# Flexible Thermoelectric Generators and 2-D Graphene pH Sensors for Wireless Sensing in Hot Spring Ecosystem

by

Ruirui Han

A Dissertation Presented in Partial Fulfillment
of the Requirements for the Degree
Doctor of Philosophy

Approved December 2017 by the
Graduate Supervisory Committee:

Hongyu Yu, Chair
Hanqing Jiang
Hongbin Yu
Edward Garnero
Mingming Li

ARIZONA STATE UNIVERSITY

May 2018

# ABSTRACT

Energy harvesting from ambient is important to configuring Wireless Sensor Networks (WSN) for environmental data collecting. In this work, highly flexible thermoelectric generators (TEGs) have been studied and fabricated to supply power to the wireless sensor notes used for data collecting in hot spring environment. The fabricated flexible TEGs can be easily deployed on the uneven surface of heated rocks at the rim of hot springs. By employing the temperature gradient between the hot rock surface and the air, these TEGs can generate power to extend the battery lifetime of the sensor notes and therefore reduce multiple batteries changes where the environment is usually harsh in hot springs. Also, they show great promise for self-powered wireless sensor notes. Traditional thermoelectric material bismuth telluride ($Bi_2Te_3$) and advanced MEMS (Microelectromechanical systems) thin film techniques were used for the fabrication. Test results show that when a flexible TEG array with an area of $3.4cm^2$ was placed on the hot plate surface of 80°C in the air under room temperature, it had an open circuit voltage output of 17.6mV and a short circuit current output of 0.53mA. The generated power was approximately $7mW/m^2$.

On the other hand, high pressure, temperatures that can reach boiling, and the pH of different hot springs ranging from <2 to >9 make hot spring ecosystem a unique environment that is difficult to study. WSN allows many scientific studies in harsh environments that are not feasible with traditional instrumentation. However, wireless pH sensing for long time in situ data collection is still challenging for two reasons. First, the existing commercial-off-the-shelf pH meters are frequent calibration dependent; second, biofouling causes significant measurement error and drift. In this work, 2-dimentional graphene pH sensors were studied and calibration free graphene pH sensor prototypes were fabricated. Test result shows the resistance of the fabricated device changes linearly with the pH values (in the range of 3-11) in the surrounding liquid environment. Field tests show graphene layer greatly prevented the microbial fouling. Therefore, graphene pH sensors are promising candidates that can be effectively used for wireless pH sensing in exploration of hot spring ecosystems.

# DEDICATION

To Qunshan – Thank you for everything.

To Aaron.

# ACKNOWLEDGMENTS

I would like to express my deepest gratitude to my advisor, Hongyu Yu, for providing the guidance on my study and research and brining me into the wonderful interdisciplinary world of engineering and science. I would also like to thank him for his endless support for me and my family throughout my years in ASU.

I would like to thank members of the research groups – Mengbing, Sally, Zuofeng, Rui, Hai, Ziyu, Jon, Bryce, Zeming, Wenwen, Xu and Teng for their friendship and help with various projects. I would like to thank students and colleagues in SESE–Shule, Hongyu, Yucong, Huawei, Guang and Yu for our good time together and their help to enhance my background in science. I would like to thank the CSSER cleanroom staff – Todd, Kevin, Scott and Carrie for their help with using the equipment and teaching the cleanroom safety and experiment experience.

I would like to thank Hanqing Jiang for supporting my research projects with his great experience in soft materials and electronics. I would like to thank Hongbin Yu for advising me with his solid knowledge in semiconductor device. I would like to thank Edward Garnero for his important input in my research with his solid scientific background and engineering projects experience. I would like to thank Mingming Li for his guidance on my research from point views of a wonderful geodynamicist.

I would like to thank my parents– for their continuous love and support throughout the years.

Most importantly, I would like to thank my wonderful husband, Qunshan. Thank you for appearing in my life and being there since then with all your love and patience.

Finally, I would like to thank my baby son, Aaron– for your arriving and getting me to know the strength of motherhood sometimes is greater than natural laws.

TABLE OF CONTENT

Page

CHAPTER

## LIST OF TABLES

# LIST OF FIGURES

Figure Page

Figure Page

Figure Page

Figure Page

Figure Page

Figure Page

# CHAPTER 1

# INTRODUCTION

## 1.1 Biogeochemical Exploration of Hot Spring Ecosystem

Hot spring ecosystem is one of the most common hydrothermal features on the Earth and many scientists have great interest in exploring this type of ecosystem. Barns et al. (1994) found that the genetic diversity in hot springs is much higher than that of almost any other environment on Earth, which is important to investigating gene transfer and comparison and genetic evolution. Based on gene studies and isotopic studies, scientists pointed out that early Earth oceans may have been significantly warmer and gradually cooling to current temperatures (Knauth & Lowe, 2003) and organisms hosting ancestral elongation genes lived in environments that progressively cooled from the Archaean to the present (Gaucher, Kratzer, & Randall, 2010). Therefore, some of the organisms found in the hot springs may be genetically similar to the first life to appear on the Earth. The hot springs are also important geochemical environments, where dynamic cooling, fluid mixing, as well as mineral dissolution and precipitation happen. Geochemical research of hot springs is important to understanding the existence of certain types of biology in these environments. The biology thrives in the hot spring by effectively utilizing the molecules and ions available in the water or sediment (Shock, Holland, Meyer-Dombard, & Amend, 2005).

In volcanically or tectonically active regions such as Yellowstone National Park, many hot springs are of high temperature (often boiling), forming the habitats for thermophile-microscopic organisms which can survive and thrive in extreme heat (Hugenholtz, Pitulle, Hershberger, & Pace, 1998). These microorganisms are grouped together and appear as masses of colors in Yellowstone’s hot springs, as shown in Figure 1.1.Some of these microorganisms are quite similar to the first life forms which are capable of photosynthesis(Konhauser, Jones, Reysenbach, & Renaut, 2003). Therefore, many scientists study these microbial communities and the geochemical processes in hot spring ecosystems, which is important to the exploration of life origin. These researches include geochemistry, biochemistry and geobiology as shown in Figure 1.2. For these researches, measurement is required, including measurement of pH, temperature, pressure, conductivity, dissolved oxygen. For all these measurements, highly specialized sensors and sensing system is essential.

Figure 1.1 Hot Spring in Yellowstone National Park, US

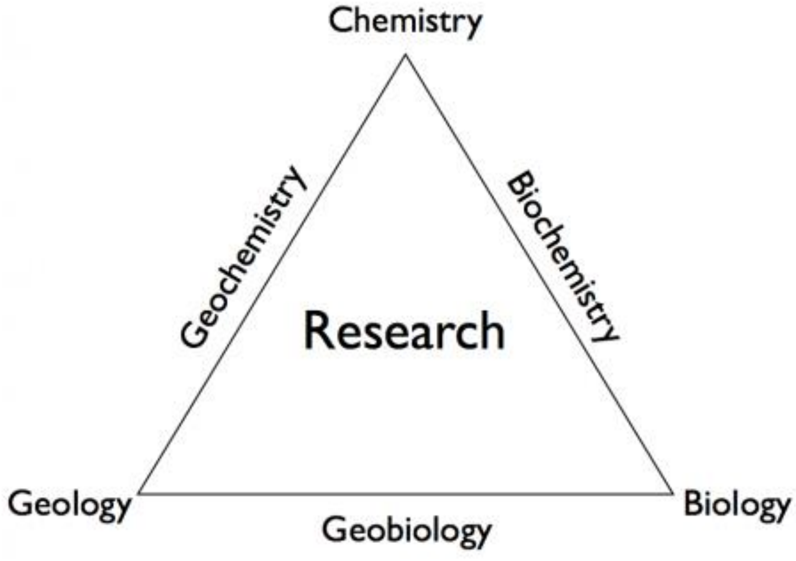

Figure 1.2 Researches in Hot Spring Ecosystems

I did some temperature measurements in the hot spring systems in Yellowstone National Park in the year of 2013. Figure 1.3 shows a stream located in the Norris area of the park. It has two outflow channels with different colors. The temperature sensor array was immersed in the yellow side of the stream for the temperature measurement as shown in Figure 1.3. There are 15 temperature sensors in total for the array, from Sensor 1 to Sensor 15. The measurement results of every other sensor (Sensor1, Sensor3, Sensor5…to Sensor15) for 10s with a step of 0.5s were plotted in Figure 1.4, which shows that the temperature of the yellow outflow is around 63°C. Figure 1.5 shows the measurement for the green outflow, where the temperature is around 45°C based on the measurement results plotted in Figure 1.6. Figure 1.7 shows the measurement across the two channels of both yellow outflow and green outflow. The measurement results of the 15 sensors for 8s with a step of 1s were plotted in Figure 1.8, which shows that the temperature goes from 40s in the green area to 60s in the yellow area. These temperature measurements confirm the scientific hypothesis that temperature plays a key role in supporting the habitation for different microbial communities in the system, some of which have the ability of photosynthesis while others don't and therefore they appear in different colors.

Figure 1.3 Stream Located in the Norris Area of Yellowstone National Park. Temperature Measurement in the Yellow Outflow Channel

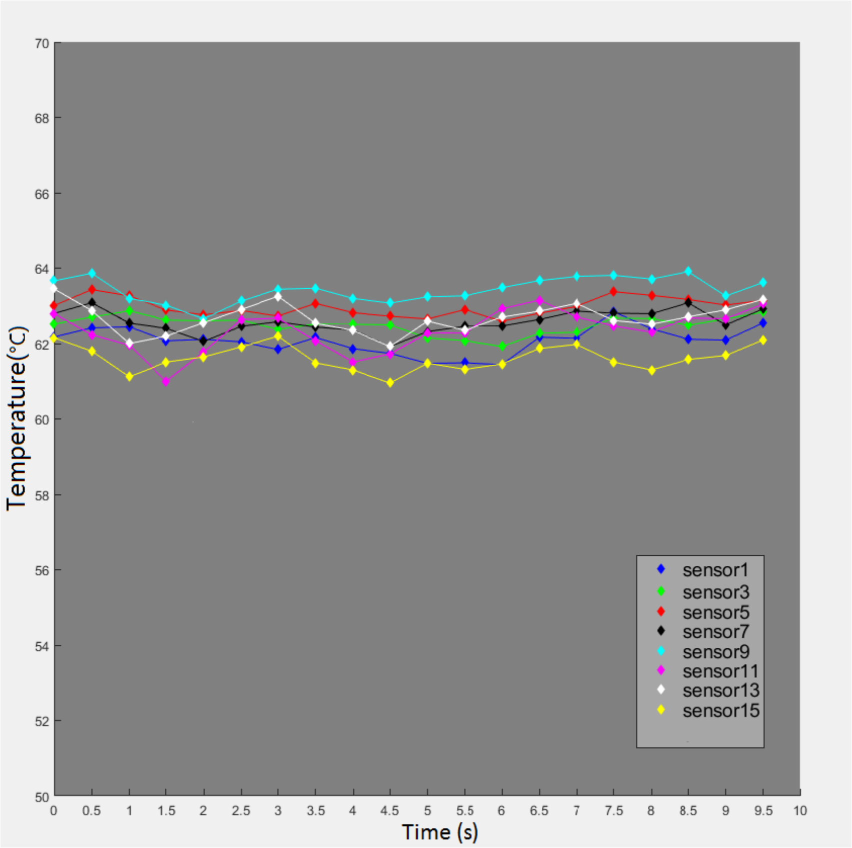

Figure 1.4 Temperature Measurement Results for the Yellow Outflow Channel

Figure 1.5 Temperature Measurement in the Green Outflow Channel

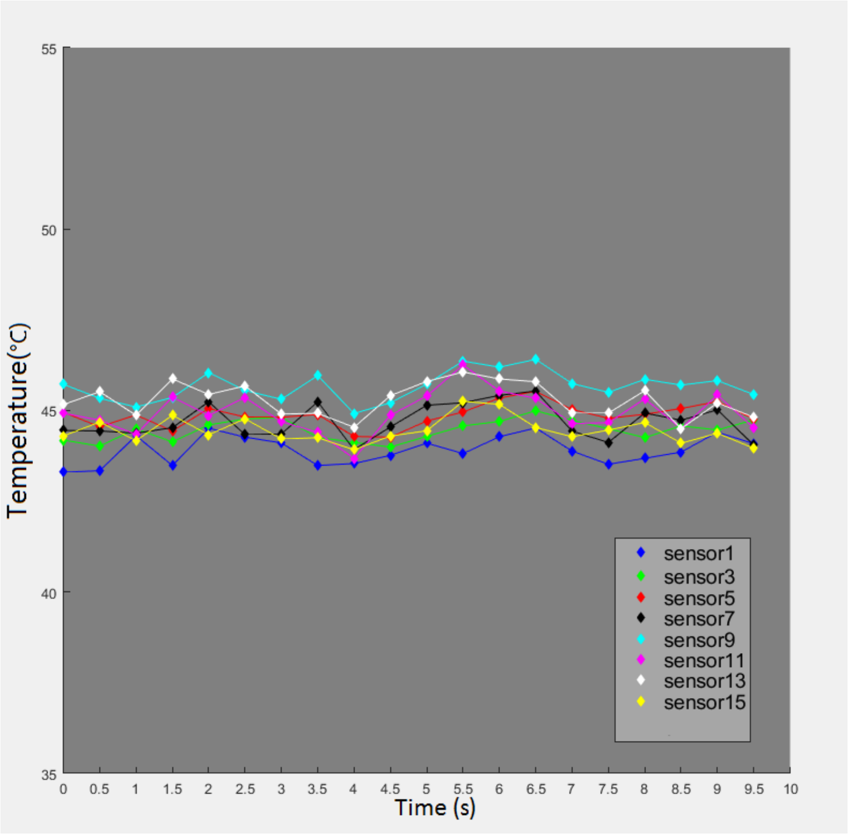

Figure 1.6 Temperature Measurement Results for the Green Outflow Channel

Figure 1.7 Temperature Measurement across the Yellow Outflow Channel and the Green Outflow Channel

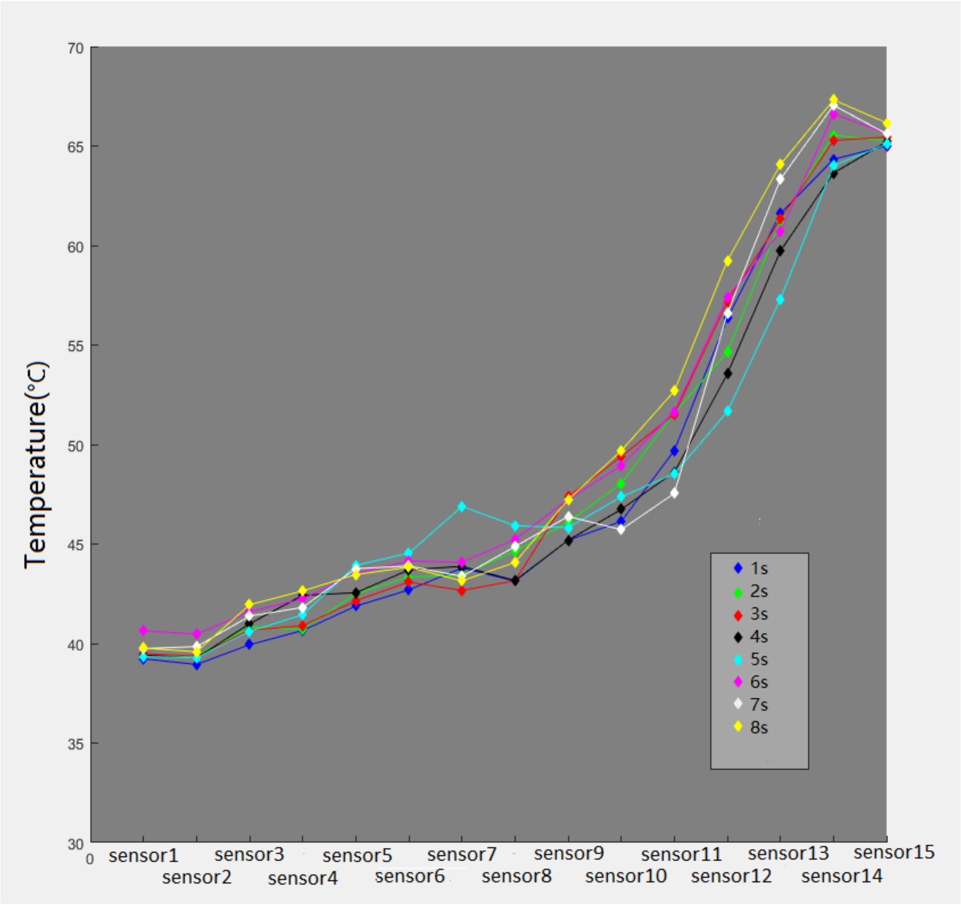

Figure 1.8 Temperature Measurement Results across the Green Outflow Channel and the Yellow Outflow Channel

## 1.2 Challenges of Wireless Sensing in Hot Spring Ecosystem

Figure 1.9 shows another example of field measurement for research on biogeochemical exploration in hot spring ecosystem(Cox, Shock, & Havig, 2011). The result gives the pH and temperature condition for photosynthesis possibly existed in hot spring ecosystem. pH probe was used for the measurement in the field for large number of points across the hot spring stream as shown in the figure, which cost lots of time and human energy(months of field work). Therefore, for scientific research in the field, data recording at large scale and with high resolution, real time data recording and data recording for long time are usually required. However, traditional sensing instrumentation with long wires connected to data processing unit and battery system as I used (Figure 1.10) for temperature measurement in Yellowstone hot springs is not efficiency. The solution to this problem is Wireless Sensor Networks (WSN).

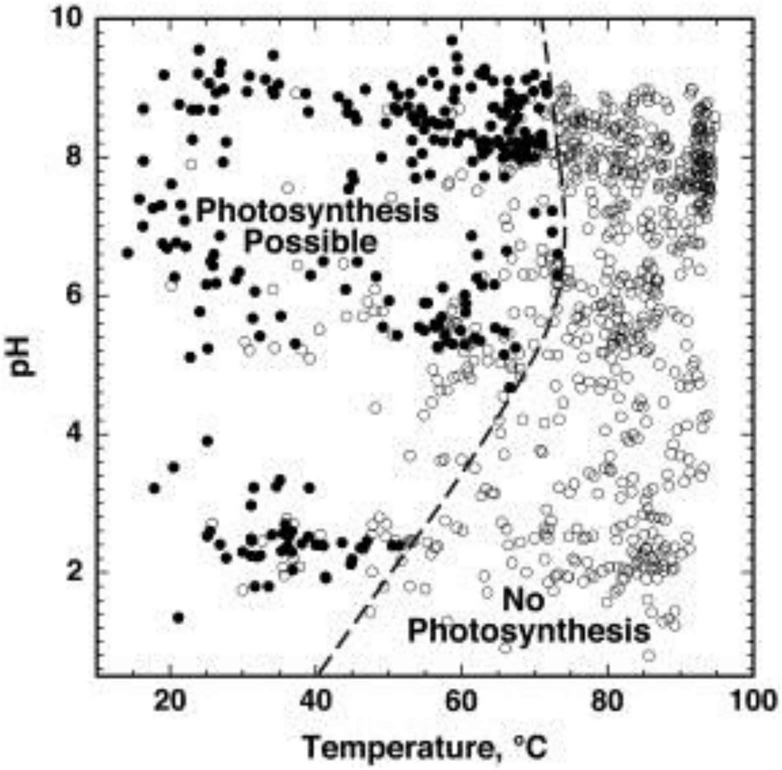

Figure 1.9 pH and Temperature Condition for Photosynthesis Possible Existing in Hot Spring Ecosystem (Cox et al., 2011)

Figure 1.10 Temperature Measurement in Hot Spring Using Sensor Array with Traditional Wire Connection

Figure 1.11 shows the diagram for one sensor note of the WSN. The sensor is used to collect data in the environment and with the control of the micro controller, the signal is sent out by the wireless RF transmitters through an antenna. Battery is used to supply power for the whole system.

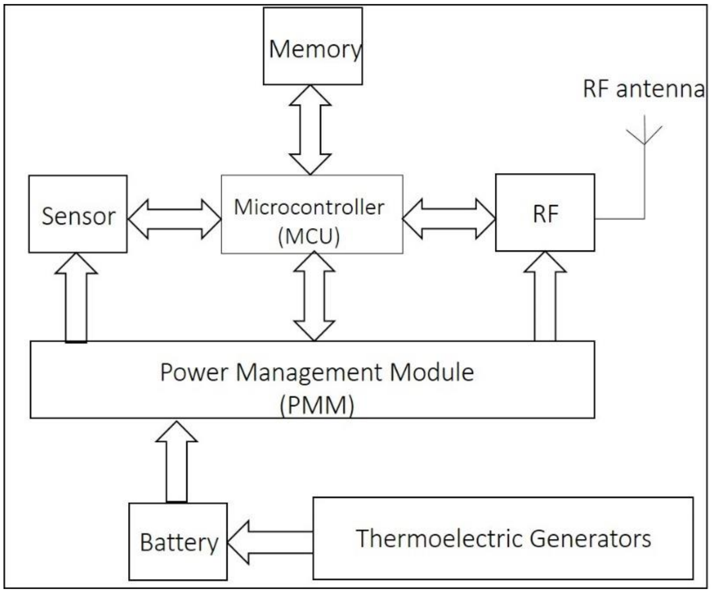

Figure 1.11 A Sensor Note of WSN

Researches have been greatly benefited from data collection using WSN in recent years(Werner-Allen et al., 2006), where long time in situ data recording at large scale and with high resolution is required. However, the battery lifetime of the sensor notes is usually short and researchers have to change the batteries repeatedly in these harsh hot spring environments. One solution to this problem is extending the battery lifetime with energy harvested from ambient by thermoelectric generator which is included in schematic diagram shown in Figure 1.11. Thermoelectric generators (TEGs) are solid-state devices that can convert heat into electricity when temperature difference exists. They are small, simple and inexpensive and they can be easily designed to operate with small heat sources and small temperature gradient (Snyder, 2008). The heated rocks at the rim of the hot springs can be the energy source for thermoelectric power generation. However, the rock surfaces are usually of arbitrary shapes and not flat so that the traditional rigid TEGs cannot be well applied for effective energy harvesting.

Therefore, in this work, highly flexible TEGs that can be easily deployed on the uneven surface of the heated rocks were fabricated to supply power for the wireless sensing note in hot spring environment and therefore reduce multiple batteries changes where the environment is usually harsh in hot springs. Also, they show great promise for self-powered wireless sensor notes. Finite element analysis (FEA) of heat transfer has been conducted to simulate temperature distribution across the thermoelectric material of the device. Traditional thermoelectric material bismuth telluride ($Bi_2Te_3$) and advanced MEMS (Microelectromechanical systems) thin film techniques were used for the fabrication to achieve the high thermoelectric efficiency and enable the high flexibility of the device.

On the other hand, measurements of the chemical and physical properties of the hot spring are critical for understanding the biogeochemical environment and the origin of life. Hot spring ecosystem is an important type of harsh environments. High pressure, temperatures that can reach boiling, and the pH of different hot springs ranging from <2 to >9 make hot spring ecosystem a unique environment that is difficult to study. Thanks to the development of WSN, which allows many scientific studies that aren’t feasible with traditional instrumentation. However, wireless pH sensing for long time in-situ data collection is still challenging for two reasons. First, the existing commercial-off-the-shelf pH meters are frequent calibration dependent; second, biofouling causes significant measurement error and drift.

This work gives the study results on 2-D graphene pH sensors, and graphene pH sensor prototypes were fabricated. Compared to traditional pH probes, reference electrode (Ag/AgCl electrode) is no longer necessary as a part of sensing unit for graphene pH sensor. Therefore, graphene pH sensors shows great promise for calibration free sensors. Graphene layer can successfully prevent the microbial fouling, which is very critical to wireless sensing in exploration of hot spring ecosystems.

Also, graphene pH sensors are of 2-D structure and have great potential in ultra mini size sensors. Therefore, many small sensing elements can form into sensing arrays, which allows graphene pH sensors to provide measurement of pH values at extremely high spatial resolution. Graphene has very stable chemical and thermal properties and will be both chemically and thermally-tolerant to the conditions present in the hot springs. Also, graphene sensors can be easily integrated with other types of MEMS sensors. Once these sensors are successfully fabricated and deployed in Wireless Sensor Networks, they will provide data that reveal for the first time the true extent of the spatial and temporal variability in these systems that can be used to test hypotheses about the relationships between geophysical, geochemical and biological systems(Oiler, 2013).

### 1.3 MEMS Fabrication Technology for Sensors and Generators

MEMS, microelectromechanical systems, are systems that consist of small scale electrical and mechanical components for specific purposes(K. B. Lee, 2011). The mechanical components include levers, springs, deformable membranes, vibrating structures etc. and electrical components include resistors, capacitors, inductors, etc. It can also include optical, radio - frequency, and nano devices. A typical dimension of a MEMS component varies from 1 μ m to a few hundred micrometers, and the overall size is approximately less than 1 mm. The first MEMS device was conceived in 1965 and it served as a tuner for microelectronic radios(Nathanson & Wickstrom, 1965). Examples of some well-known MEMS device include pressure sensors, accelerometers (inertial sensors), micromirrors, gear train, miniature robots, fluid pumps, microdroplet, generators, optical scanners, probes ,analyzers and imagers(Asada, Jiang, & Gibbs, 2004; Birch et al., 2001; Frosio, Pedersini, & Borghese, 2009; Han, Zhang, Ren, & Lin, 2011; Han, Zhang, Ren, Lin, & Liu, 2012; Han, Zhang, Ren, Lin, & Pang, 2011; Hanein, BÎhringer, Wyeth, & Willows, 2002; Huang & Chuan, 2002, p.; Jones et al., 2009; Leonov, Fiorini, Sedky, Torfs, & Van Hoof, 2005; Luczak, Oleksiuk, & Bodnicki, 2006; Martel et al., 2001; Miyajima, Murakami, & Katashiro, 2004; Otto et al., 2009; Rone & Ben-Tzvi, 2011; Singh-Gasson et al., 1999; Suntharalingam et al., 2005; Wu, Fedder, & Carley, 2002; Yang & Liao, 2007; Z. Zhang, Ren, Han, Yuan, & Pang, 2013; Z.-H. Zhang, Ren, Zhang, Han, & Liu, 2012). They can be developed where miniaturization is beneficial, such as consumer products, aerospace, automotive, biomedical, chemical, optical displays, fluidics and wireless and optical communications. Common materials for MEMS fabrication are silicon (semiconductor materials), polymers, metals, ceramics and basic MEMS processes are lithography, layer deposition and layer etching, which will be discussed in the following parts of this chapter. In the era of “more than Moore” (MtM) (“There’s more to come from Moore,” 2015), all these fabrication processes are indispensable in fabrication of semiconductor devices that play important roles in the areas of automotive electronics, remote sensing, urban planning, medical care and earth and space exploration (Dargaville et al., 2013; Kuai & Zhao, 2017; Liang et al., 2016; Wentz & Zhao, 2015; Werner-Allen et al., 2006; Yabiku, Glick, Wentz, Ghimire, & Zhao, 2017; J. Zhang et al., 2011; Q. Zhao et al., 2016; Q. Zhao, 2017; Q. Zhao, Myint, Wentz, & Fan, 2015; Q. Zhao & Wentz, 2016; Q. Zhao, Wentz, & Murray, 2014, 2017; Q. Zhao, Yang, Wang, & Wentz, 2018).

### 1.3.1 Photolithography

Photolithography, is based on photography using photoresist, a light sensitive material. Parts of layers on the substrate must remain and parts of that are not used should be removed in order to get the patterns to fabricate MEMS and microelectronic devices. Based on the design, a mask with patterns that are transparent or opaque to light is constructed, and then with photography technology, the patterns are transferred to the structural or sacrificial layers on the substrate. Figure 1.12 can be used to understand the process of photolithography. The purpose of the process shown in Figure 1.12 is to form a window on a layer using photolithography, which is an essential process to generate most MEMS device. As shown in the figure, the process start with a substrate that has a silicon dioxide ($SiO_2$) layer on the top surface. The glass mask is with an opaque metal block on transparent glass. A positive photoresist is used to coat on the $SiO_2$ layer to generate the pattern. A positive resist is a type of photoresist in which the portion of the photoresist that is exposed to light becomes soluble to the photoresist developer. The portion of the photoresist that is unexposed remains insoluble to the photoresist developer. A negative resist is a type of photoresist in which the portion of the photoresist that is exposed to light becomes insoluble to the photoresist developer. The unexposed portion of the photoresist is dissolved by the photoresist developer. Afterward the masks are placed above the substrates and exposed to UV light. The light passes the transparent parts of the mask and react with the photoresist. The exposed photoresist can dissolve in the developer and in this way the photoresist patterns are successfully transferred from the masks. Using photoresist as masks, the $SiO_2$ layer is etched to form $SiO_2$ patterns, and the remaining photoresist is removed to obtain the structure of $SiO_2$. As shown in Figure 1.12, the photolithography process with positive photoresist is used for pattern transfer from a mask to a desired material. Also, photolithographic process with a negative photoresist to form the same structure of $SiO_2$ is shown in Figure 1.13.

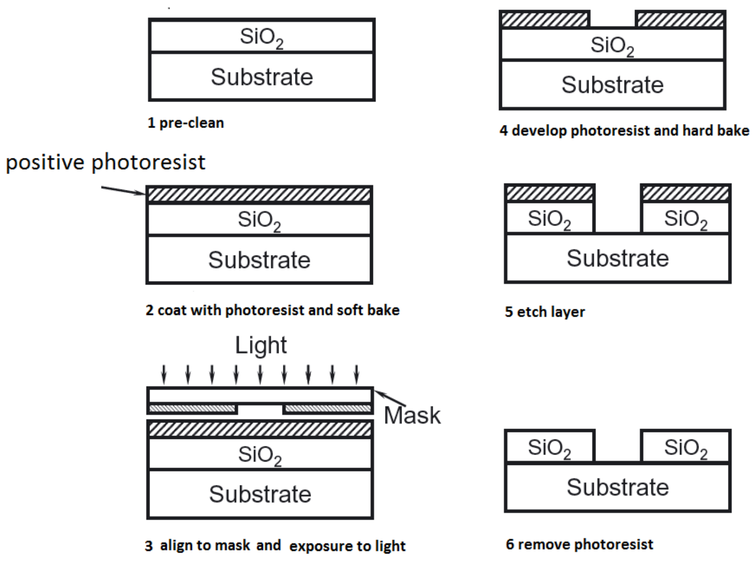

Figure 1.12 Photolithography (Positive Photoresist) and Etching Process

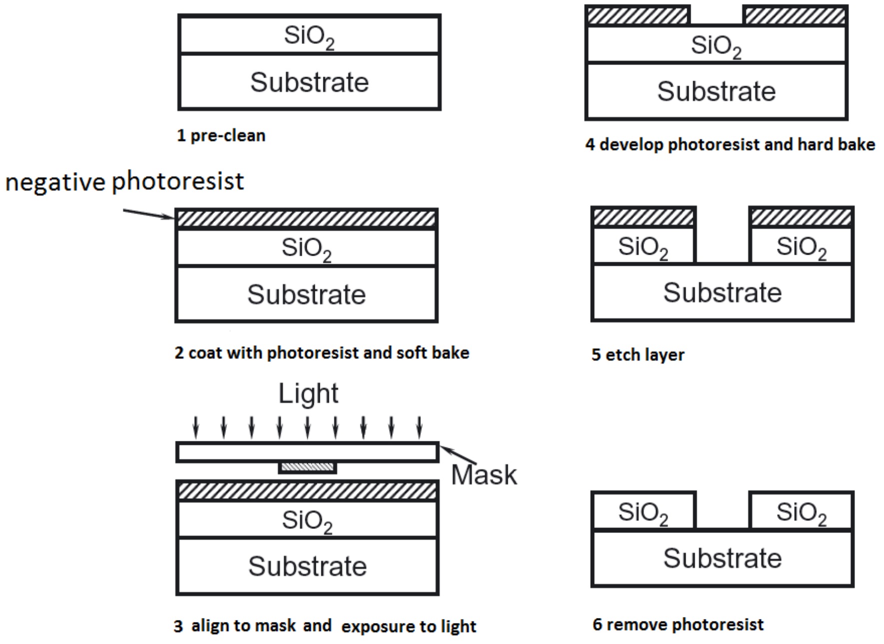

Figure 1.13 Photolithography (Negative Photoresist) and Etching Process

Detailed process of photolithography includes wafer cleaning, photoresist coating, soft baking, mask alignment and exposure, development and hard-baking. Sometimes post exposure baking is required, depending on the types of photoresist and process. Mask alignment is one of the most important steps in the photolithography process is. The mask is aligned with the wafer and the pattern can be transferred onto the wafer surface. Each mask after the first one must be aligned to the previous pattern. Once the mask has been accurately aligned with the pattern on the wafer's surface, the photoresist is exposed through the pattern on the mask with a high intensity ultraviolet light. There are three primary exposure methods: contact, proximity, and projection. They are shown in Figure 1.14. In contact printing, the photoresist-coated silicon wafer is physically brought into contact with the glass photomask. The wafer is held on a vacuum chuck, which rises until the wafer and mask contact each other. The photoresist is exposed under UV light when the wafer is in contact with the mask. Because the resist and mask are in close contact, very high resolution can be obtained in contact printing, e.g. in 0.5 microns of positive resist 1micron features is possible. The problem with contact printing is that debris can be trapped between the resist and the mask, which can damage the mask and cause defects in the pattern. The proximity exposure method is similar to contact printing except that between the wafer and the mask during exposure, a small gap, 10 to 25 microns wide, is maintained. This gap minimizes (but may not eliminate) mask damage. With proximity printing, approximately 2to 4 microns resolution is possible. In projection printing, mask damage can be entirely avoided. The mask and the resist-coated wafer are many centimeters away and the image of the patterns on the mask is projected onto the wafer. In order to achieve high resolution, only a small portion of the mask is imaged and is scanned or stepped over the surface of the wafer. The resolution is approximately 1-micron.

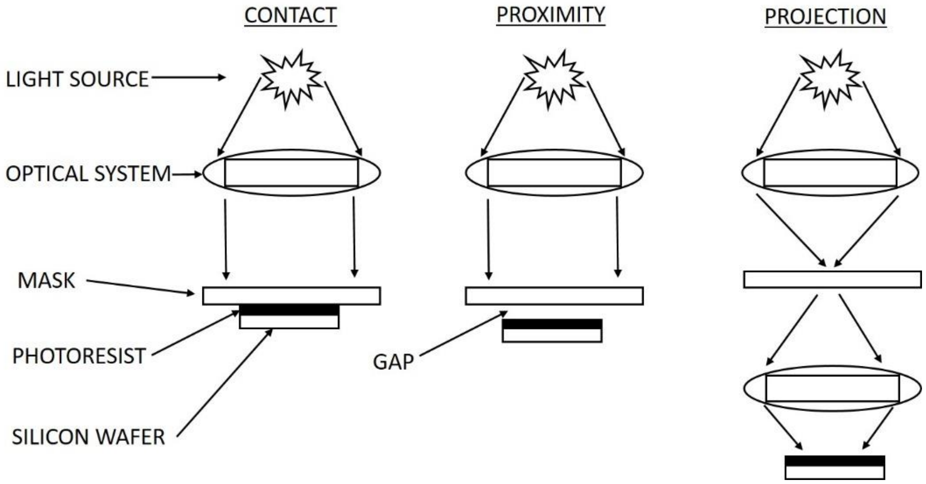

Figure 1.14 Three Primary Exposure Methods: Contact, Proximity, and Projection

Besides traditional UV light exposure, there are other types of lithography, for example, electron beam lithography, Ion beam lithography, X-ray lithography. A successful photolithography process is related to good 1) pre-cleaning, 2) photoresist choice, 3) developer choice, 4) adhesion promoter choice: HMDS, 5) temperature control, 6) descum (post-cleaning),7) alignment.

### 1.3.2 Layer Deposition

There two types of MEMS deposition process, physical deposition and chemical deposition. Physical vapor deposition (PVD) involves a process in which a material is removed from a target and deposited on a surface. Two common Physical vapor deposition used are sputtering and evaporation (thermal evaporation and electron beam evaporation). Figure 1.15 shows a schematic of DC sputtering in which an upper metal target serves as a cathode to generate metal particles and the substrate (wafer) serves as an anode (which can accept electrons). A DC voltage is applied across the target and substrate and the incoming sputtering gas are usually Ar,Kr and Xe. The cathode voltage is from -500 to -5000V and current density is from 0.1 to 2.0MA/cm2.The pressure of the chamber is low, ranging from 0.1 to 10 torr. Electrons from the target (cathode) flow toward the substrate (anode) and hit argon atoms, so that the argon is ionized and accelerated into the target and collides with the target, so that the kinetic energy of the ionized argon is transferred to the target. Bombardment of the ionized argon results in scattering of the target metal, and the scattered metal atoms then move into the substrate and are deposited on the substrate. Sputtering has good step coverage while the metal evaporation does not. Since metal can act as a conductor and can transfer electrons to the ionized argon, DC sputtering is used for a metal target. If an insulation layer deposition is required, we can use RF (radio frequency) sputtering, where AC voltage with DC bias voltage is applied across the target and substrate. The frequency of the RF is 13.56MHz or 100KHz.The insulation target acts as a capacitor and the electrons can be transferred to the ionized argon.

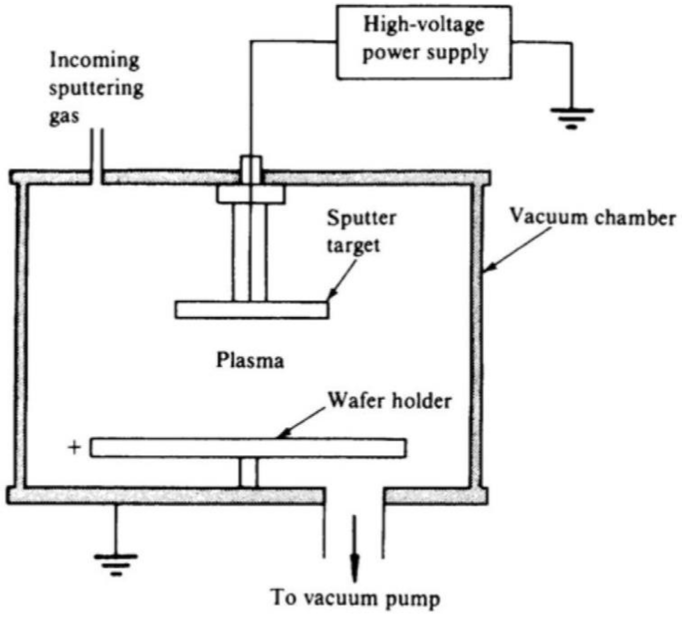

Figure 1.15 Schematic of Sputtering (Runyan & Bean, 1990)

Thermal evaporation is one of the simplest methods of depositing a metal. The metal is heated by Joule heating using a current and evaporates into vacuum (low pressure) and is directed toward the wafer and deposited on the wafer as shown in Figure 1.16 (a). Thermal evaporation is generally used to deposit metals with a low temperature of evaporation (e.g., aluminum, copper, and gold). For electron beam evaporation, an electron beam of high velocity is generated by an electron beam source and directed to the metal in a crucible as shown in Figure 1.16 (b). When the electrons hit the metal, kinetic energy due to the electron velocity is converted into heat energy, which increases the temperature of the metal to evaporate and deposit onto the wafer.

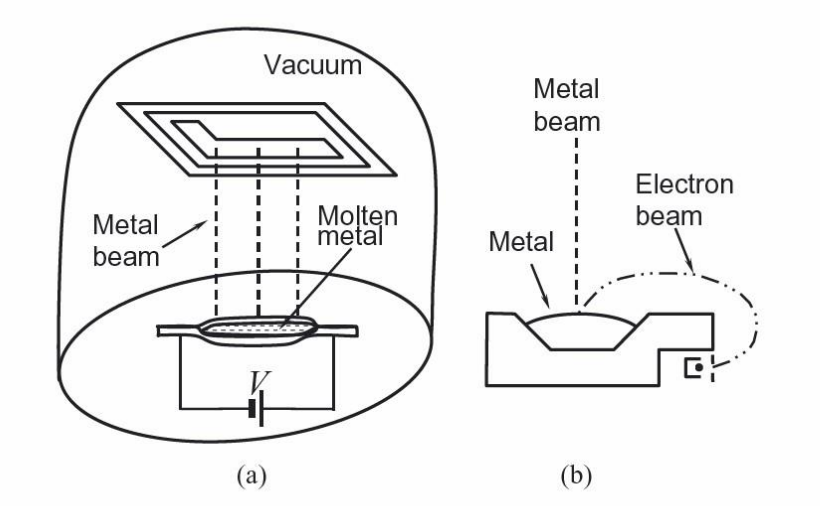

Figure 1.16 (a) Thermal Evaporation and (b) Electron Beam Evaporation (K. B. Lee, 2011)

Chemical vapor deposition (CVD), uses thermal decomposition and/or reaction of chemicals to deposit a layer on a substrate. Figure 1.17 shows a schematic of LPCVD (low pressure CVD) which is used widely for deposition of polycrystalline silicon dioxide, and silicon nitride. In Figure 1.17, reactant gases are introduced from the gas inlet, flow over wafers, and are pumped out at the right side. While the gases flow over the wafers at a temperature of 300°C to 1150°C, the gases introduced are decomposed into a desired material that is deposited on the wafers. With LPCVD, uniform layers can be obtained and several hundred wafers can be processed in a single run.

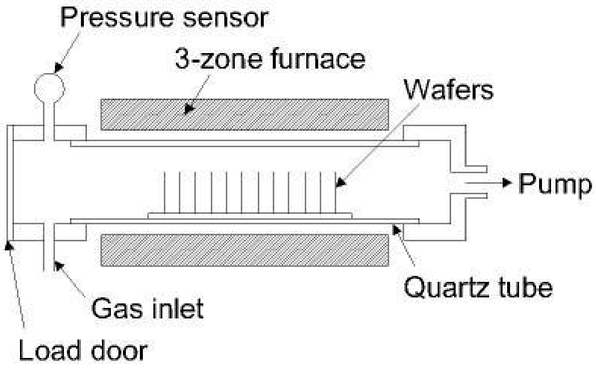

Figure 1.17 Schematic of LPCVD ("Deposition Processes," n.d.)

Parylene is also deposited through CVD process. There are mainly three steps for the deposition as shown in Figure 1.18. In first step the vaporizer is heated to around 150°C and the dimer starts to turn to gas from solid. In Step2 the dimer gas enter the pyrolosis furnace where the temperature is around 690°C and the gas starts to transform into single monomer vapor. In Step 3, the monomer vapor enters room-temperature chamber and bond to other monomers forming long molecular chains to grow the polymer layer on the target surface.

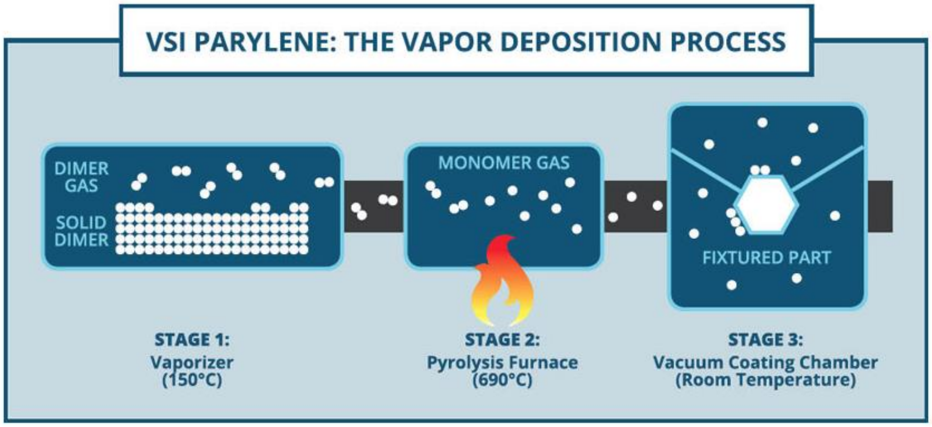

Figure 1.18 Parylene Deposition Process("Parylene Coating & Vapor Deposition Process | VSI Parylene," n.d.)

### 1.3.3 Layer Etching

There are two groups of etching: wet etching and dry etching. For wet etching, a wet etchant is used to remove the undesired portions of a layer and form the structure on the substrate. Depending on the etchant and layers to be etched, wet etching is divided into isotropic and anisotropic wet etching. For isotropic wet etching the etching rate is almost the same in all direction. Figure 1.19 shows the Isotropic etching of bulk silicon, which undercut is formed under the masking layer. Anisotropic etchants etch materials much faster in one direction than in others. Figure 1.20 illustrates how anisotropic etchants etch (100) bulk silicon.

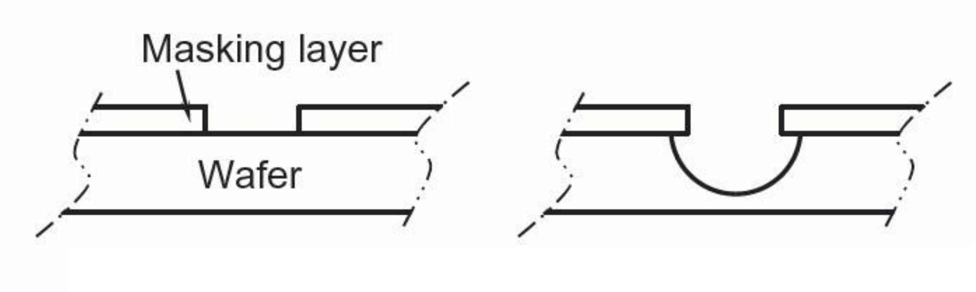

Figure 1.19 Isotropic Etching of Bulk Silicon (K. B. Lee, 2011)

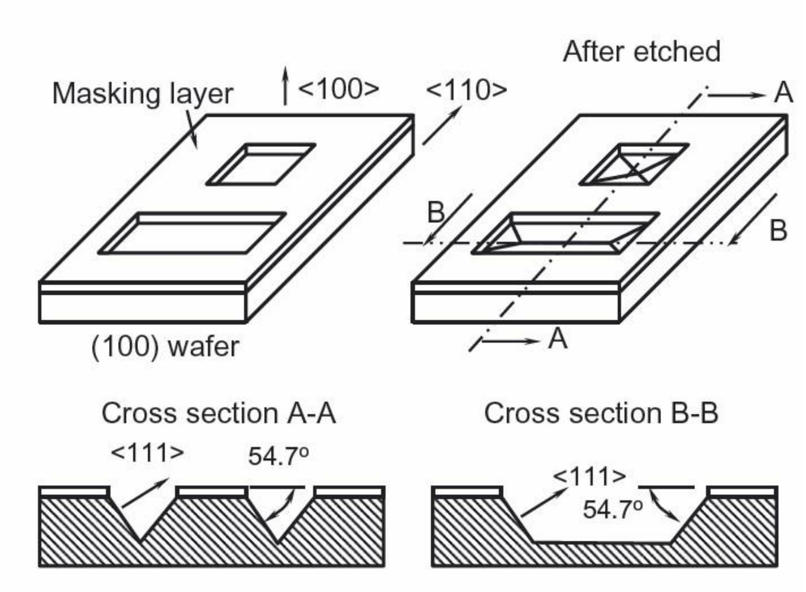

Figure 1.20 Anisotropic Etchants Etch (100) Bulk Silicon (K. B. Lee, 2011)

Dry etching uses gas vapor or plasma to etch layers or structures. RIE (Reactive Ion Etching) and PE (Plasma Etching) are the most two common dry etching methods. RIE involves physical and chemical etching mechanism. It is directional etching. PE only involves chemical etching and thus the etching rate is faster than RIE. It is isotropic etching and it is more selective and less prone to radiation damage.

Other MEMS fabrication process includes thermal oxidation, ion implantation, diffusion, electroplating, lift off and so on. The process of lift - off, uses the poor coverage of the metal evaporation in vacuum to form a metal pattern on a layer. In the lift-off process shown in Figure 1.21, a sacrificial pattern (e.g., photoresist) is formed on the layer, and a metal layer is then deposited by thermal evaporation or electron beam evaporation. Upon removing the sacrificial layer, the upper metal on the sacrificial pattern is lifted off and only the lower metal pattern remains. With this method, etching can be avoided to pattern the metal. Some types of metals are pretty difficult to etch. For lift-off processes, negative resists are generally the best choice: On the one hand, negative resists designed for lift-off attain a reproducible undercut. Such an undercut helps to prevent the resist sidewalls from being coated, which makes the subsequent lift-off easier. On the other hand, the crosslinking of the resin of common negative resists maintains the undercut even at very high coating temperatures, which helps to maintain the undercut during coating.

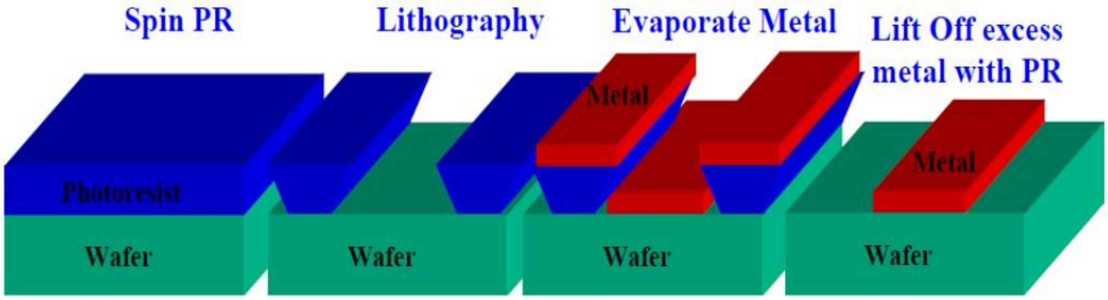

Figure 1.21 Lift-off Process

# CHAPTER 2

# HEAT TRANSFER MODELING FOR FLEXIBLE THERMOELECTRIC GENERATORS

## 2.1 Traditional Rigid Thermoelectric Generators

There are two categories of natural energy, renewable resources and non-renewable resources. Renewable energy resources can be renewed or replaced along with their exploitation and are always available for use, such as solar energy, hydropower, etc. Non-renewable energy resources, if used in unlimited way, will be exhausted forever. Unfortunately, humans are greatly relying on the non-renewable energy and they are running out. With some forecasts that the Earth will run out of coal and other non-renewable resource in about 200 years. Another urgent problem is the greenhouse effect, the main reason for which is the massive exhaust of CO2 (Fahrner & Schwertheim, 2009)Therefore, researchers are exploring more applications of renewable energy resources and increasing the energy harvesting efficiency. One success is the invention and popularization of solar cells. Another important type of renewable energy resource which can offer huge potential of energy is thermoelectricity and it has greatly attracted researchers' interest over the past decade. Thermoelectric generators are solid-state devices that can convert heat into electricity when temperature difference exists. Compared to the large, traditional heat engines, thermoelectric generators are small, simple and inexpensive and they can be used to harvest energy whenever unused heat appears. Each year, nearly 60% of the energy produced in US have never been utilized (Kaiper, 2004). Figure 2.1 shows the U.S. energy flow trends in 2002. Therefore, thermoelectric generators are widely used in automotive waste heat recovery and home co-generation of heat and electricity. This type of generators has also been used reliably in deep space probes for over 30 years such as the Voyager missions of NASA.

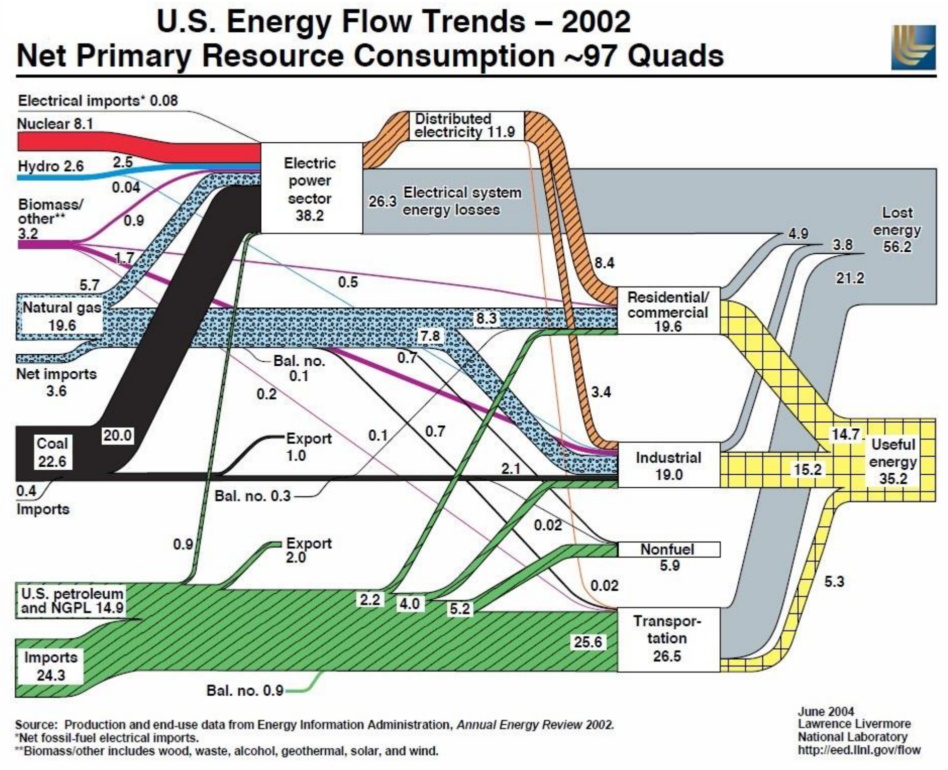
U.S. Energy Flow Trends – 2002
Net Primary Resource Consumption ~97 Quads

Source: Production and end-use data from Energy Information Administration, *Annual Energy Review 2002.*
*Net fossil-fuel electrical imports.
**Biomass/other includes wood, waste, alcohol, geothermal, solar, and wind.

June 2004
Lawrence Livermore
National Laboratory
http://eed.llnl.gov/flow

Figure 2.1 U.S. Energy Flow Trends in 2002(Kaiper, 2004)

However, these thermoelectric generators are usually rigid and cannot be well applied when the heat source surface is not flat, such as in the cases of automobile and spacecraft components and robot joints. Figure 2.2 shows a rigid thermoelectric generator sold by Customer Thermoelectric. Figure 2.3 shows the heat waste in engine exhaust. Figure 2.4 and Figure 2.5 show the surface of the car exhaust manifold and catalytic converter, which are very good heat source surface with the temperature of many hundred degrees. But the complexity of these heat surfaces limit the use of the rigid conventional thermoelectric generators. Also, the large area of rigid thermoelectric generator arrays takes considerable space for storage and transportation. Therefore, highly flexible thermoelectric generators demonstrated in Figure 2.6 can be well applied in all kinds of areas.

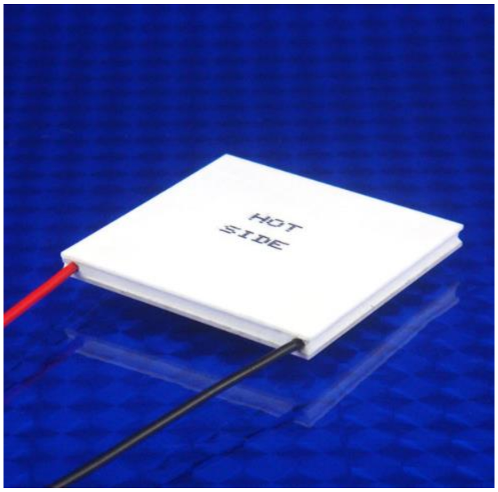

Figure 2.2 Rigid Thermoelectric Generator

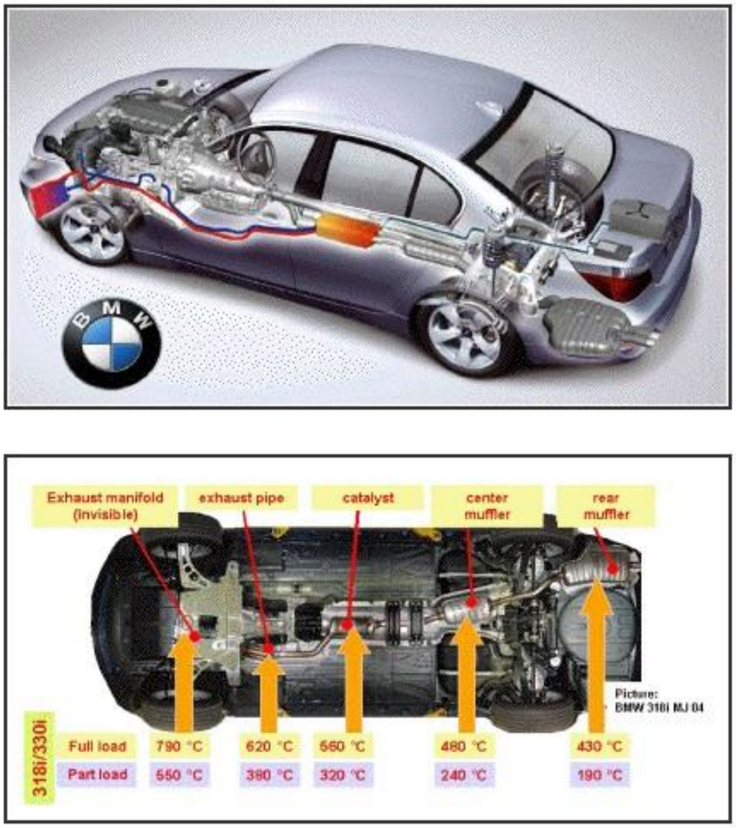

Figure 2.3 Heat Waste in Engine Exhaust (Snyder, 2008)

Figure 2.4 Car Exhaust Manifold

Figure 2.5 Catalytic Converter

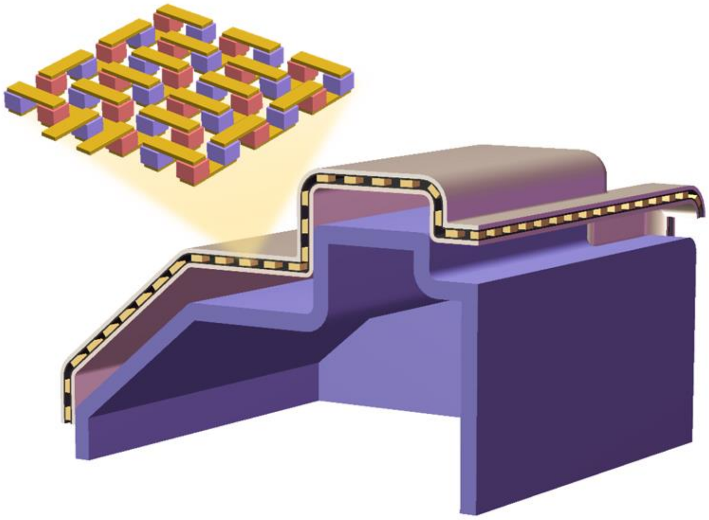

Figure 2.6 Demonstration of Flexible Thermoelectric Generator

## 2.2 State-of-Art Flexible Thermoelectric Generator

Many researchers have reported the fabrication of flexible thermoelectric generator with elastic polymers including polypyrrole (Eftekhari, Kazemzad, & Keyanpour-Rad, 2006; Kemp et al., 1999), polyaniline(Jun, Lian-meng, Li, & Xin-feng, 2003; K. Lee et al., 2006),and poly(3,4-ethylenedioxythiophene):poly(styrenesulfonate)(S. J. Kim, We, & Cho, 2014) as thermoelectric materials. These polymers exhibited flexibility but showed very low output power density due to the low power factor of polymers.

Sun Jin Kim’s group reported a glass fabric based flexible TEG that achieved a very large output power density(S. J. Kim et al., 2014) as shown in Figure 2.7. PDMS was used as the flexible package for the device. However, the PDMS layer is very thick (about 500μm), which gives low flexibility of the TEG (bending radius>20mm). Kouji Suemori’s group reported a highly flexible TEG (bending radius >5mm) fabricated on a thin polyethylene naphthalate film substrate(20um) with a composite material of carbon nanotubes (CNTs) and polystyrene as the thermoelectric material as shown in Figure 2.8(Suemori, Hoshino, & Kamata, 2013). However, the output power is not high, especially when the temperature difference is low as shown in Figure 2.9. Rhombuses indicate test results of the fabricated device. Circles are calculated results by assuming a packing density of 0.94. Packing density is the ratio of the area with CNT-polystyrene composites to the entire area of the TEG. Figure 2.9 shows when the temperature difference is smaller than 10°C, there is hardly output power.

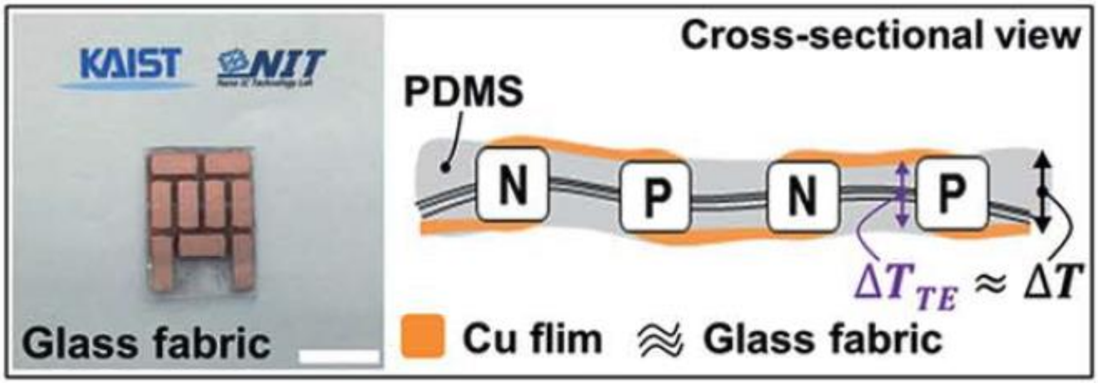

Figure 2.7 Actual Photos and Schematic Illustrations of the Glass Fabric-based Flexible TEG(S. J. Kim et al., 2014)

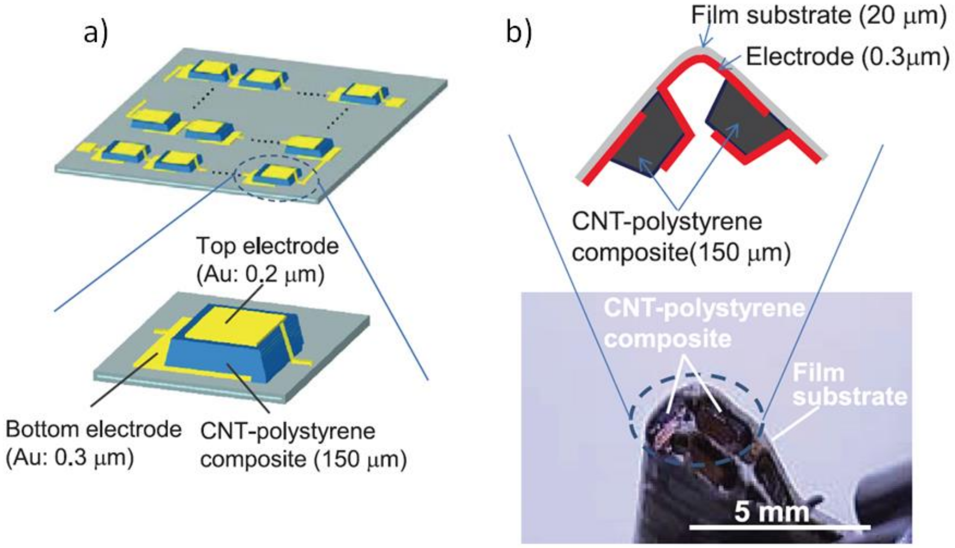

Figure 2.8 Structure of Carbon Nanotubes (CNTs) and Polystyrene TEG a) Schematic Illustrations of the TEG b) Illustration and Close-up Photograph of Bent TEG(Suemori et al., 2013)

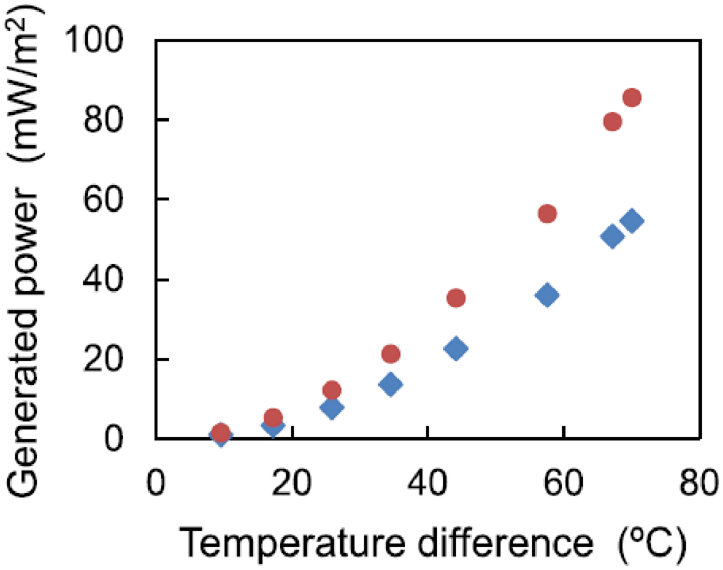

Figure 2.9 Generated Electric Power of Carbon Nanotubes (CNTs) and Polystyrene TEG as a Function of Temperature Difference ( Rhombuses Indicate Test Results of the

Device, Circles are Calculated Results by Assuming a Packing Density of 0.94) (Suemori et al., 2013)

In this work, traditional rigid thermoelectric material bismuth telluride ($Bi_2Te_3$) combined with thin film material parylene C (tens of micron thick) were used to fabricate the thermoelectric generators that will have both high thermoelectric efficiency and high flexibility.

These flexible thermoelectric generators can be easily deployed on the uneven surface of heated rocks at the rim of hot springs as shown in Figure 2.10. By employing the temperature gradient between the hot rock surface and the air, these TEGs can generate power to extend the battery lifetime of the sensor notes and therefore reduce multiple batteries changes where the environment is usually harsh in hot springs. Also, they show great promise for self-powered wireless sensor notes.

Figure 2.10 Heated Rock Surface at the Rim of Hot Springs in Yellowstone National Park

## 2.3 Working Principles of Thermoelectric Generators

The basic working principles of this device is the Seebeck effect. It is named after its discoverer, Thomas Seebeck (Figure 2.11). In his experiment (shown in Figure 2.12), he connected two different metal stripes at their ends and placed the compass needle in the center. When one junction was heated, there was a deflection of the needle, which means current was generated.

Figure 2.11 Thomas Johann Seebeck

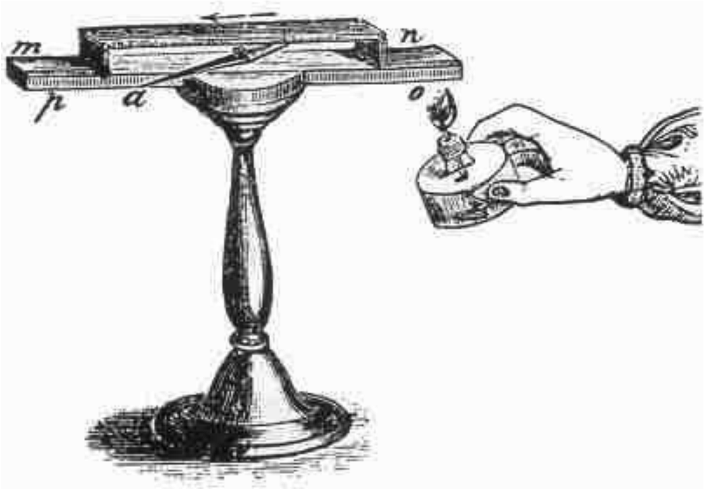

Figure 2.12 Seebeck’s Experimental Setup

When semiconductor is used as an example, its working mechanism is similar to metal. Figure 2.13 shows a n type semiconductor with two ends $X_1$ and $X_2$. $X_2$ is heated. The temperature gradient from the cold end to the hot end is assumed to be liner which is shown in Figure 2.13 (b). This temperature gradient causes a change of the Fermi energy $E_F$ (imagine, at supper high temperature, fermi energy of both p type and n type is close to intrinsic fermi energy) and thus a potential difference. It is called Seeback voltage. It is proportional to the temperature difference described in Equation 2.1, α is the Seebeck coefficient.

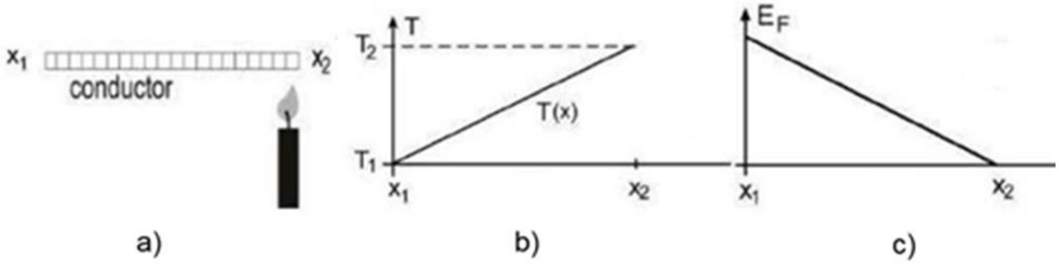

Figure 2.13 Fermi Energy for Heated  Electric Conductor a) Electric Conductor (n Type) with One End Heated b) Temperature Profile along the Conductor c) Profile of the Fermi energy for Electron Conductivity in an n Type Semiconductor (Fahrner & Schwertheim, 2009)

$$V_S = -\alpha(T_2 - T_1) = -\alpha\Delta T \qquad (2.1)$$

For a complete device of thermoelectric generator, carrier distributions and the resulting potential difference in the p and n type thermoelectric generator legs are shown in Figure 2.14. The Seebeck coefficient $\alpha_{AB}$ for the combination of two semiconductors, A and B, is called the relative Seebeck coefficient (Equation 2.2). Normally, two materials with Seebeck coefficients of different signs are chosen in order to gain an accordingly large voltage. In order to increase the output voltage or output power, many thermoelectric generators together are connected in series as shown in Figure 2.15.

$$V_{AB} = (\alpha_B - \alpha_A)\Delta T = \alpha_{AB}\Delta T \qquad (2.2)$$

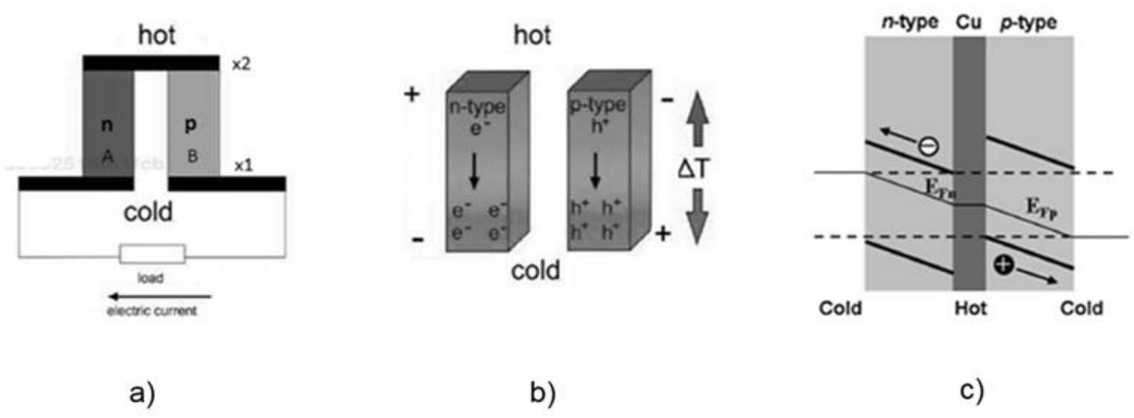

Figure 2.14 Band Structure of Thermoelectric Generator a) n Type/p Type Thermoelectric Generator b) Carrier Distributions in the n/p Thermoelectric Generator Legs(Fahrner & Schwertheim, 2009) c) Band Structure of n/p Thermoelectric Generator (Park et al., 2013)

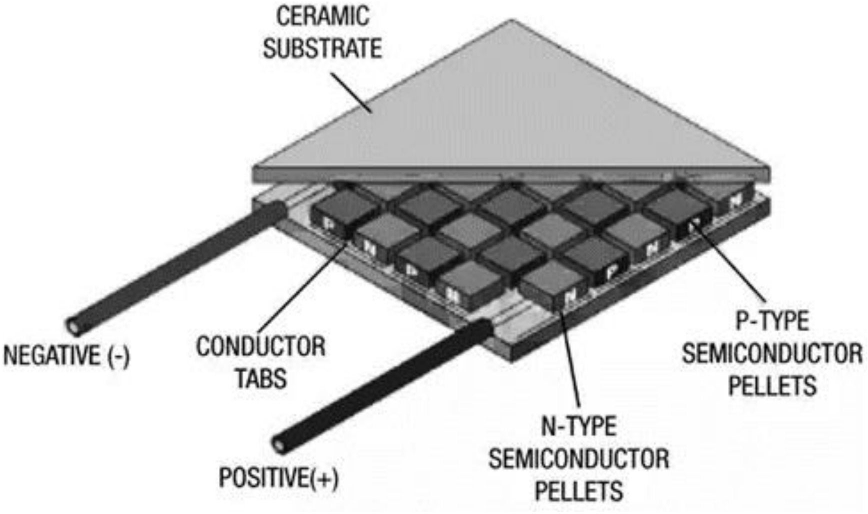

Figure 2.15 Thermoelectric Generator Array (“Thermoelectric Energy Harvesting | DigiKey,” n.d.)

Figure of merit is used to characterize the thermoelectric materials, which is important to get high performance TEGs. A high temperature difference is critical for a high Seebeck voltage. In order to maintain this high temperature difference, the thermal conductivity λ of the thermoelectric material should be as small as possible. The definition of the thermal conductivity is described by Equation 2.3. Also, the materials with high electrical conductivity is required so that the generated energy is not lost in the form of joule heat. Z and ZT are figures of merit to characterize the thermoelectric materials as described in Equation 2.4 and Equation 2.5. With higher Seebeck coefficient, higher electrical conductivity, and lower thermal conductivity, figure of merit is higher. Temperature dependency of ZT for some materials are in Figure 2.16.

$$\mathrm{jQ} = \frac{\mathrm{dQ}}{\mathrm{dA}} = \lambda \frac{\mathrm{dT}}{\mathrm{dx}} \tag{2.3}$$

jQ is the heat flux, A is the cross section of the conductor (perpendicular to the heat flux), Q is the heat quantity, and λ is the material dependent thermal conductivity, dim(λ)=W/K m.

$$Z = \frac{\alpha^2 \sigma}{\lambda} \tag{2.4}$$

$$ZT = \frac{\alpha^2 \sigma}{\lambda} T \tag{2.5}$$

α is the Seebeck coefficient, $\sigma$ is the electrical conductivity, λ is the thermal conductivity.

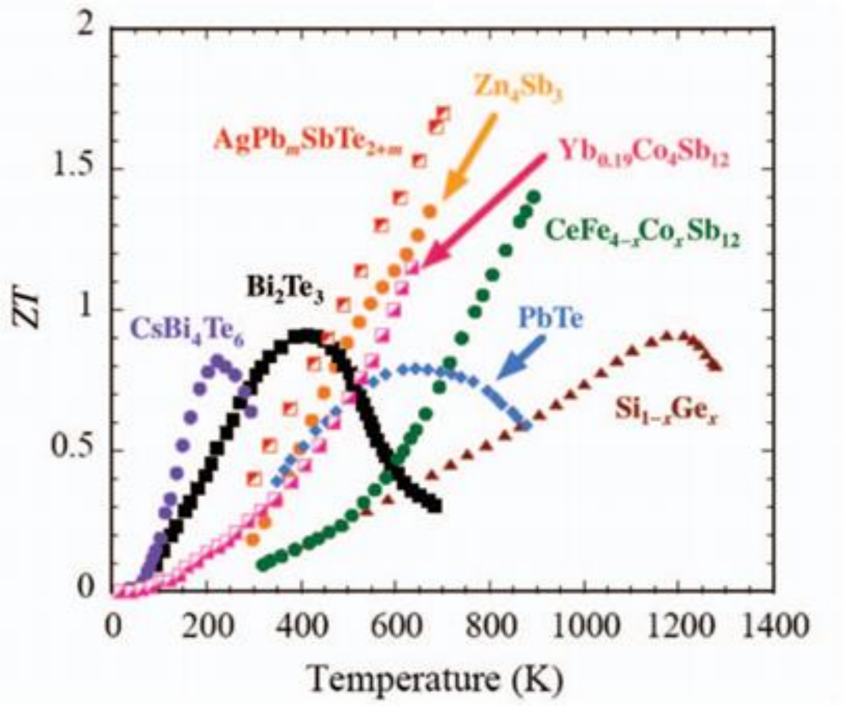

Figure 2.16 Temperature Dependency of ZT for Common Materials (Tritt & Subramanian, 2006)

2.4 Heat Transfer Simulation

The structure of the foldable thermoelectric generators was designed as shown in Figure 2.17. It consists of rigid thermoelectric material bismuth telluride (Bi2Te3) of both p type and n type. Metals of copper (Cu) and gold (Au) are used for the top electrodes and the bottom electrodes. The whole structure is packed by the parylene C film to realize its flexibility. It is like a mango with vertical and horizontal cuts as shown in Figure 2.18. Each cube of the mango stands for one pair of p and n legs of the device and the whole device can be bended along between individual pairs. Since the top parylene C film layer and the bottom parylene C film layer are of same thickness(15um), the metal is located at the mechanical neutral plane and won't suffer from tensile strain or compressive strain when it is bended so it won't be damaged(D.-H. Kim et al., 2008).

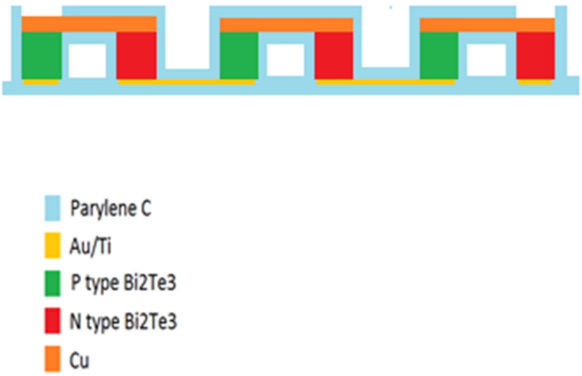

Figure 2.17 Device Structure of the Flexible Thermoelectric Generators

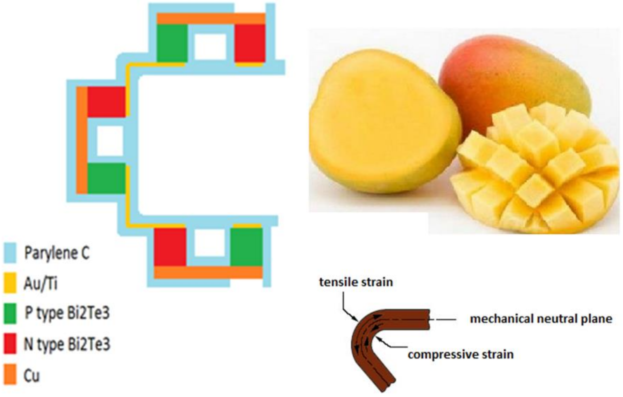

Figure 2.18 Flexibility of the Thermoelectric Generators

Heat transfer simulation of the device was conducted by using the software of COMSOL. The device was first simplified by using only one of the bismuth telluride pellets for the simulation as shown in Figure 2.19. The dimension of the bismuth telluride pellets is 1.4mmx1.4mmx1.1mm. The bismuth telluride pellet is covered by 15um parylene C film and metal connection is ignored. The bottom surface is the hot side with a temperature of 80 °C. All other surfaces are exposed in the air at room temperature. Since the Seebeck voltage is proportional to the temperature difference between the hot side and the cool side of the bismuth telluride pellet, temperature gradient across the pellet is simulated under different conditions, which is discussed in following part of this chapter.

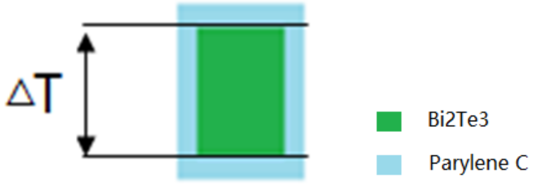

Figure 2.19 Single Bismuth Telluride Pellet Used for Simulation

As shown in Figure 2.20, a path AB is defined, where A is the center point of top surface of the Be2Ti3 pellet and B is the center point of the bottom surface. Figure 2.21 shows surface temperature for the model shown in Figure 2.20 and the Figure 2.22 shows its isosurface temperature. The temperature difference across the height (path AB) of the Be2Ti3 pellet is around 3.5°C as shown in Figure 2.23.

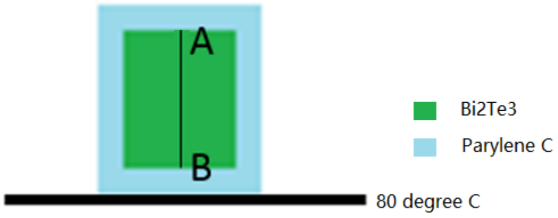

Figure 2.20 Single Bismuth Telluride Pellet Model with Path AB Defined

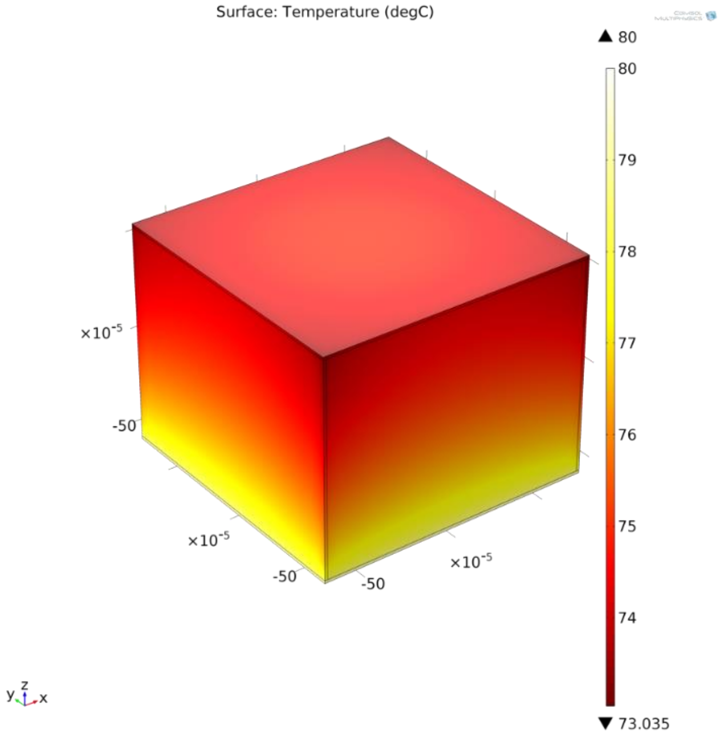

Figure 2.21 Simulated Surface Temperature for the Model Shown in Figure 2.17

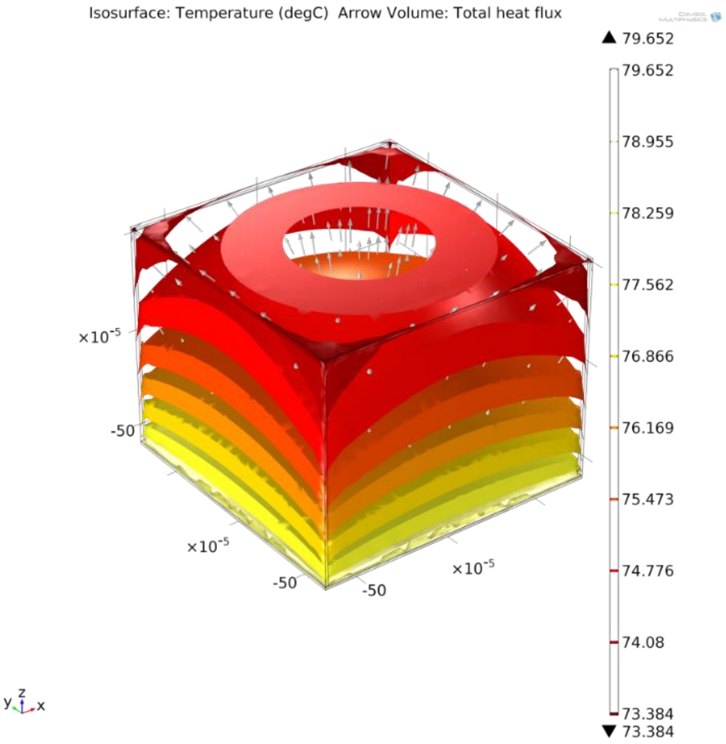

Figure 2.22 Simulated Isosurface Temperature for the Model Shown in Figure 2.17

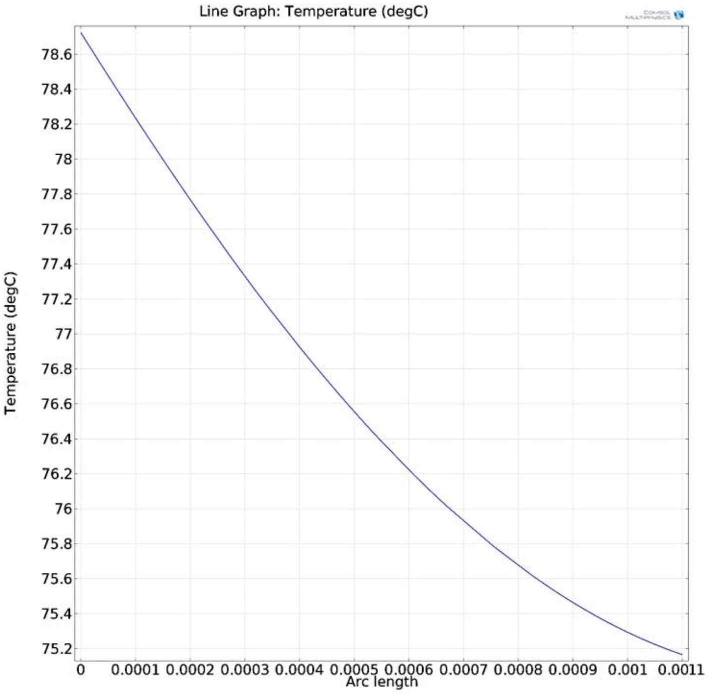

Figure 2.23 Simulated Temperature Gradient for the Model Shown in Figure 2.17

If top layer parylene C film is removed and instead a layer of 150 um thick copper is used as a heat sink (Figure 2.24), the simulated surface temperature, isosurface temperature and temperature gradient are shown in Figure 2.25, Figure 2.26 and Figure 2.27. The results show that there is not much improvement in the temperature difference across the $Bi_2Te_3$ pellet because the surface area is very small for heat dissipation despite copper has very good thermal conductivity.

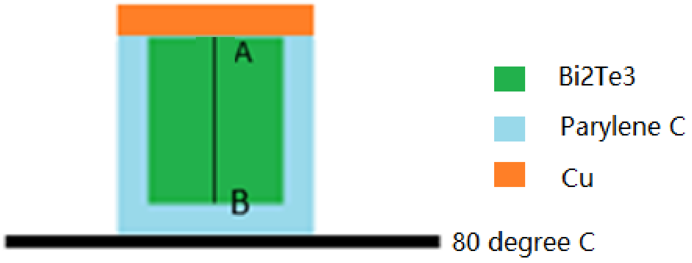

Figure 2.24 Single Bismuth Telluride Pellet with Copper Heat Sink

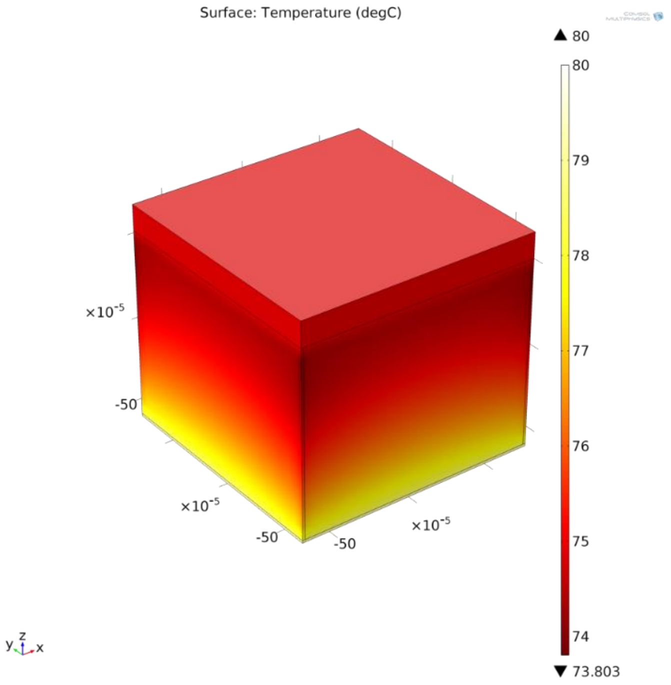

Figure 2.25 Simulated Surface Temperature for the Model Shown in Figure 2.21

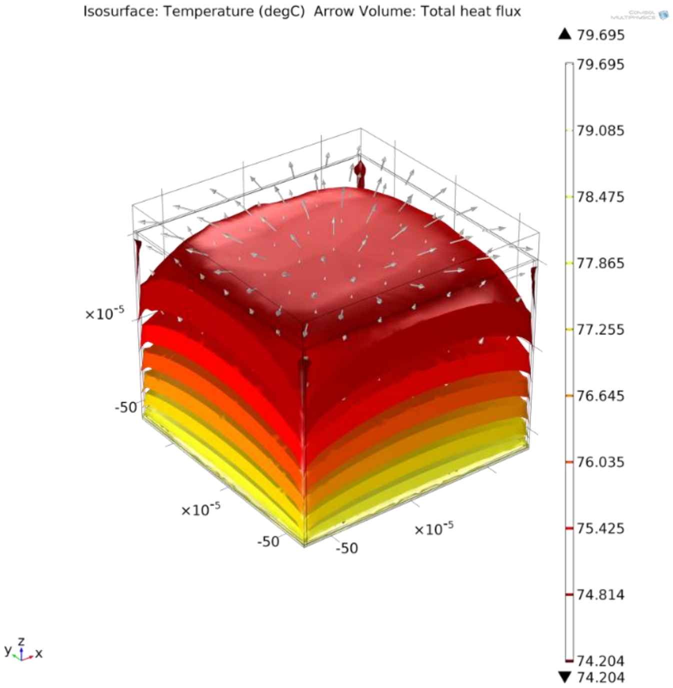

Figure 2.26 Simulated Isosurface Temperature for the Model Shown in Figure 2.21

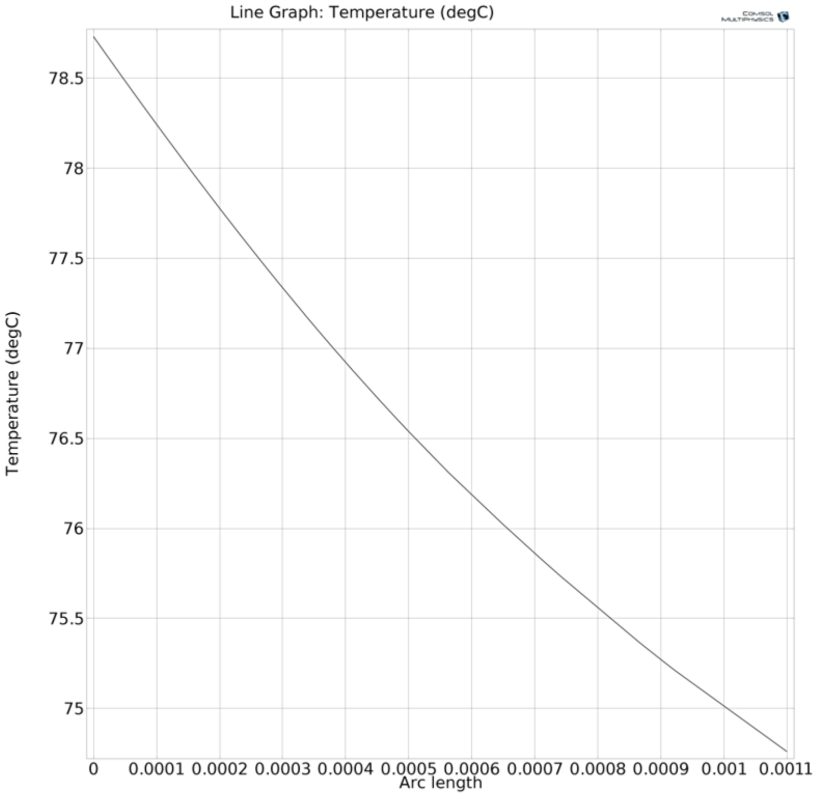

Figure 2.27 Simulated Temperature Gradient for the Model Shown in Figure 2.21

In order to explore the role that parylene C film has played in heat transfer, bare $Be_2Ti_3$ pellet was used for the simulation as shown in Figure 2.28. The results (Figure 2.29, Figure 2.30 and Figure 2.31) didn't show much change of the temperature difference. Although parylene C has a relatively low thermal conductivity as a type of polymer, the thickness of the film is pretty thin, only 15um, which does not affect too much on the heat dissipation from the $Be_2Ti_3$ pellet surface.

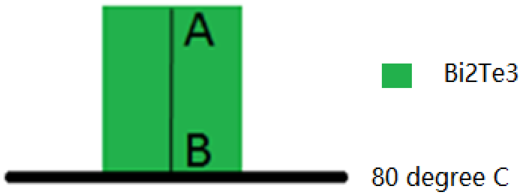

Figure 2.28 Single Bare Bismuth Telluride Pellet

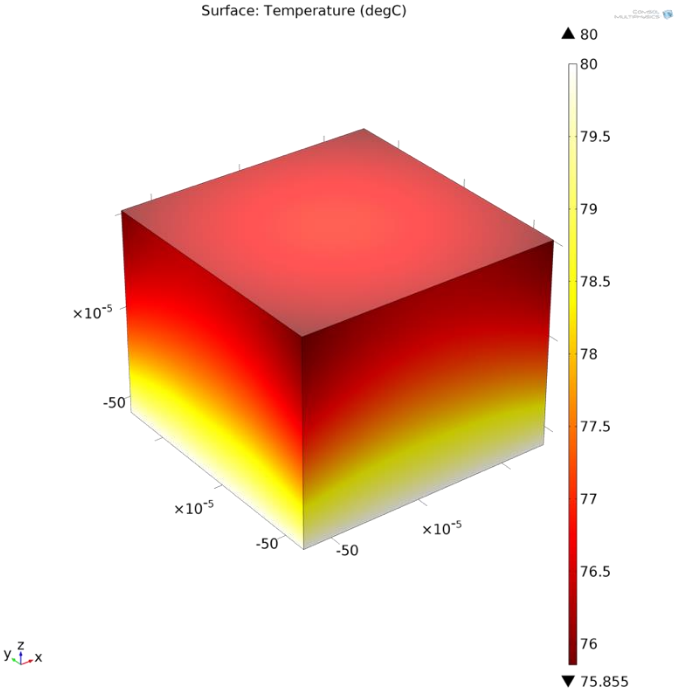

Figure 2.29 Simulated Surface Temperature for the Model Shown in Figure 2.25

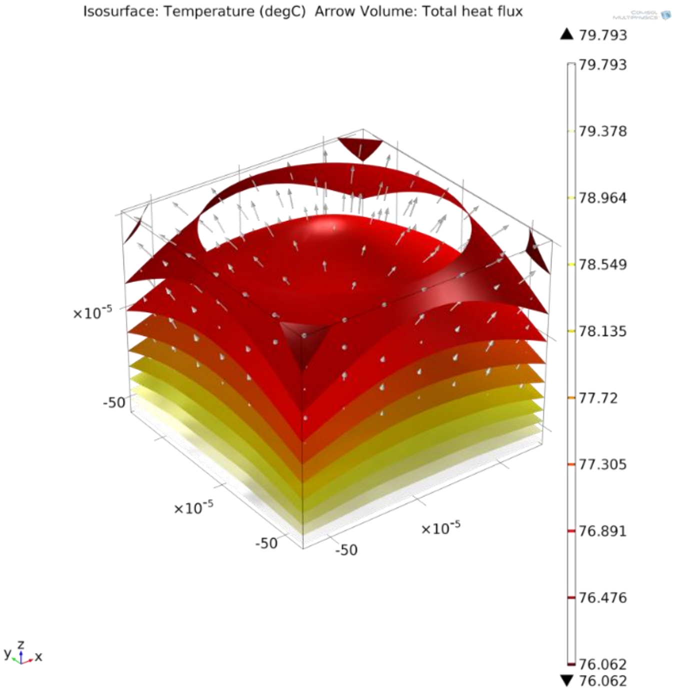

Figure 2.30 Simulated Isosurface Temperature for the Model Shown in Figure 2.25

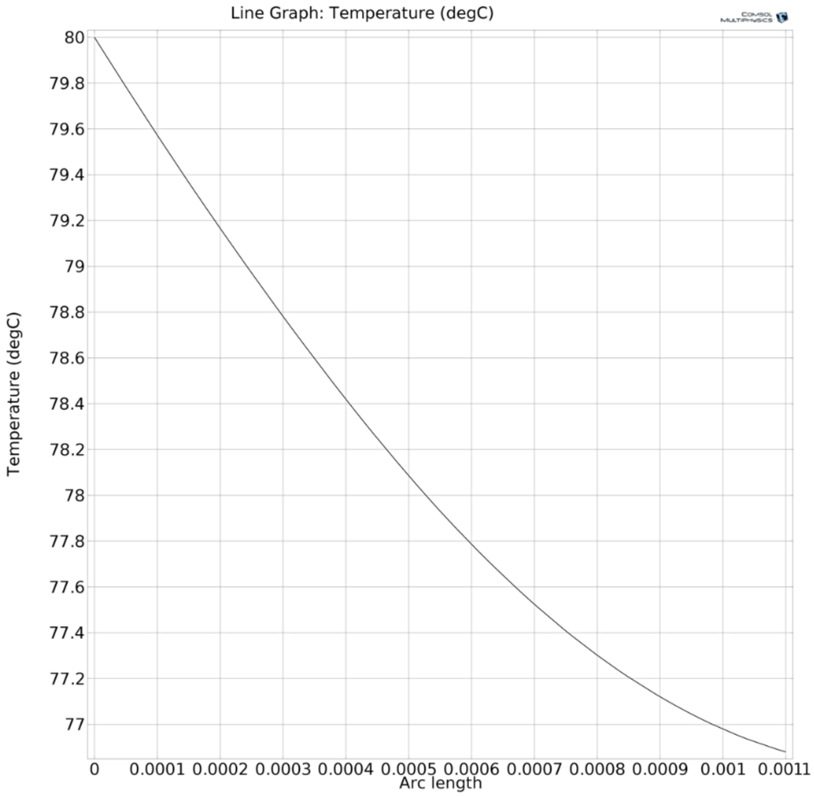

Figure 2.31 Simulated Temperature Gradient for the Model Shown in Figure 2.25

In the simulation above, only external natural convective cooling of the surfaces is considered. With the surface to ambient radiation included for the simulation model in Figure2.20, the results are as Figure 2.32, Figure2.33 and Figure 2.34. Based on the simulation results, radiation can be ignored since the surface emissivity is around 0.34. Only when surface emissivity is large, close to 1, radiation should be considered.

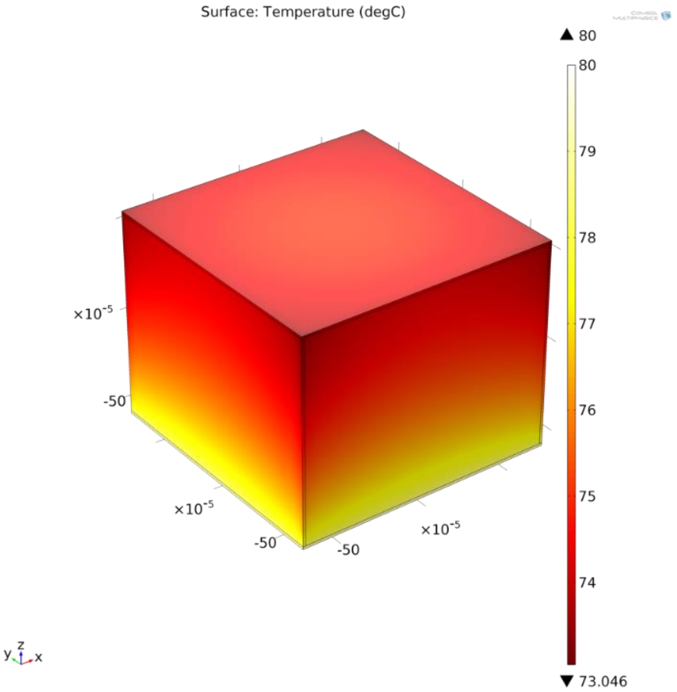

Figure 2.32 Simulated Surface Temperature for the Model Shown in Figure 2.17 with Surface to Ambient Radiation Considered

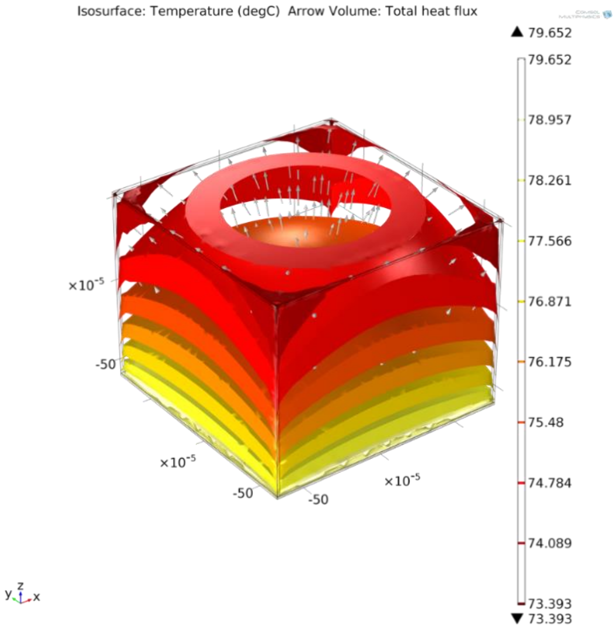

Figure 2.33 Simulated Isosurface Temperature for the Model Shown in Figure 2.17 with Surface to Ambient Radiation Considered

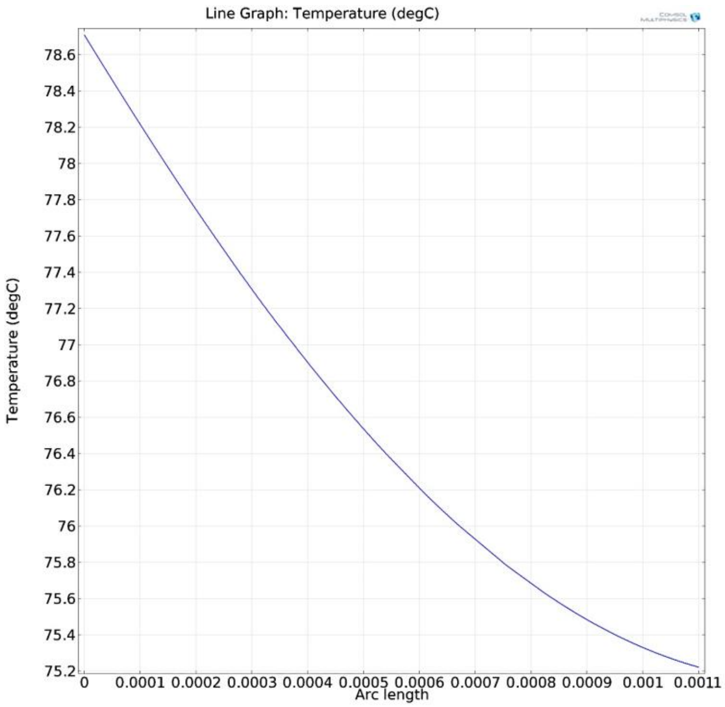

Figure 2.34 Simulated Temperature Gradient for the Model Shown in Figure 2.17 with Surface to Ambient Radiation Considered

Based on the above simulations, complete device model building and heat transfer simulation were done. Figure 2.35 shows the device model which consists of the thermoelectric material bismuth telluride pellets, metal connections of both top and bottom electrodes and the parylene C film package of the device. No additional metal heat sink was used. External natural convection cooling was considered for the simulation while surface to ambient radiation is ignored. The bottom side of the device is placed on a hot surface of 80 °C and all sides are exposed in the air under room temperature. Figure 2.36 shows the surface temperature and Figure 2.37 shows the isosurface temperature of the device from the simulation. Figure 2.38 shows the temperature distribution across the materials. The temperature gradient between the bismuth telluride pellets is around 5°C when hot plate surface temperature is set to 80 ° C. Based on the simulation, the bismuth telluride pellets of only 1.1mm height can give a temperature difference of 5°C. The area of individual bismuth telluride pellet is also quite small (1.4mmx1.4mm); therefore, large amount of bismuth telluride pellets can be integrated to get a high output power.

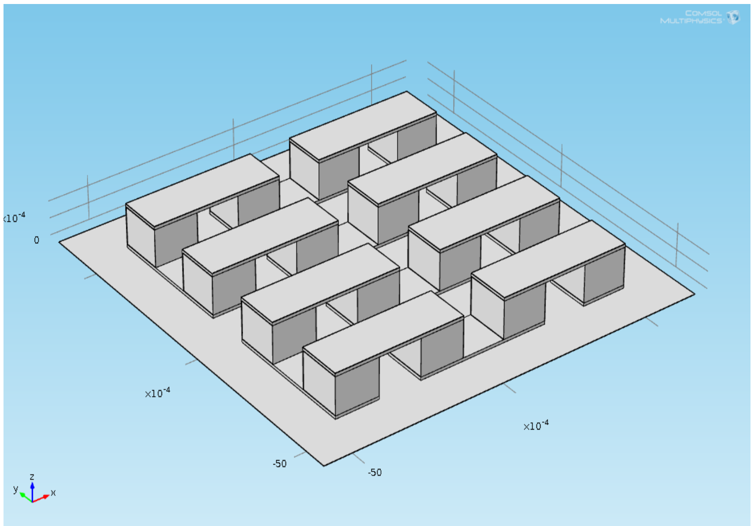

Figure 2.35 Device Model of Thermoelectric Generator Array

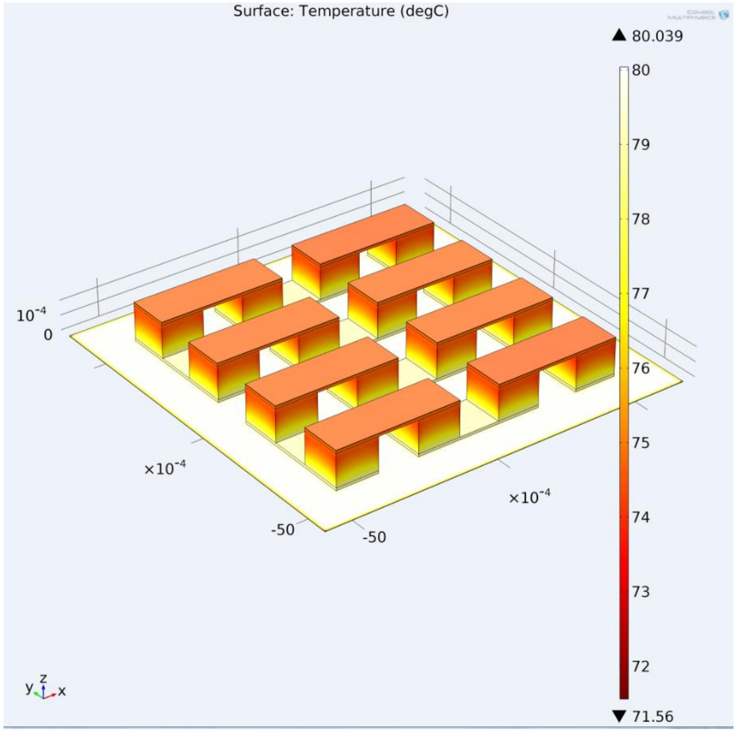

Figure 2.36 Simulated Surface Temperature for the Thermoelectric Generator Array

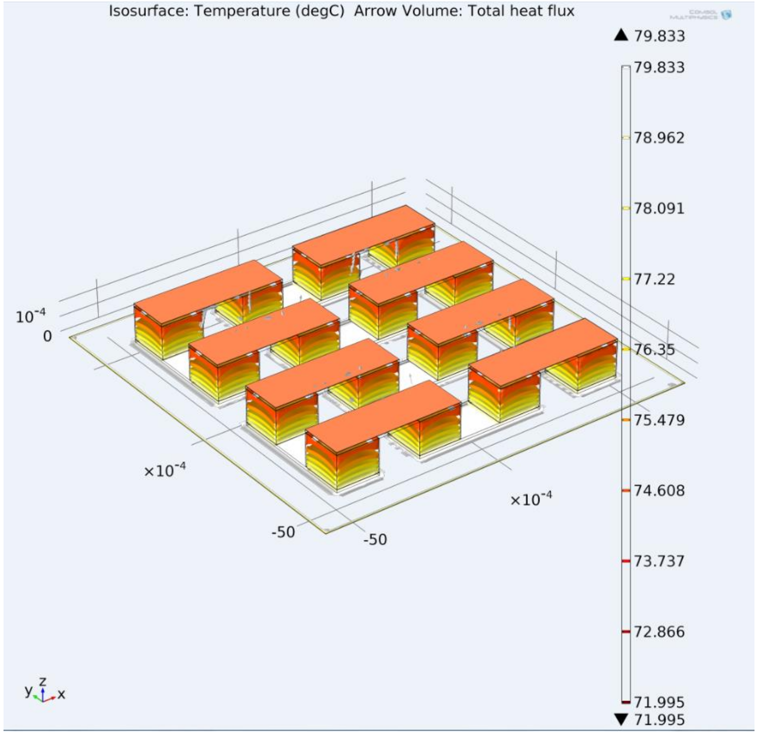

Figure 2.37 Simulated Isosurface Temperature for the Thermoelectric Generator Array

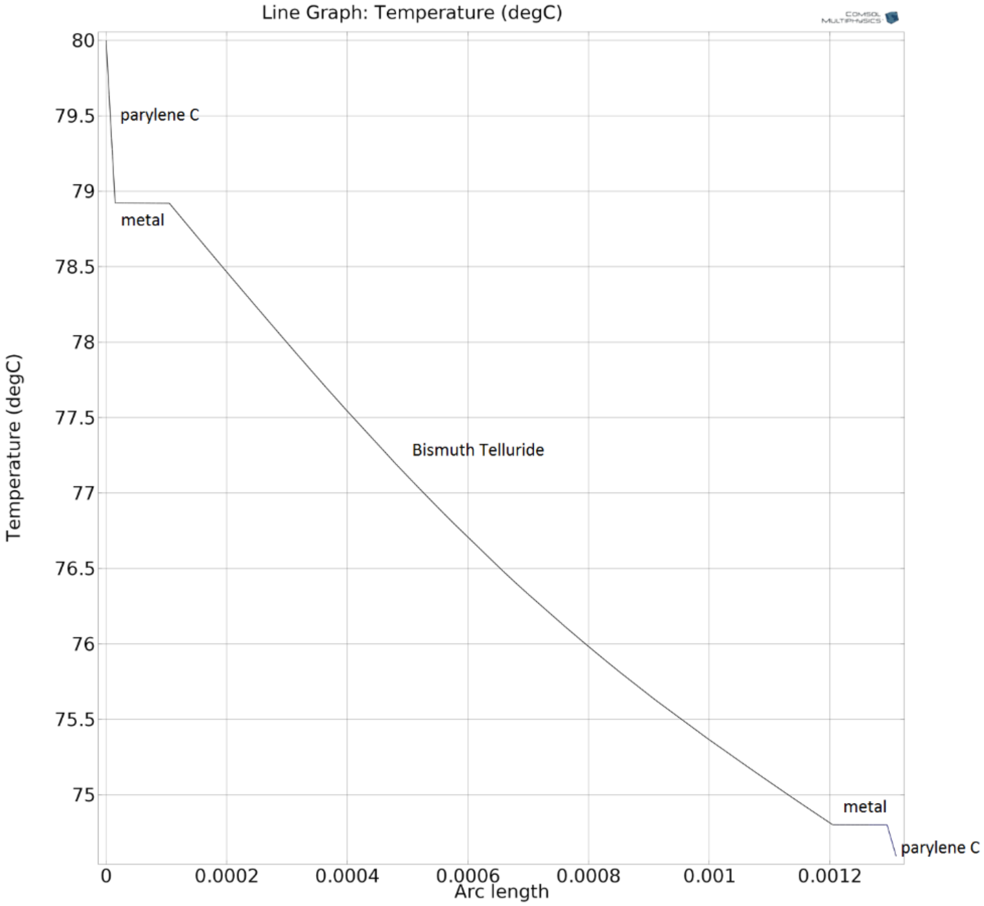

Figure 2.38 Simulated Temperature Distribution across the Material of the Thermoelectric Generator Array

# CHAPTER 3

# FABRICATION OF FLEXIBLE THERMOELECTRIC GENERATORS BASED ON MEMS TECHNOLOGY

## 3.1 Fabrication Flow Design of Flexible Thermoelectric Generators

Traditional thermoelectric material bismuth telluride ($Bi_2Te_3$) of p type and n type were chosen for the fabrication in order to achieve high thermoelectric efficiency. MEMS technology and thin film technique were used for the fabrication process. The small bismuth telluride pellets (1.4x1.4x1.1mm) were purchased from Everredtronics (Figure 3.1). Table 3.1 shows the specifications of the bismuth telluride pellets. Figure 3.2 shows the fabrication flow of flexible thermoelectric generators. First, the silicon substrate is pre-cleaned, then a thick layer of photoresist (5um) is deposited. In Step 3, a layer of parylene C film(15um) is deposited on top of the photoresist. In Step 4 and Step 5, another layer of photoresist is deposited and patterned with photolithography technology that discussed in Chapter 1.In Step 6, a layer of metal (Gold/Titanium ,3000A/300A) is deposited. Titanium is used for good adhesion between the parylene C film and the gold layer. With the process of lift off in Step 7, the bottom electrodes form. Then in Step 8 the Be2Te3 pellets of both P type and N type are mounted on the bottom electrodes using Ag paste. After that we mount the Cu chips on the Be2Te3 pellets in Step 9 to form the top electrodes.  In Step 10 a second layer of parylene C film is deposited, which is also 15um thick. In Step 11 and Step 12, the sample is placed in the environment of oxygen plasma (RIE) and a shadow mask is used to etch parts of the parylene C film surface to open the electric contacts. In the last step, the parylene C film along the edge of the substrate is cut to expose the under layer photoresist and with soaking process in acetone, the flexible structure packed by parylene C film is lift off.

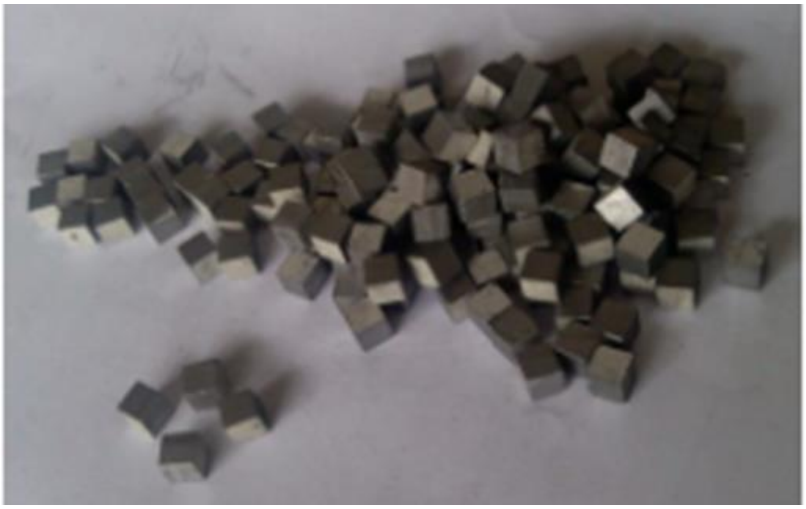

Figure 3.1 Bismuth Telluride Pellets (1.4x1.4x1.1mm) Purchased from Everredtronics

Table 3.1 Specifications of the Bismuth Telluride Pellets

| P-type crystals: | N-type crystals: |
|---|---|
| 1. Purity: 99.99%<br>2. Thermal conductivity (k): 1.2-1.6w/m.K<br>3. Seebeck (S) : 200-230 uV<br>4. Electrical conductivity (rou): 850-1250<br>5. Figure of merit (Z): 2.55- $3.4\times10^{-3}K^{-1}$<br>6. ZT>=1.1@300K | 1. Purity: 99.99%<br>2. Thermal conductivity (k): 1.2-1.6w/m.K<br>3. Seebeck (S) : 205-235 uV<br>4. Electrical conductivity (rou): 950-1250<br>5. Figure of merit (Z): 2.34-$3.2\times10^{-3}K^{-1}$<br>6. ZT>=1.0@300K |

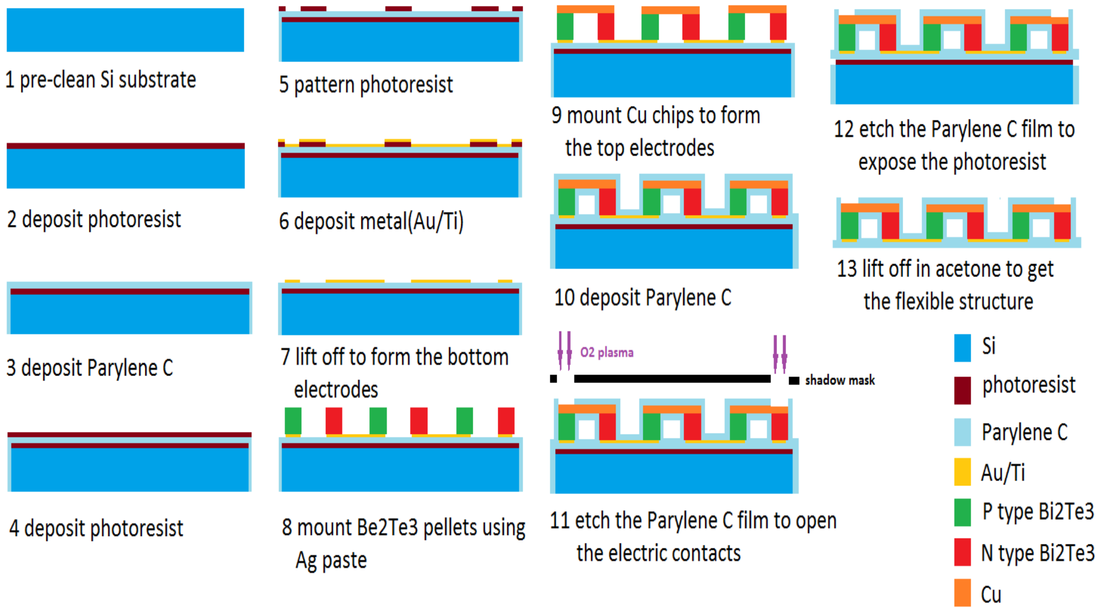

Figure 3.2 Fabrication Flow of Flexible Thermoelectric Generators

### 3.2 Experiment Process

Fabrication process for the flexible thermoelectric generator array is illustrated in Figure 3.3 with the help of actual experimental photos. The whole fabrication process was done in ASU Nanofab. After the photoresist and the parylene C film was deposited on the silicon substrate, Au/Ti (3000A/300A) was deposited on the parylene C film to form the bottom electrodes, as shown Figure 3.3 (a). Figure 3.3 (b) shows the bismuth telluride pellets are mounted on the bottom electrodes using silver paste and the paste was cured by overnight 80 °C baking. Bismuth telluride pellets used here were pre-processed by depositing a layer of nickel 200 nm by electron beam evaporation on the contact areas in order to reduce the contact resistance(Iyore et al., 2009; S. J. Kim et al., 2014). Figure3.3 (c) shows the copper chips were boned on the bismuth telluride pellets with silver paste to form the front electrodes.  Another layer of parylene C film was deposited so that the whole structure is packed by the flexible film. Also, parylene C film was etched for openings so the front electrodes are exposed for circuit connection. Finally, the surface of the parylene C film was cut through along some lines so that the under layer photoresist is exposed and dissolved in the acetone and the flexible device can be lift off from the rigid silicon wafer substrate as shown in Figure3.3(d).

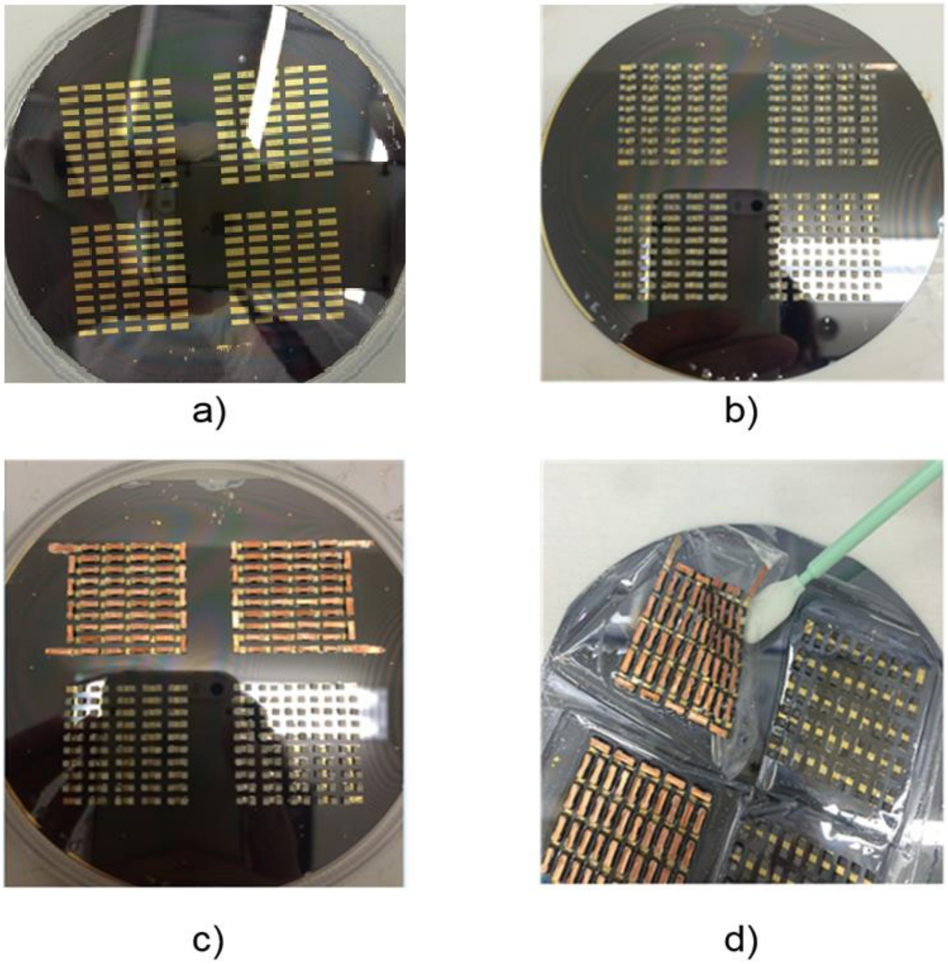

Figure 3.3 Fabrication Process Photos of the Flexible Thermoelectric Generator Array a) Bottom Electrodes Deposited on the Substrate b) Bismuth Telluride Pellets Mounted on the Bottom Electrodes c) Front Copper Electrodes Mounted on the Bismuth Telluride Pellets d) Flexible Thermoelectric Generator Arrays Lift off from the Rigid Substrate

One of the fabricated devices is shown in Figure 3.4. It has 40 pairs of p and n thermoelectric legs. It is only a little bigger than a US quarter coin and it is quite flexible and can be rolled around a rod as shown in Figure 3.5.

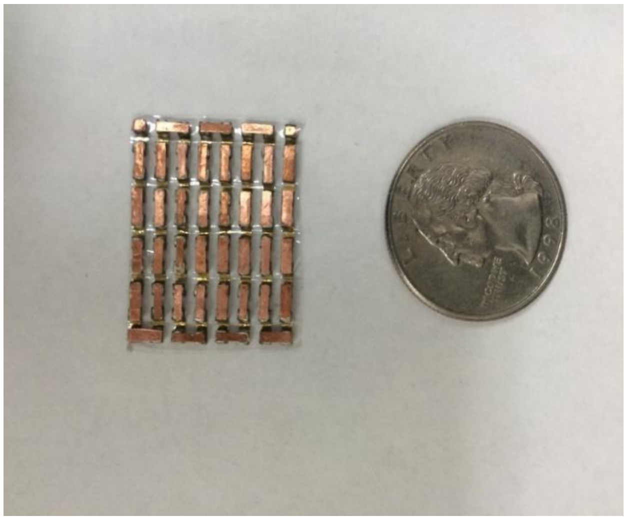

Figure 3.4 Fabricated Thermoelectric Generator Array with its Size Comparable to a US Quarter

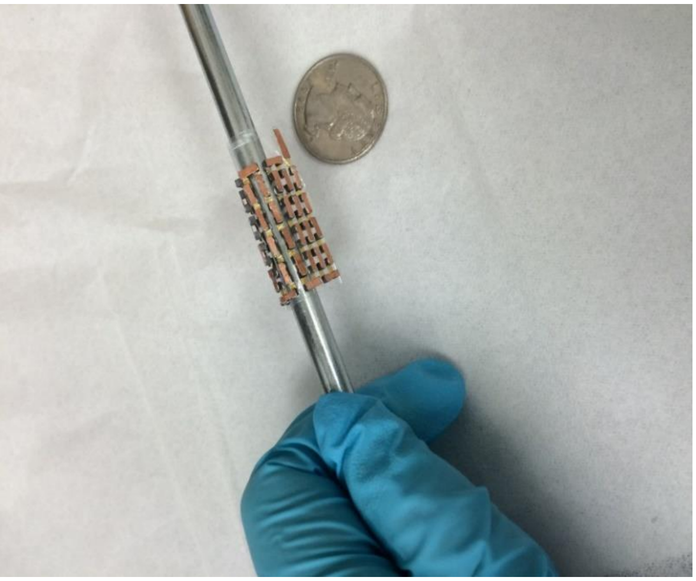

Figure 3.5 Fabricated Flexible Thermoelectric Generator Array Rolled around a Rod

## 3.3 Test Results

The setup for the test is shown Figure 3.6. The device was placed on the hotplate surface flatly with the top surface exposed in the air under room temperature. The hotplate surface temperature was increased to 40°C, 50°C, 60°C, 70°C and 80°C. At each temperature, a multi-meter was used to measure the generated open circuit output voltage and the short circuit current of the device. The results were recorded in Table 3.2. Six samples of different size were tested.  Sample 6 has 40 pairs of p/n thermoelectric legs as shown in Figure 3.4. Other samples either have 35 pairs or 25 pairs p/n thermoelectric legs. The resistance of each sample at room temperature was also measured.

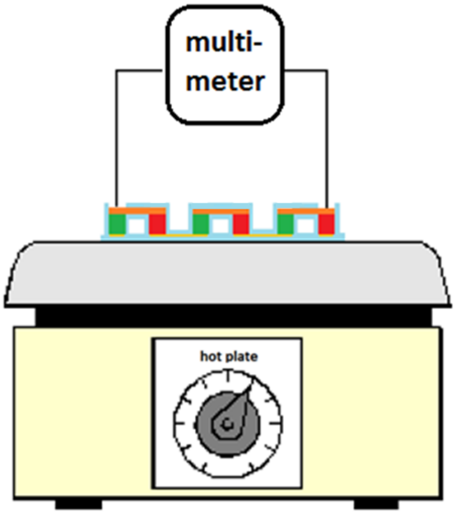

Figure 3.6 Setup for Sample Test

Table 3.2 Test Results for Six Fabricated Flexible Thermoelectric Generator Arrays

| Sample# | # of pellets pairs | Resistance at room temperature(Ω) | Sample area($cm^2$) | Temperature (°C)<br>Output | 40 | 50 | 60 | 70 | 80 |
|---|---|---|---|---|---|---|---|---|---|
| #1 | 25 | 22.9 | 3.3516 | Voltage(mv) | 2.6 | 5.1 | 9.4 | 14 | 18.8 |
| | | | | Current(mA) | 0.07 | 0.15 | 0.27 | 0.37 | 0.43 |
| #2 | 25 | 21.1 | 3.3516 | Voltage(mv) | 2.0 | 4.5 | 9.3 | 13.0 | 17.6 |
| | | | | Current(mA) | 0.08 | 0.19 | 0.33 | 0.41 | 0.53 |
| #3 | 35 | 26.5 | 4.8412 | Voltage(mv) | 3.1 | 7.1 | 12.3 | 16.8 | 22.3 |
| | | | | Current(mA) | 0.08 | 0.17 | 0.28 | 0.38 | 0.47 |
| #4 | 35 | 26.8 | 4.8412 | Voltage(mv) | 3.6 | 7.2 | 13.0 | 17.0 | 22.9 |
| | | | | Current(mA) | 0.11 | 0.19 | 0.29 | 0.41 | 0.51 |
| #5 | 35 | 26.3 | 4.8412 | Voltage(mv) | 3.5 | 7.6 | 12.3 | 16.0 | 21.4 |
| | | | | Current(mA) | 0.11 | 0.22 | 0.37 | 0.46 | 0.62 |
| #6 | 40 | 30.2 | 5.586 | Voltage(mv) | 3.6 | 8.8 | 14.0 | 19.3 | 25.0 |
| | | | | Current(mA) | 0.1 | 0.17 | 0.27 | 0.37 | 0.52 |

The voltage output with the hot plate surface temperature is plotted in Figure 3.7, which shows that higher temperature leads to higher voltage output and samples with more pairs of p/n thermoelectric legs have higher voltage output. For example, Sample #6, which has 40 pairs of thermoelectric legs gave highest output voltage (25 millivolts) when the hotplate surface temperature is 80 °C. Figure 3.8 shows the output current with the temperature. Higher temperature also leads to higher current output. However, samples with more p/n legs do not always have higher output current because the output current is not only related to the generated voltage but also related to the internal resistance of the device. Contact resistance between the thermoelectric material and the metal contributes most part of the total internal resistance. It is very critical to reduce the contact resistance, otherwise, the generated power will be lost in the form of Joule heat.

With the output voltage and current, the output power was calculated (Figure 3.9). At 80 °C, sample 5 has the output power of around 3.5uw, which is pretty enough to activate a micro temperature sensor or CMOS image sensor(P. Chen, Chen, Wang, & Chen, 2009; S. Hanson, Foo, Blaauw, & Sylvester, 2010). Also, output power per unit area for each sample was calculated shown in Figure 3.10. Sample 2 with an area of 3.3516 cm$^2$ has the best performance with an approximate output power per unit area of 7mW/m$^2$. The output power per unit area for some of the samples are overlapped, which shows they have good product consistency. Good product consistency is very important for commercializing the research devices.

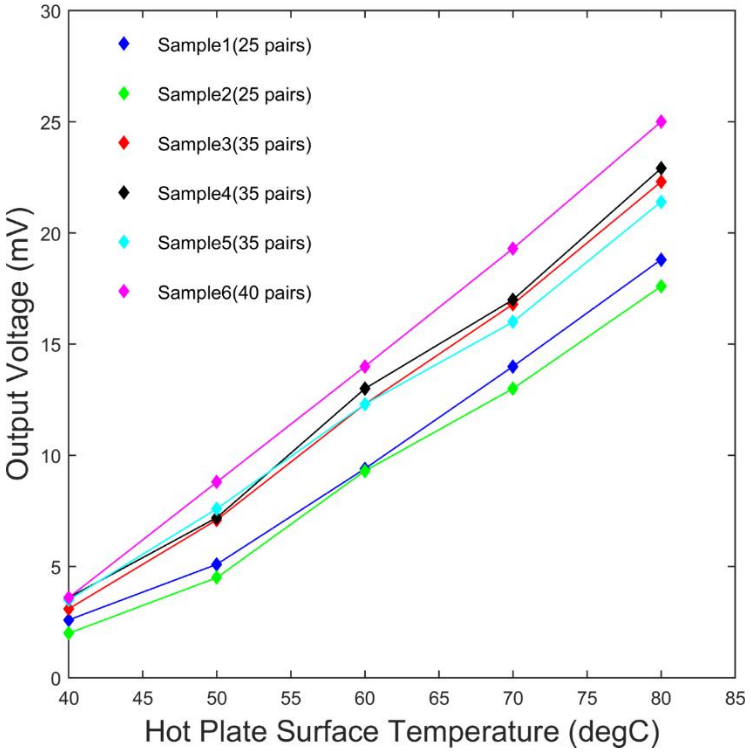

Figure 3.7 Output Voltages of Samples at Different Temperatures

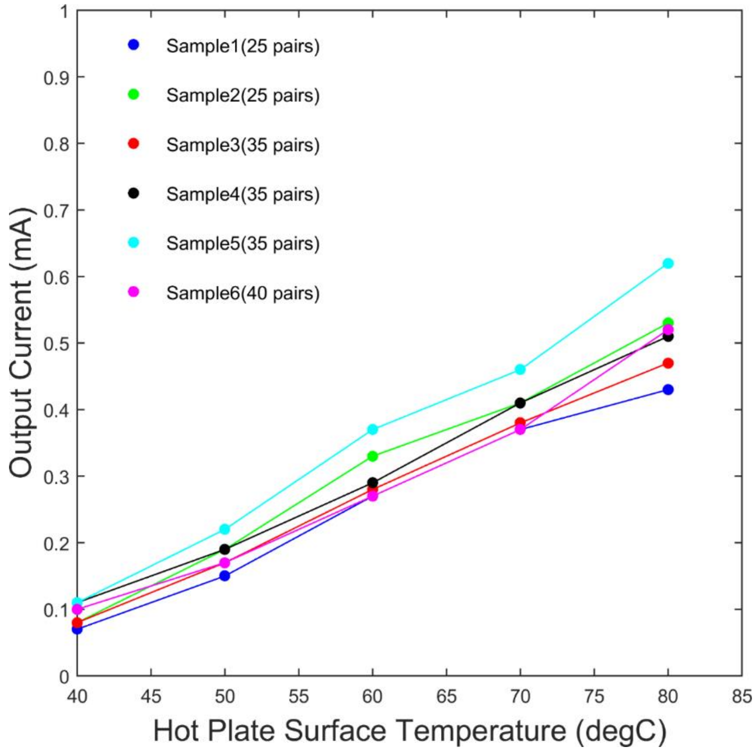

Figure 3.8 Output Currents of Samples at Different Temperatures

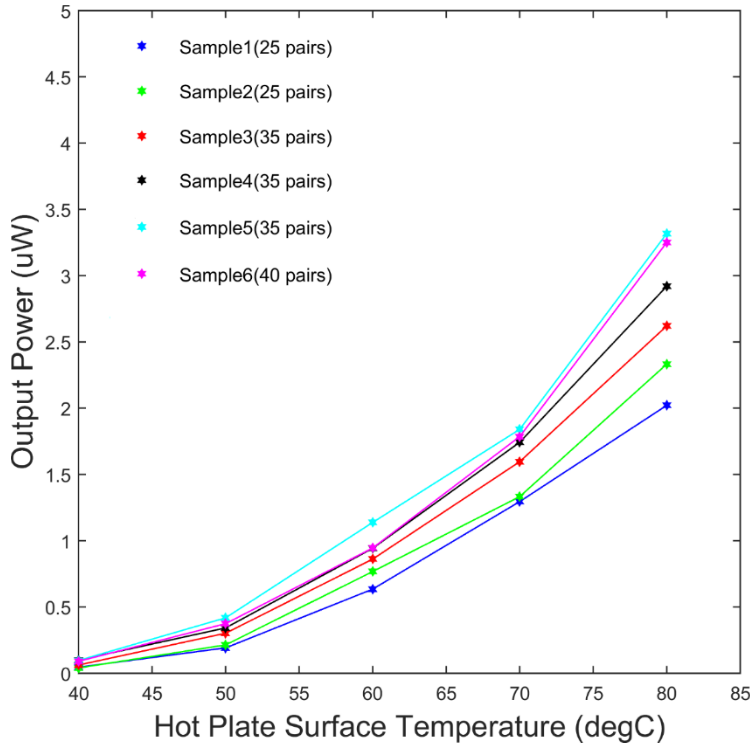

Figure 3.9 Output Powers of Samples at Different Temperatures

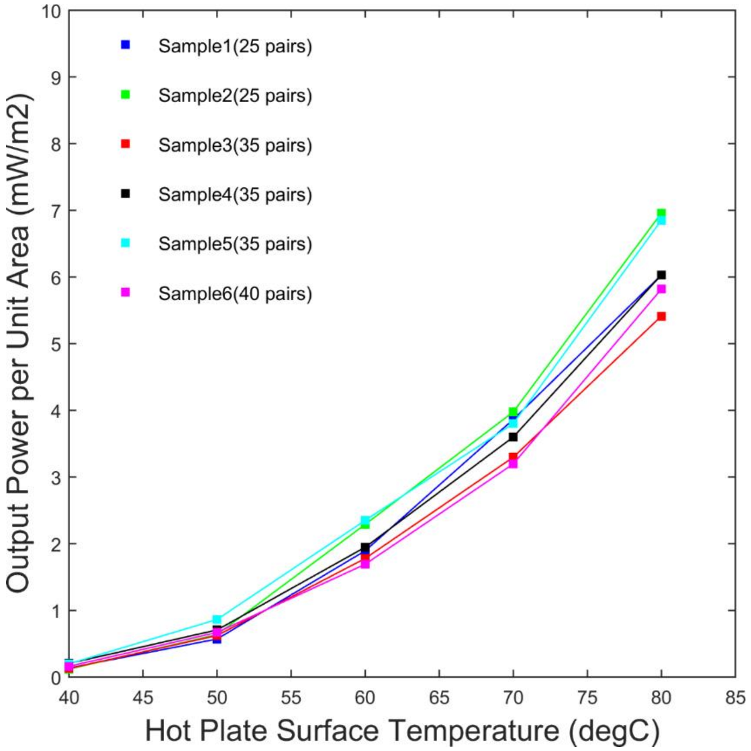

Figure 3.10 Output Powers per Unit Area of Samples at Different Temperatures

## 3.4 Flexibility Test and Discussion

The flexibility of the fabricated TEGs was investigated by measuring the resistance of the samples when they were completely folded (not just bended) as shown in Figure 3.11. Sample 1 and Sample 2 with an original resistance of 22.9Ω and 21.1Ω were folded and the resistance was re-measured in room temperature. The result is 21.3 Ω and 20.0 Ω and therefore did not show any increase in resistance. This leads to the conclusion that the metal connections are well protected by the two layers of parylene C films of the same thickness and the fabricated thermoelectric generator arrays are of high flexibility.

Figure 3.11 Folded Thermoelectric Generator Array

Based on the simulation when hot side temperature of the thermoelectric generator array is 80°C and all other surfaces are exposed in the air under room temperature, the temperature difference across the bismuth telluride material is only around 5 °C. With this very small temperature difference, Sample2 gives output power per unit area of 7mW/m$^2$. In real application, there is only hot surface and the cold surface does not usually exist. The cold surface is in the air and only small temperature difference across the thermoelectric material exists. Therefore, it is important to get high thermoelectric efficiency under small temperature difference.  Also, the fabricated TEGs show super high flexibility. The devices didn't damage with bending or folding. MEMS thin film technique used in this work allows deposition of very thin Parylene C film, which not only enables the high flexibility of the device but also achieves effective heat transfer to get high thermoelectric efficiency. These show great improvement compared with previous works(S. J. Kim et al., 2014; Suemori et al., 2013).

The fabricated flexible thermoelectric generators will be very favorable for energy harvesting from ambient. They will work better outdoors than indoors because of the stronger air convection outdoors. With the thin film techniques, large area of flexible thermoelectric generator arrays with high output power can be fabricated in industry. Also, with the development of technology for ultra-low power sensor nodes (Arms, Townsend, Churchill, Galbreath, & Mundell, 2005), these flexible thermoelectric generator arrays show great promise for self-powered wireless sensor notes. Besides their application in environmental data collection, they can also be used for wearable electronics, wireless biosensor networks for human health monitoring, automotive waste heat recovery, home co-generation of heat and electricity and space probes.

Future work should focus on reducing the contact resistance between the thermoelectric material and the metal, and exploring and using other types of film materials that can substitute parylene C to tolerate high temperature fabrication process.

# CHAPTER 4

# WORKING PRINCIPLES AND FABRCATION OF 2-D GRAPHENE PH SENSORS

## 4.1 State-of-Art pH Sensors

pH equals the inverse of the logarithm to the base10 of the hydrogen ion activity .The three main ways of pH sensing are: pH paper, electrode, optode. They are summarized in Table 4.1. The accuracy of pH paper is very low, only for general visual check. Optode, besides its high cost and limited dynamic range, it cannot be used in the field because of the complex optical facilities. Therefore, the best current choice for field measurement of pH is using electrodes in spite of their disadvantages.

Table 4.1 Comparison of Different pH Sensing Methods

| | Dynamic Range | Accuracy | Cost | Limitations |
|---|---|---|---|---|
| pH paper | very limited | General visual check | None | General visual check |
| Electrode | pH0~pH14 | 0.01pH unit | Moderate | Delicate assembly<br>Salinity dependent |
| Optode | Limited to about 4 pH units | 0.01pH unit | High | Limited range<br>High cost<br>Salinity dependent<br>Photo leaching drift<br>Storage conditions |

Two common types of pH electrodes are ISE (Ion Selective Electrodes) and ISFET (Ion Sensitive Field-Effect Transistor). Figure 4.1 shows the basic components of ISE setup. The ISE consists of an ion selective electrode and a reference electrode and they are connected by a milli-voltmeter. Measurement is accomplished simply by immersing the two electrodes in the same test solution, the selective membrane (glass membrane) on the side of the ion selective electrode allows measured ions (hydrogen ion) to pass, but excludes the passage of the other ions. Therefore, there is a potential difference between the membrane which is defined by Nernst equation (Eq. (4.1)).

$$E = E^0 + \frac{RT}{F}\ln a_{H^+} \tag{4.1}$$

where $E^0$ is the standard electrode potential, R is gas constant (8.314 J/K.mol), T is temperature (K), F is Faraday constant (96,500 coulombs/mol). On the side of reference electrode, the selective membrane is replaced by porous frit and with correct selection of electrolyte used in the reference electrode and good flow through the diaphragm the potential difference between the two liquids can be ignored. Therefore, the milli-voltmeter reflects the potential difference between the membrane thus determines the pH of the test solution.

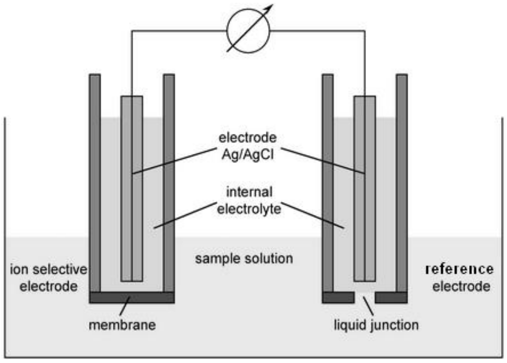

Figure 4.1 ISE (Ion Selective Electrodes)

The other type of pH electrode is ISFET (Ion Sensitive Field-Effect Transistor). Figure 4.2 shows (a) schematic diagram of a MOSFET (metal–oxide–semiconductor field-effect transistor); and (b) schematic diagram of an ISFET; For MOSFET there are gate, source and drain. For ISFET, there are also source and drain and a reference electrode is used as gate. The reference electrode is immersed in the solution of which the pH to be measured. Schematic electrical diagram for both MOSFET and ISFET is shown in Figure

4.2(c). For both devices Eq. (4.2) is valid for the non-saturated region, which shows how the source-drain current is related to applied voltage.

$$\mathrm{I_d} = \beta\left(\mathrm{V_{gs}} - \mathrm{V_T} - \frac{1}{2}\mathrm{V_{ds}}\right) * \mathrm{V_{ds}} \tag{4.2}$$

where β is constant which is determined by the mobility of the electrons, the gate insulator capacitance per unit area and the width to length ratio of the channel W/L, $V_{gs}$ is the voltage applied between the gate and the source. $V_{ds}$ is the voltage applied between the drain and source. Those variables are fixed. Therefore, source-drain current only depends on $V_T$. $V_T$ is determined by the surface potential which results from a chemical reaction between the analyte and the electroactive material that is deposited on the surface of the ISFET. The chemical reaction is related to the pH of the analyte. A very good electroactive material is $Ta_2O_5$, it allows very high sensitivity of the ISFET(Bergveld, 2003).

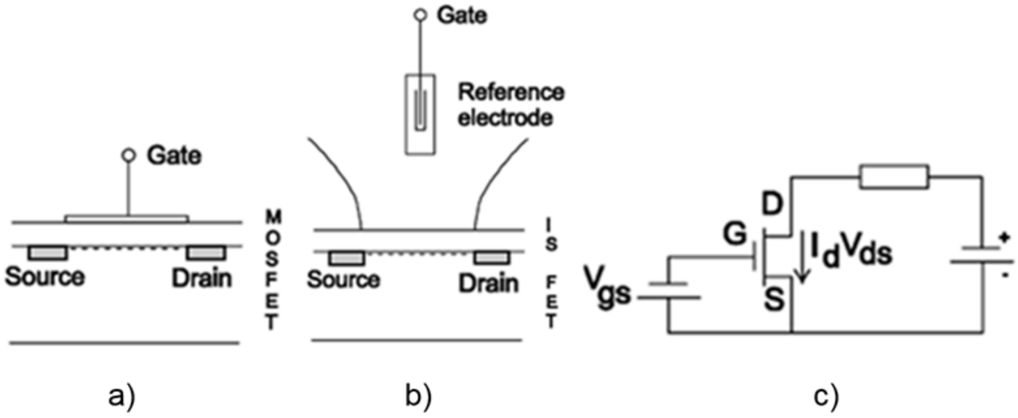

Figure 4.2 MOSFET and ISFET a) Schematic Diagram of a MOSFET b) Schematic Diagram of an ISFET c) Schematic Electrical Diagram for both MOSFET and ISFET(Bergveld, 2003)

Either for ISE or ISFET, reference electrode is required. The most common reference electrode is silver chloride electrode, which is made of silver wire coated with solid silver chloride, immersed in concentrated potassium chloride solution (filling solution) saturated with silver chloride. The potential of the silver chloride electrode is also determined by Nernst Equation (Eq. (4.3)).

$$E = E^0_{AgCl} + \frac{RT}{F} \ln a_{H^+} \tag{4.3}$$

where $E^0_{AgCl}$is the standard electrode potential, R is gas constant (8.314 J/K.mol). T is temperature (K), F is Faraday constant (96,500 coulombs/mol). Based on the equation, the reference potential changes with temperature and the chloride ion concentration, also silver is quite sensitive to visible light. Therefore, frequent calibration for pH electrodes is required, which brings great inconvenience for the field measurement in hot spring systems. Another disadvantage is the biofouling of the electrodes. Glass is used as ion selective membrane and outer capsulation for the electrodes. However, biofouling on glass is very strong, which causes the measurement error of the electrode for long-term data colleting in aqueous environment.

## 4.2 Graphene and Anti-biofouling

Graphene has one-atom thick layer of carbon arranged in a honeycomb lattice. All carbon atoms are all sp2 hybridized, one 2s orbital together with the 2px and the 2py orbitals generate three sp2 orbitals. All sp2 orbitals form σ-bonds with the sp2 orbitals of the neighboring carbon atoms as shown in Figure 4.3(a). One electron left in the 2pz orbital for each carbon atom forms the π-bonding. The 2pz orbital stick out of the plane of the chain and form the π-bonds with neighboring 2pz orbitals as shown in Figure 4.3(b). The mainly graphene synthesis methods include mechanical cleaving (exfoliation), chemical exfoliation, chemical synthesis, and thermal chemical vapor deposition (CVD)(Bhuyan, Uddin, Islam, Bipasha, & Hossain, 2016). Single layer graphene with large area and high quality can be deposited using CVD. Figure 4.4 shows the process of graphene growth on copper by CVD. The copper foil with native oxide is exposed to CH4/H2 atmosphere at 1000°C, which leads to nucleation of graphene islands and formation of large area of graphene(Mattevi, Kim, & Chhowalla, 2011). With transfer technology, graphene can be transferred to many other types of substrate, which includes SiO2, SiN, glass, PET, quartz.

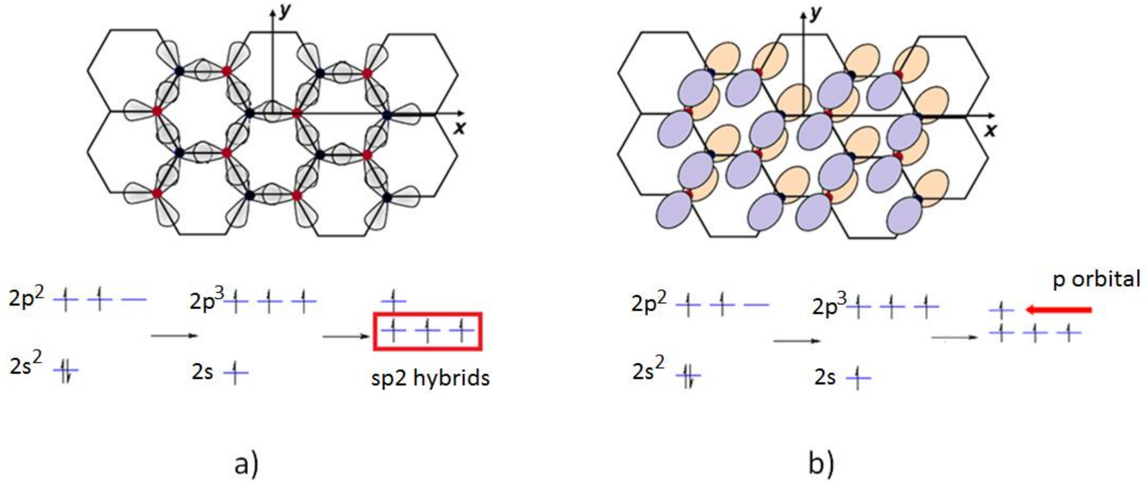

Figure 4.3 Orbitals of Graphene a) $sp^2$ Hybrids of Graphene b)π-bonding of Graphene

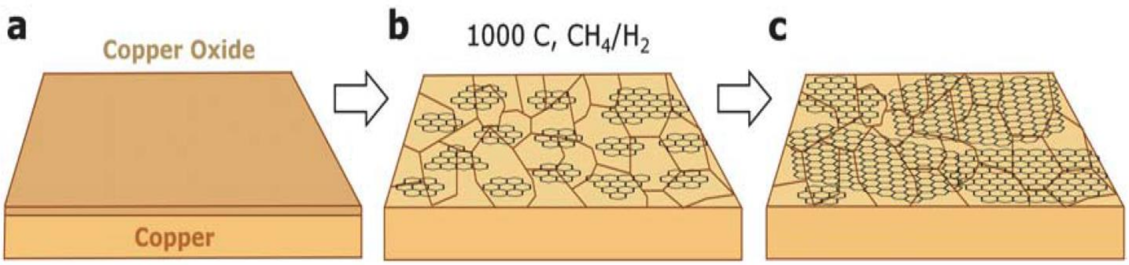

Figure 4.4 Steps of Graphene Growth on Copper a) Copper Foil with Native Oxide b) Exposure of Copper to CH4/H2 at 1000°C c) Formation of Large Area of Graphene(Mattevi et al., 2011)

Biofouling is a major hurdle to long-term sensor measurement in natural aqueous environment, not only for pH sensing but also for most of other types of sensing. Biofouling is the accumulation of organisms on underwater surfaces. Biofouling can cause device corrosion and loss of sensitivity and measurement drift. Current anti-biofouling techniques include physical (heat treatment, pulse-power technology, radioactive coatings and etc.) and chemical method (biocide, bactericide coatings and etc.). Most physical anti-biofouling methods require complicated setup and chemical methods usually cause negative environmental impact. For long-term pH sensing, anti-biofouling is much more changing since either physical or chemical methods will likely change the pH values of the natural aqueous environment.

A great advantage to fabrication of pH sensor using graphene is that graphene layer can greatly reduce adhesion of bacteria and is biofilm resistance. The anti-biofouling effect of laser-induced graphene and CVD graphene have been reported by researchers(Parra et al., 2015; Singh et al., 2017). Figure 4.5 shows epifluorescence microscopy images of a partially and completely CVD graphene-coated SiO2 samples. Bacterial bodies were green stained as indicative of live bacteria on sample surface. The study revealed that graphene coatings modify material surface energy and electrostatic interaction between material and bacteria and therefore successfully reduce the adhesion of bacteria on the surface. Microorganisms will be attracted or repelled when approach to a surface, depending on the interaction forces(Gottenbos, Busscher, Van Der Mei, & Nieuwenhuis, 2002). Figure 4.6 gives theoretical calculations of electrostatic force as function of distance between bacteria and surface (SiO2 and graphene-coated SiO2) which confirm that repulsive interaction increases when material is coated with graphene(Parra et al., 2015). The suspension media is 2% and 0.5% NaCl. The results shows the electrostatic force is repulsive and short range (<5 nm for 0.5% NaCl and <3nm for 2% NaCl).

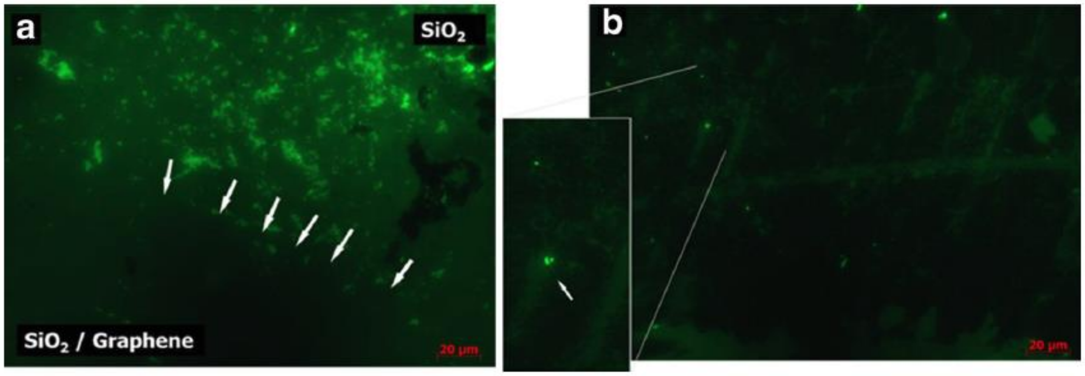

Figure 4.5 Epifluorescence Microscopy Images of Bacterial Distribution on CVD Graphene-coated Surfaces a) Partially Graphene-Coated SiO2 Surface b) Completely Graphene-coated SiO2 Surface (Parra et al., 2015)

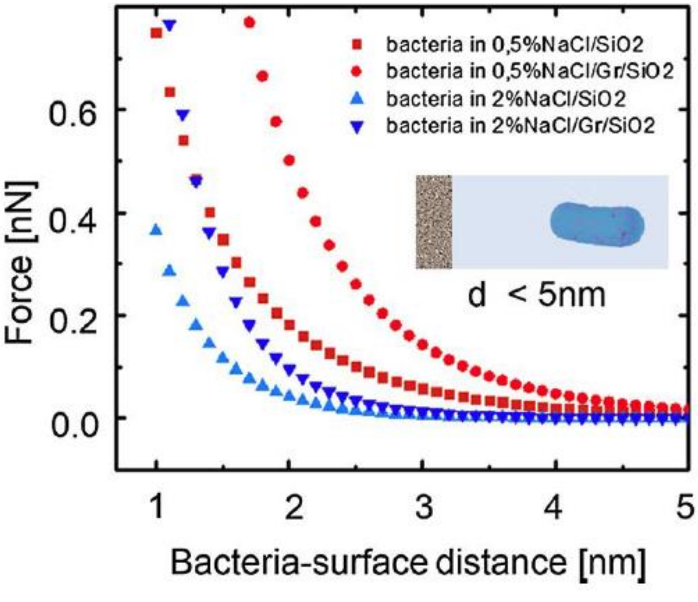

Figure 4.6 Theoretical Calculations of Electrostatic Force as Function of Distance between Bacteria and Surface (SiO2 and Graphene-coated SiO2)(Parra et al., 2015)

Even short-range hydrophobic interaction will occur when bacteria-surface distance is smaller than 1.5 nm, which have a strong impact on bacterial surface adhesion(Busscher & Weerkamp, 1987). Contact angle was measured on SiO2 and graphene-coated SiO2 (Figure 4.7) to determine the hydrophobic characteristics of graphene coatings over bacterial adhesion. Contact angles are related to the surface free energies. Hydrophobic coatings create a larger contact angle between the bacteria's glue and the surface and are used to minimize the adhesion. The measurement results show a transition from hydrophilic surface (contact angle of ~85° ± 0.7) for $SiO_2$ substrate to hydrophobic surface (contact angle of~95° ± 0.3) for graphene-coated $SiO_2$ is observed(Parra et al., 2015).

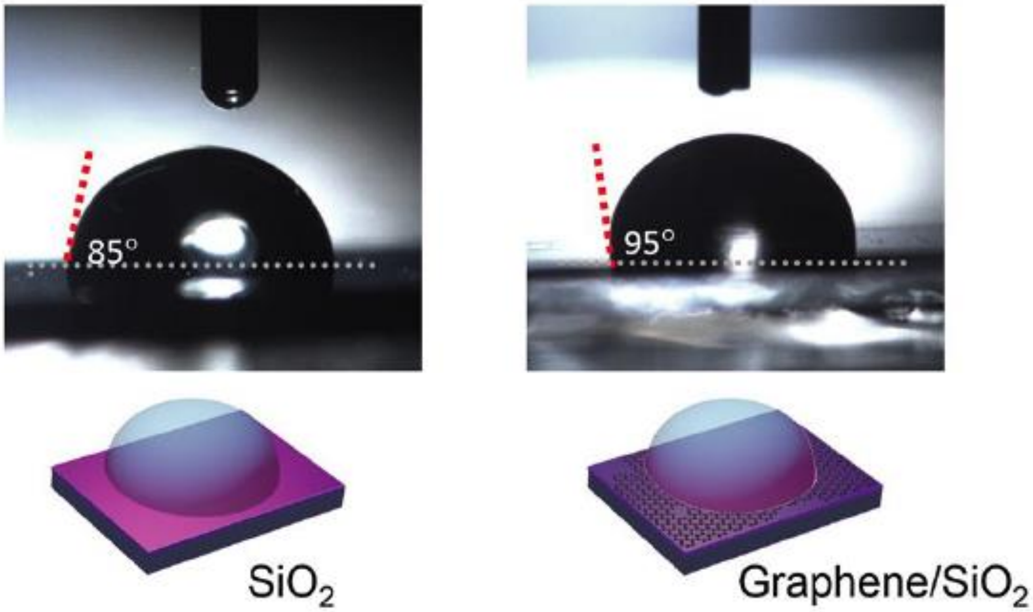

Figure 4.7 Images of Contact Angle Measurements Using Water in Contact with $SiO_2$ and graphene-coated $SiO_2$(Parra et al., 2015)

Field test for anti-biofouling of graphene was done in Desert Breeze Lake in Chandler, Arizona. As discussed in Chapter 4.1, silver chloride electrode is the most common type of reference electrode for ISE and ISFET, glass usually works as ion-selective membrane and the outer capsulation for the silver chloride electrode. Therefore, glass was used in the control group for the field test for anti-biofouling of graphene. Figure 4.8 shows the graphene on SiN and the glass slide used for the test. The graphene on SiN and glass were fixed inside a steel container and then immersed in the Desert Breeze Lake as shown in Figure 4.9. After couple of weeks, samples were taken out from the lake. As shown in Figure 4.10, green biofilm was found on the glass slide whereas the graphene sample was still smooth and shining without any adhesion of organism. Also, the graphene sample was observed under microscope and no biofilm was found. This shows graphene layer greatly prevented the microbial fouling, which is critical for long time pH sensing in the aqueous environment.

Figure 4.8 Graphene on SiN and Glass used for Anti-biofouling Test.

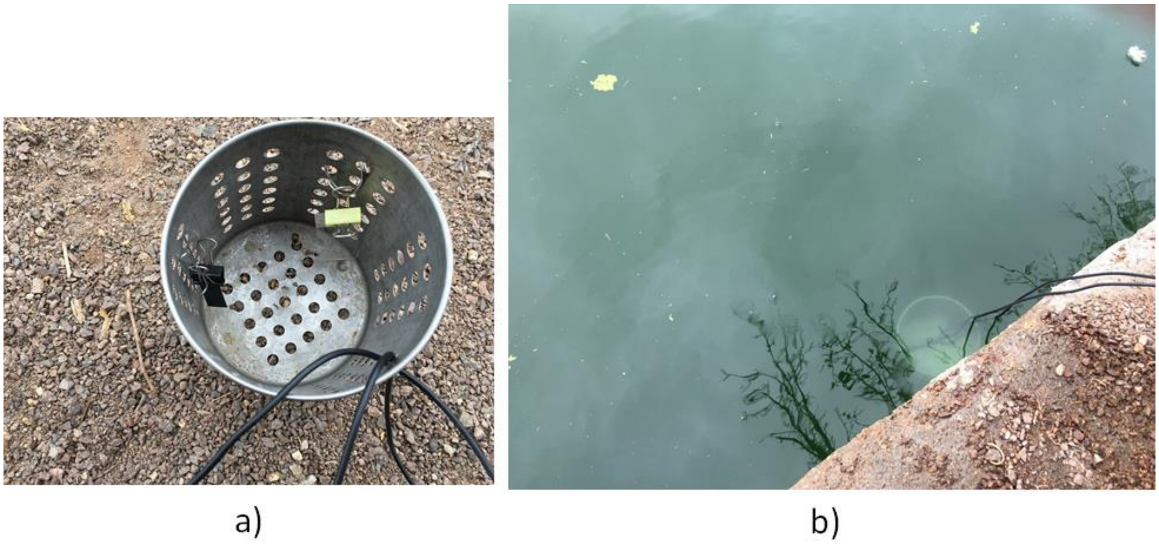
a)
b)

Figure 4.9 Setup for the Anti-biofouling Filed Test a) Graphene on SiN and the Glass Slide were Fixed inside the Steel Container b) the Container with the Samples were Immersed into the Desert Breeze Park

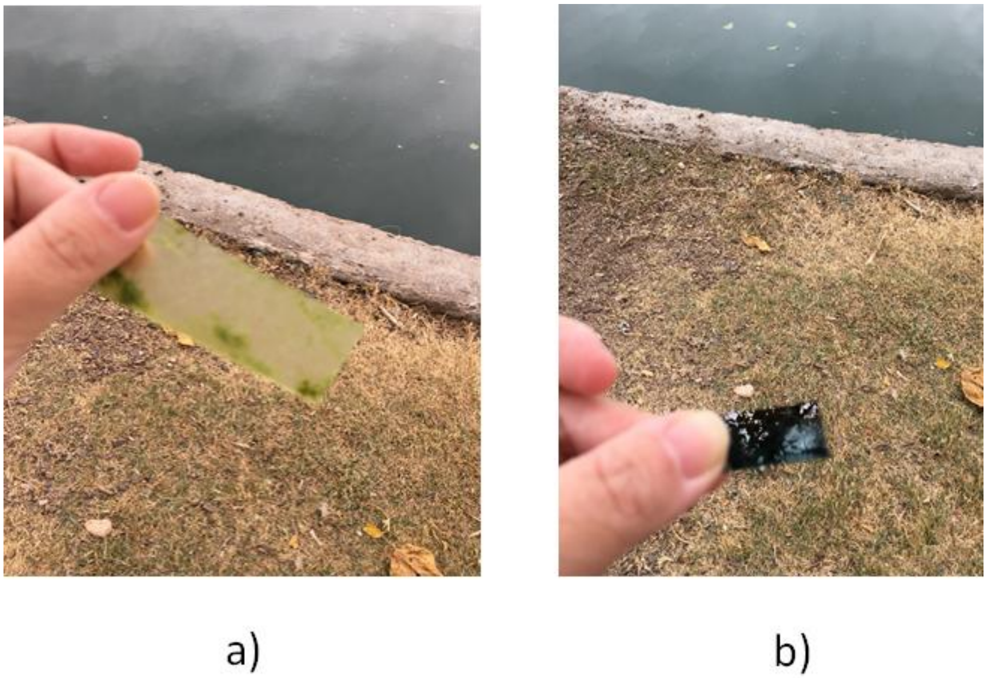
a)
b)

Figure 4.10 Glass and Graphene on SiN Taken out from the Lake after Weeks a) Biofilm was Found on the Glass Slide b) No Biofilm was Found on Graphene on SiN

## 4.3 Working Principles of Graphene pH Sensors

The band structure of graphene is shown in Figure 4.11. Valance band and conduction band of graphene touch at the Dirac points. Therefore, intrinsic graphene is a semi-metal or zero-gap semiconductor(Warner, Schaffel, Rummeli, & Bachmatiuk, 2012). Similar to semiconductor silicon, graphene can also be used to construct Field-Effect Transistor, which is named as Graphene Field-Effect Transistor (GFET). The advantages of graphene pH sensors include: they are chemically and thermally stable; the 2-D structure of graphene allows small dimension sensors; they can be integrated with other types of MEMS sensors; they are promising candidate for calibration free pH sensors.

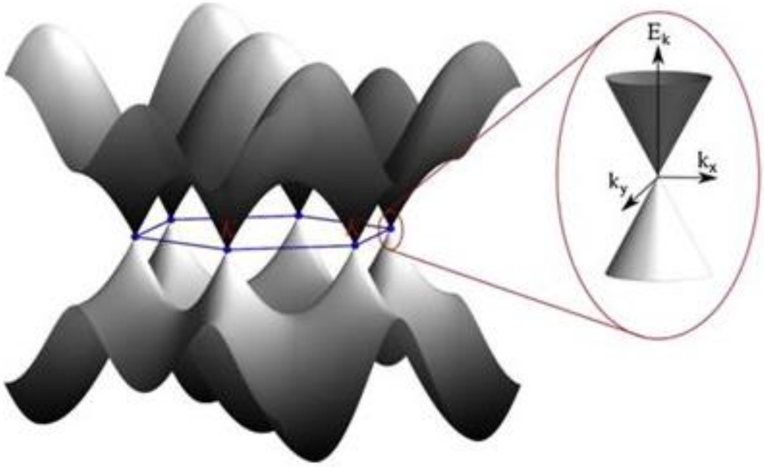

Figure 4.11 Band Structure of Graphene(Warner et al., 2012)

Figure 4.12(a) shows the conventional Metal-Oxide-Semiconductor Field-Effect Transistor (MOSFET). When no gate voltage is applied, no channel forms so there is no current between the source and drain. When a very positive gate voltage is applied , all the holes are driven away from the channel and electrons accumulate near the surface region and channel forms. So if there is voltage applied between the source and drain, current forms. For GFET, shown in Figure 4.12(b) there are also source and drain. The graphene single layer itself performs as the conductive channel. The oxide and the gate are on the backside. The conducting property of the graphene single layer is related to gate voltage.

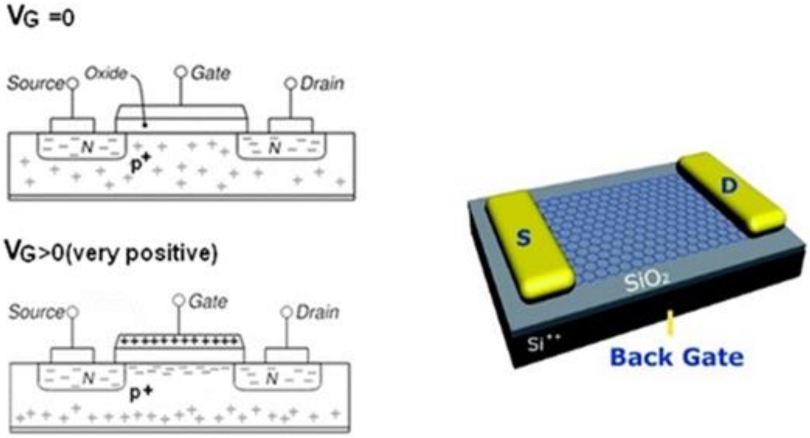

a) b)

Figure 4.12 a) Metal-Oxide-Semiconductor Field-Effect Transistor b) Graphene Field-Effect Transistor(Guo et al., 2010)

Figure 4.13 shows ambipolar electric field effect in single layer graphene. The resistance of the graphene layer changes as a function of the electric field applied. Positive gate voltage $V_g$ induces electrons in concentrations. Negative $V_g$ induces holes in concentrations. When gate voltage equals zero, the resistance changes little with $V_g$, indicating the substitution of one type of carrier with another. The sharp peak is the Dirac point. Figure 4.14 shows the working mechanism of GFET pH sensor. When the graphene single layer is immersed in the acid solution, the hydrogen ions attached to the inner Helmholtz plane, which makes graphene ‘electron’ doped, in other word, it induces the electrons in concentrations in the same way the positive gate voltage does. When the graphene single layer is immersed in an alkali solution, the hydroxide ions attached to the inner Helmholtz plane, which makes graphene 'hole' doped, in other word, it induces the holes in concentrations in the same way the negative gate voltage does. Figure 4.15(a) shows how the conductance of graphene changes with the gate voltage in neutral solution and in acid and base solution. When the graphene is in acid or base solution, the Dirac point is not where gate voltage equals zero. Therefore, either by applying a proper negative gate voltage or a proper positive voltage, GFET works as a pH sensor by reflecting the change of conductance when it is in solution with different pH. Also, GFET can work as pH sensor by doping the graphene if gate voltage is not applied. As shown in Figure 4.15(b) and (c), n-doping makes the curves shift to the left, p-doping to the right. In fact, graphene is naturally p doped when it is exposed in the air and water.

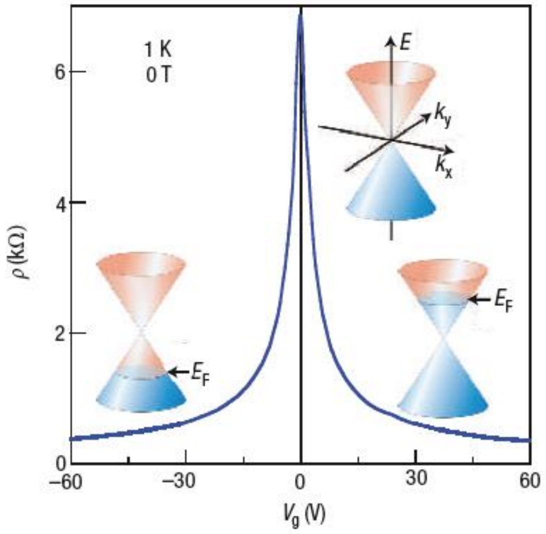

Figure 4.13 Ambipolar Electric Field Effect in Single-layer Graphene(Geim & Novoselov, 2007)

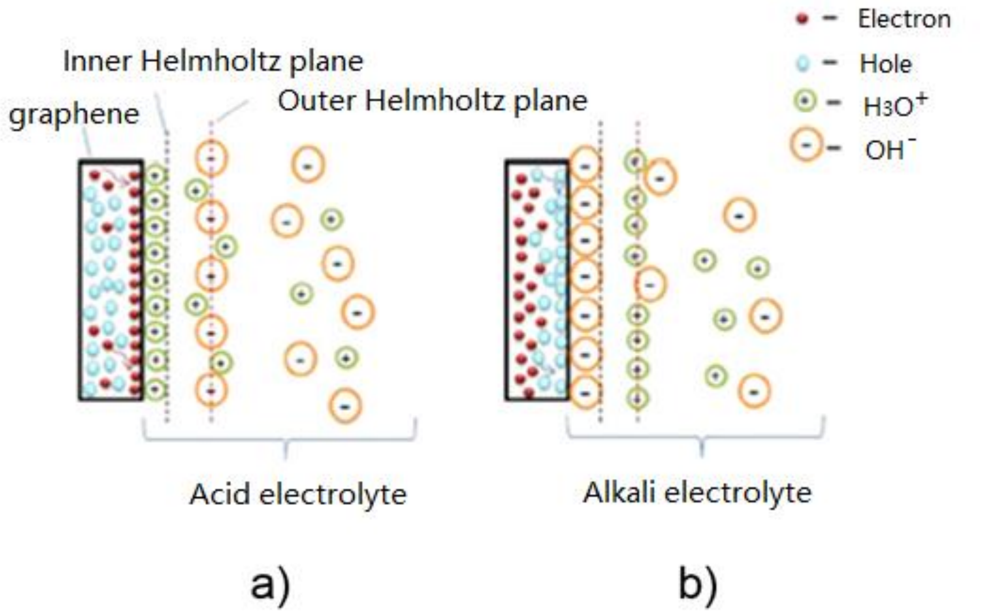

Figure 4.14 Graphene Single Layer in a) Acid Electrolyte b) Alkali Electrolyte(Lei, Li, Xue, & Xu, 2011)

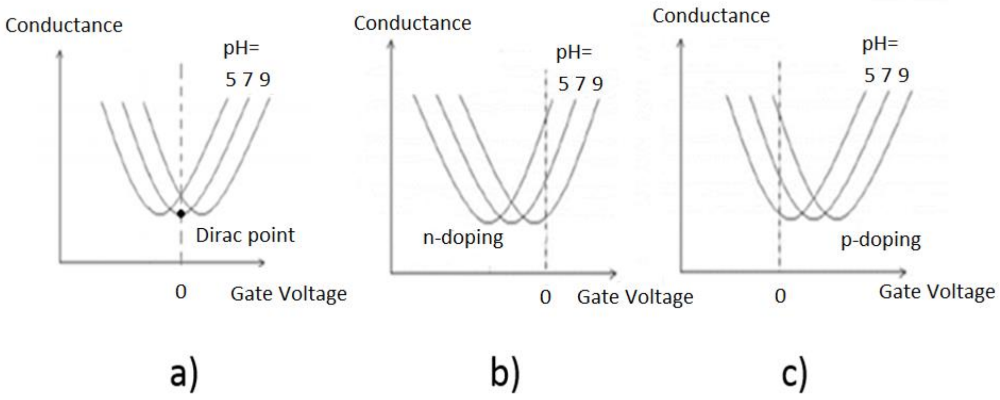

Figure 4.15 Conductance of Graphene Changes with the Gate Voltage in Neutral Solution and in Acid and Base Solution for a) Intrinsic Graphene b) n Doped graphene c) p Doped Graphene

One important question is, why only $OH^-$ and $H_3O^+$ adsorb at the graphene/electrolyte interface and are detected by the sensor? Why do other types of ions stay far away and do not disturb $OH^-$ and $H_3O^+$ ions to be detected? This is much about the selectivity of the sensor, which is essential to sensors fabrication and application. Molecular dynamic simulation of the ion adsorption and segregation at the graphene/electrolyte interface was done by researchers. The computation results of the density profiles of ions at the graphene surface are shown in Figure 4.16 (Cole, Ang, & Loh, 2011). $H_3O^+$ adsorbs closer to the surface and at higher concentration than $Cl^-$ at low pH. Also, at high pH, $OH^-$ ions are closer to the graphene surface over small, positively charged ions.

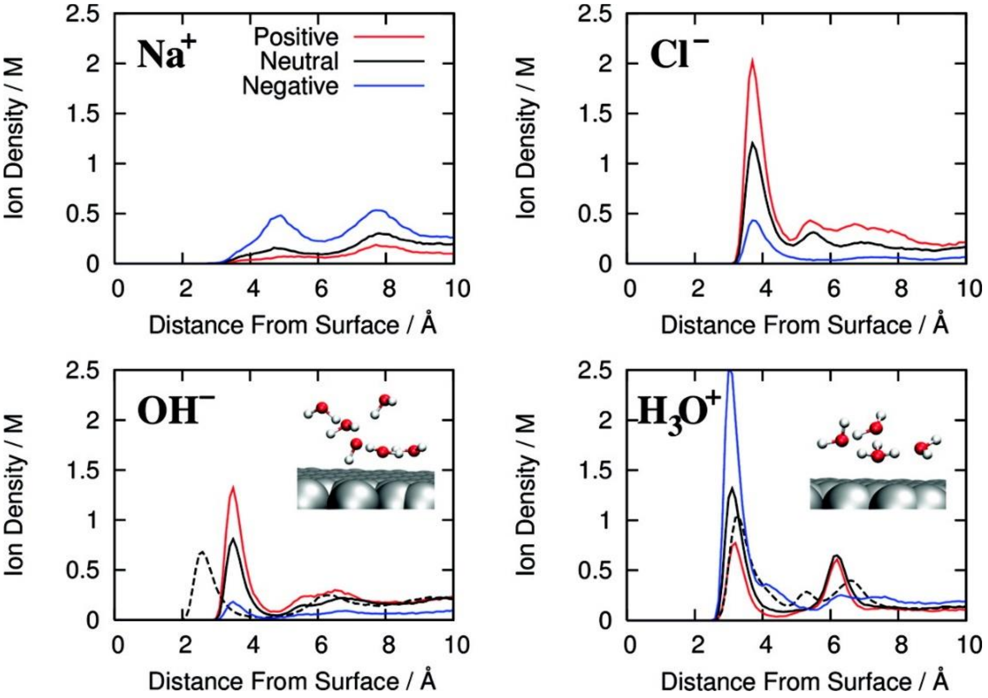

Figure 4.16 Ion Adsorption and Segregation at the Graphene/Electrolyte Interface(Cole et al., 2011)

Also, experiment methods are used to show the dominant $OH^-$ and $H_3O^+$ adsorption at the graphene/electrolyte interface(Ang, Chen, Wee, & Loh, 2008). One typical method is cyclic voltammetry (CV). Clear maxima in the cathodic and anodic peak currents can be observed as shown in Figure 4.17. The positions of the peaks are dependent on the pH value of the solution and they agree with the electrochemical potential for the redox couples, $H_2/H_3O^+$ and $O_2/OH^-$, in which both $OH^-$ and $H_3O^+$ ions are specifically adsorbed on the graphene surface.

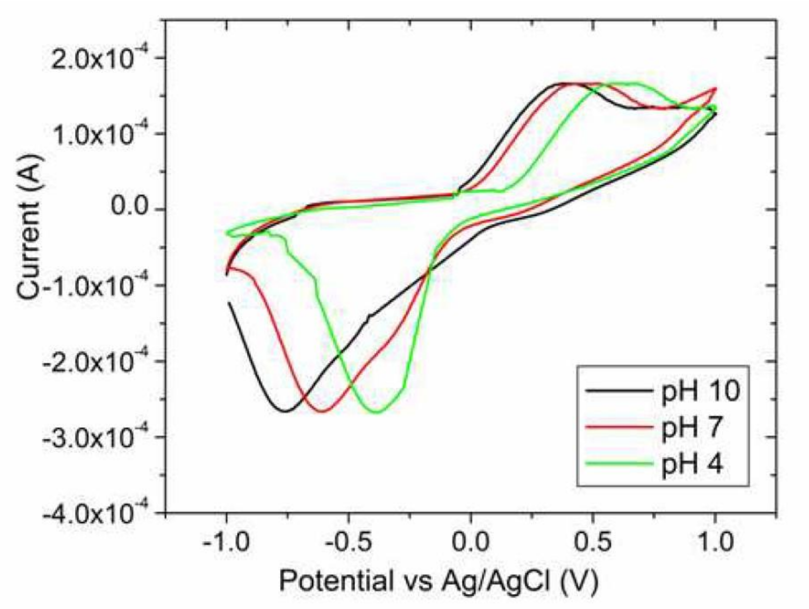

Figure 4.17 Cyclic Voltammetry (CV) of Graphene (Ang et al., 2008)

Also, frequency-dependent impedance spectroscopy was done to further elucidate this question(Ang et al., 2008). Figure 4.18 shows that under different potential frequency capacitance peaks were observed at similar anodic and cathodic peak potentials when the pH equals 7. But under different pH values, the peaks shift. Also, measurements were done at different buffer concentrations (Ang et al., 2008). The positions of these peaks are insensitive to changes in buffer concentrations as shown in Figure 4.19. These indicate that the adsorption of $OH^-$ and $H_3O^+$ is the dominant process that is responsible for influencing the conductivity behavior of graphene.

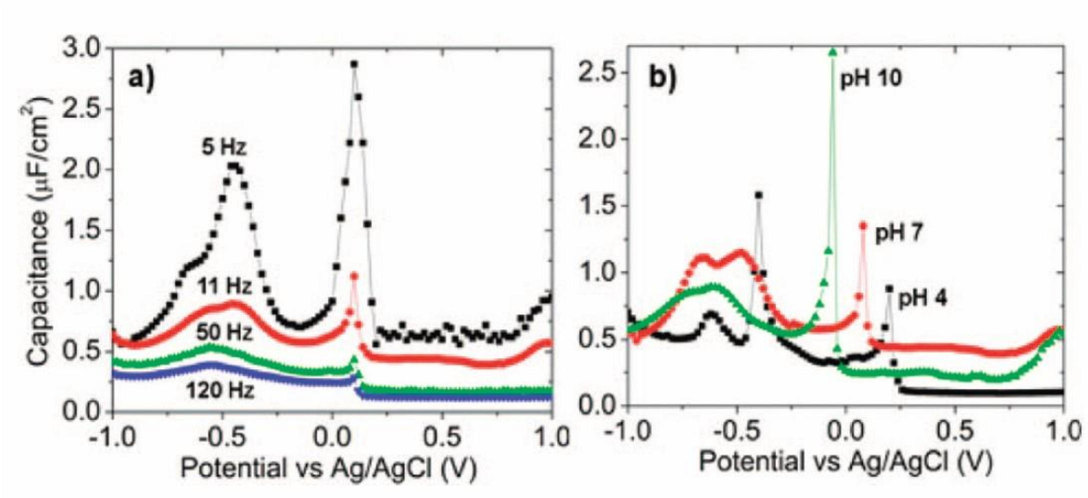

Figure 4.18 Frequency Dependent Impedance Spectroscopy of Graphene (a) Frequency Dispersion of Measured Capacitance for Adsorbed $H_3O^+$ at -0.5 V and $OH^-$ at -0.2 V Collected in 10 mM KCl/10mM PBS Solution at pH 7 (b) pH Dependence of Interfacial Capacitance Peak Potential(Ang et al., 2008)

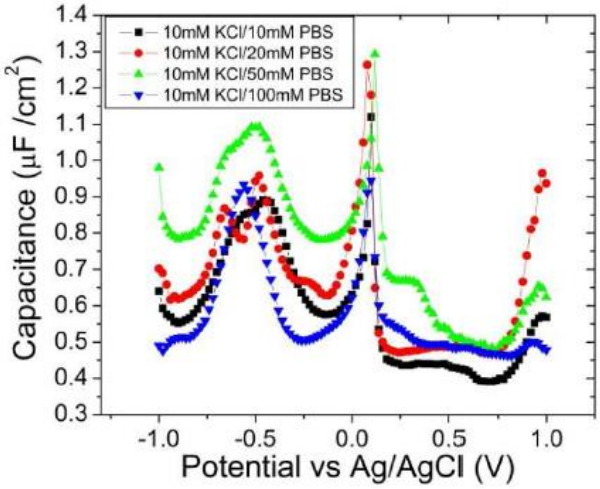

Figure 4.19 Interfacial Capacitance Plots of Graphene Derived from Impedance Measurements Collected at Different Buffer Concentrations (Ang et al., 2008)

### 4.4 Computation of Graphene Carrier Density

Conductivity of graphene is important to the performance of the device. The conductivity of graphene σ, is described by the following relation (Equation 4.4):

$$\sigma = ne\mu \tag{4.4}$$

where n is the carrier density, e is the electronic charge, μ is carrier mobility. Carrier density of graphene will be computed in the following part of this chapter. Also, mobility of graphene will be discussed.

#### 4.4.1 Carrier Density of Graphene

Dirac Equation (Equation (4.5)) is used to describe the carriers in graphene.

$$i\hbar(\partial\varphi(X,t))/\partial t = (\frac{1}{i}\alpha \cdot \nabla + \beta m)\varphi(X,t) \tag{4.5}$$

where φ(X, t) is the wave function for the electron of rest mass m with spacetime coordinates x, t; ħ is the reduced Planck constant(Planck constant divided by 2π); $\beta = (\begin{matrix} I & 0 \\ 0 & -I \end{matrix})$; $\alpha_i = (\begin{matrix} 0 & \sigma_i \\ \sigma_i & 0 \end{matrix})$; is Pauli matrices $\sigma_1 = (\begin{matrix} 0 & 1 \\ 1 & 0 \end{matrix})$, $\sigma_2 = (\begin{matrix} 0 & -i \\ i & 0 \end{matrix})$, $\sigma_3 = \begin{pmatrix} 1 & 0 \\ 0 & -1 \end{pmatrix}$. (Haldane, 1988; McClure, 1956; Novoselov et al., 2007; Slonczewski & Weiss, 1958).

The linear dispersion relation for graphene is given by Equation (4.6):

$$\mathrm{E(k)} = s\hbar v_F|k| \tag{4.6}$$

Where s=1 is for the conduction band (CB) and s=-1 is for the balance band (VB). $v_F$~106 m/s is the Fermi velocity of carriers in graphene, and$|k| = \sqrt{k_x^2 + k_y^2}$ is the wave vector of carriers in the graphene sheet. The point$|k| = 0$, referred to as the Dirac point, where E $(|k| = 0) = 0\ eV$ is set as the reference of energy.

In 2D K-space, since there is one k-state for every choice of quantum numbers $(n_x, n_y)$, the area per k state is $(2\pi)^2$/L1L2= $(2\pi)^2$/A. Therefore, taking spin and valley degeneracy into account, the number of states per area is given by Equation (4.7)

$$N_k = \frac{g_v g_s \mathrm{A}}{(2\pi)^2} \tag{4.7}$$

where the prefactors gs = 2, gv = 2. For the area shown in Figure 4.20 , there is,

$$\rho_{gr}(E)dE = N_K 2\pi k dk/A \tag{4.8}$$

where, $\rho_{gr(E)}$ is the density of states (DOS) of graphene. Also, $\mathrm{k} = \frac{E}{\hbar v_F}$, $\mathrm{dE} = \hbar v_F dk$. Therefore, the density of states of graphene is given by

$$\rho_{gr}(E) = \frac{g_v g_s}{2\pi(\hbar v_F)^2}|E| \tag{4.9}$$

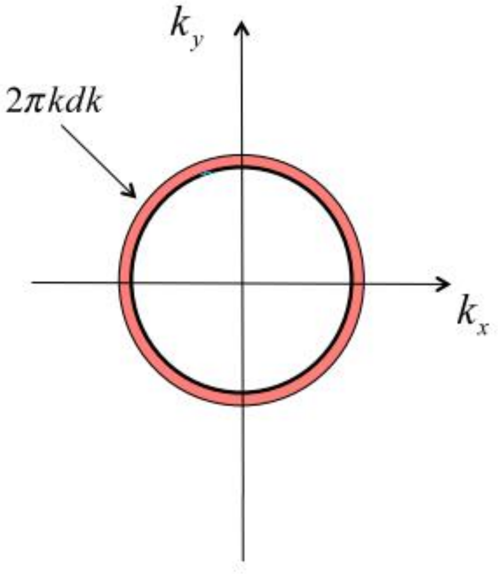

Figure 4.20 Density States within the Area of $2\pi kdk$ in K space

The Fermi-Dirac function $f_{FD}(E)$ (Equation (4.10)), gives the probability of a state being occupied by an electron.

$$f_{FD}(E) = (\exp\left(\frac{E-\mu}{k_B T}\right) + 1)^{-1} \quad (4.10)$$

where $\mu$ is the chemical potential. The chemical potential of a system of electrons is also called the Fermi level $E_F$. $k_B$ is the Boltzmann constant, T is the absolute temperature.

In thermal equilibrium the density of electrons is calculated as an integrate of the DOS and the probability distribution function as follows:

$$\mathrm{n} = \int_0^\infty f_{FD,n}(E)\,\rho_{gr}(E)dE \quad (4.11)$$

The density of conducting holes (denoted as $p$) is calculated as:

$$\mathrm{p} = \int_{-\infty}^0 f_{FD,p}(E)\,\rho_{gr}(E)dE \quad (4.12)$$

where$f_{FD,p}(E) = 1 - f_{FD,n}(E) = (\exp\left(\frac{\mu-E}{k_B T}\right) + 1)^{-1}$.

Figure 4.21 shows the density of state $\rho_{gr}(E)$ for graphene. The Fermi-Dirac function$f_{FD,n}(E)$ giving the probability of a state being occupied by an electron (at room temperature) is shown in Figure 4.22. The Fermi-Dirac function$f_{FD,p}(E)$for the holes (at room temperature) is shown in Figure 4.23.

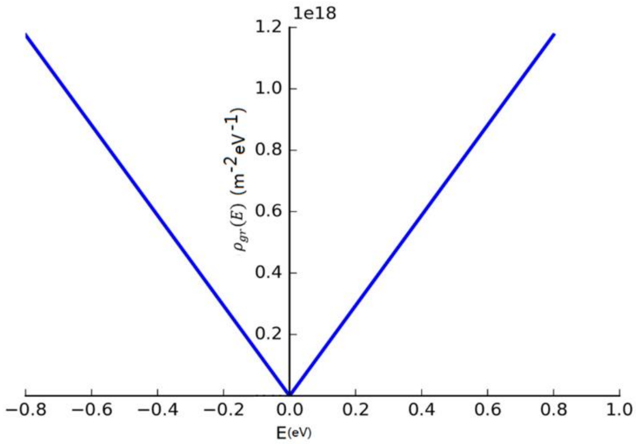

Figure 4.21 Density of State $\rho_{gr}(E)$for Graphene

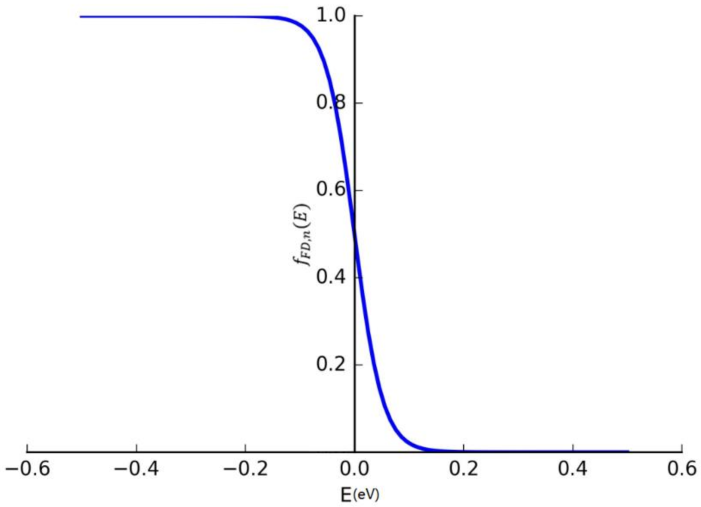

Figure 4.22 Fermi-Dirac Function$f_{FD,n}(E)$ for Electrons (at Room Temperature)

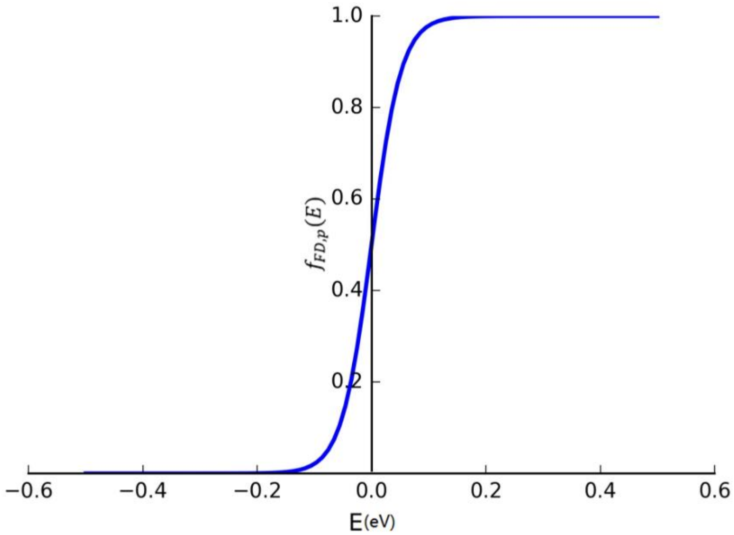

Figure 4.23 Fermi-Dirac Function $f_{FD,p}(E)$for Holes (at Room Temperature)

Figure 4.24 shows the curve for product of density of state $\rho_{gr}(E)$ and the Fermi-Dirac function$f_{FD,n}(E)$for electrons in undoped graphene. The area under the curve gives the density of electrons, 8.2 $*10^{14}m^{-2}$ for undoped graphene under room temperature.

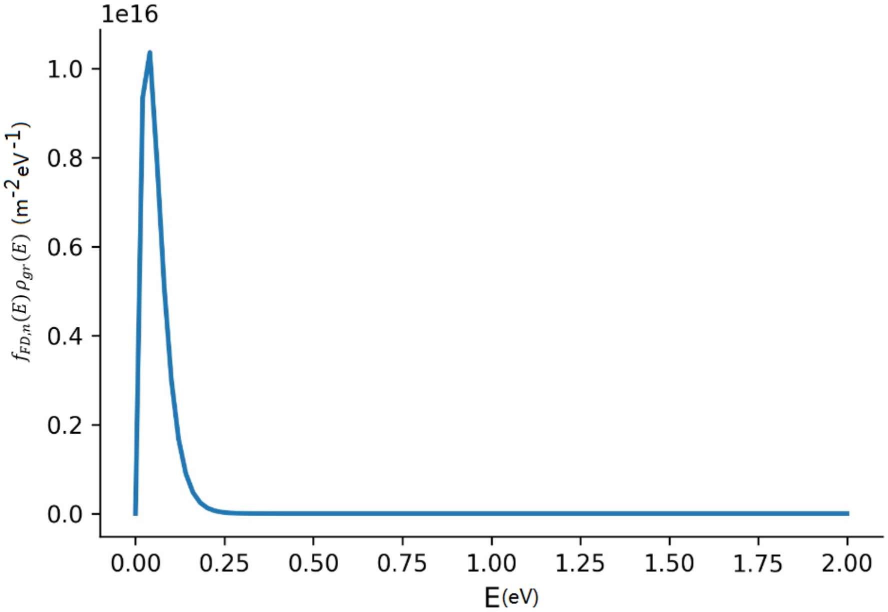

Figure 4.24 Product of Density of State $\rho_{gr}(E)$ and the Fermi-Dirac Function$f_{FD,n}(E)$ for Electrons in Undoped Graphene ($E_F$ =0). The Area under the Curve Gives the Density of Electrons, 8.2 *$10^{14}$ $m^{-2}$ for Undoped Graphene (at Room Temperature).

Similarly, Figure 4.25 shows the curve for product of density of state $\rho_{gr}(E)$ and the Fermi-Dirac function$f_{FD,p}(E)$for holes in undoped graphene. The area under the curve gives the density of holes, which is also 8.2 *$10^{14}$$m^{-2}$ for undoped graphene under room temperature.

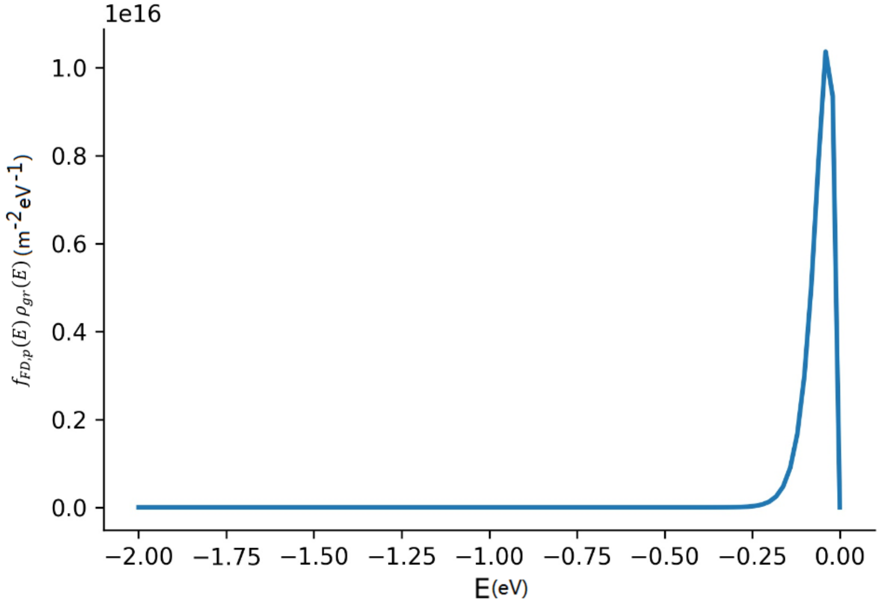

Figure 4.25 Product of Density of State $\rho_{gr}(E)$ and the Fermi-Dirac Function $f_{FD,p}(E)$ for Electrons in Undoped Graphene($E_F$ =0). The Area under the Curve Gives the Density of Holes, 8.2 *$10^{14}$m$^{-2}$ for Undoped Graphene(at Room Temperature).

Figure 4.26 shows the bands occupation and the corresponding Fermi distribution when $E_F = 0$ at finite temperatures. The valence band is fully occupied and the conduction band is empty.

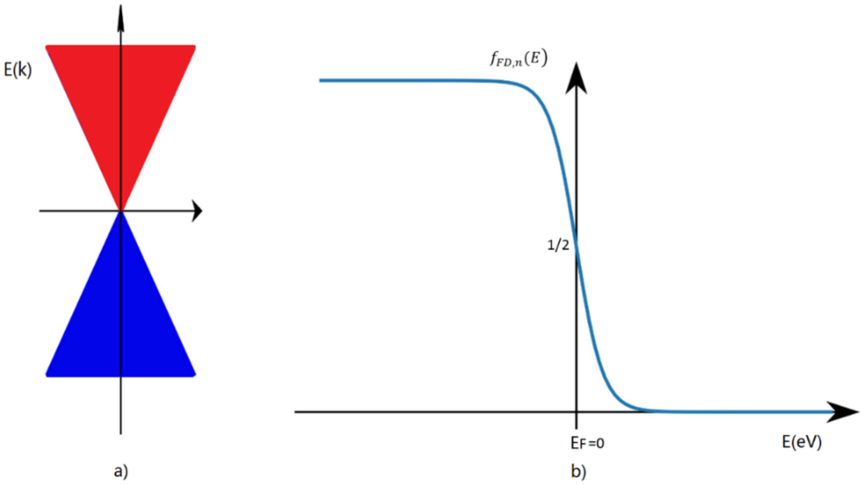

Figure 4.26 a) Bands Occupation for Undoped Graphene ($E_F$=0) b) Corresponding Fermi Distribution When $E_F$ = 0 at Finite Temperatures.

In doped graphene, the Fermi level is shifted, and the density of one type carrier dominates over the other. Figure 4.27 shows the bands occupation and the corresponding Fermi distribution when $E_F$> 0 at finite temperatures. The valence band is fully occupied, and there is a considerable number of electrons in conduction band.

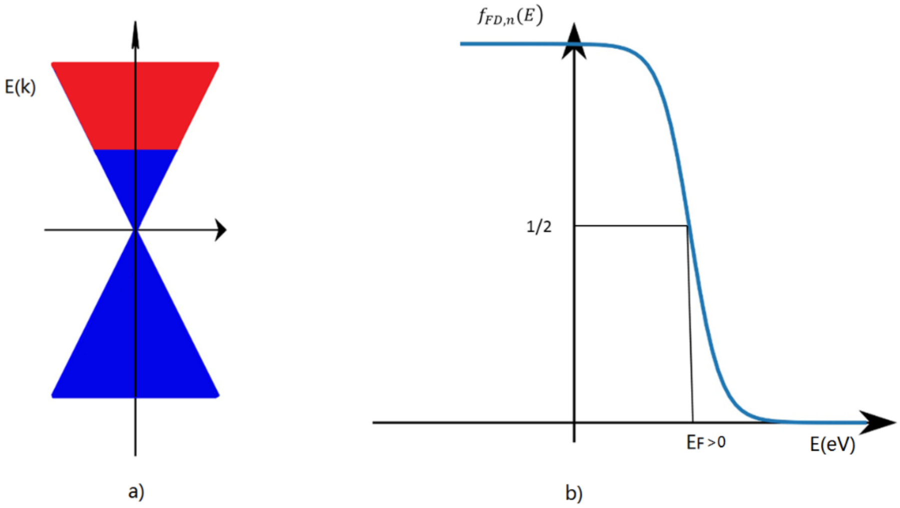

Figure 4.27 a) Bands Occupation for n Doped Graphene (EF>0) b) Corresponding Fermi Distribution when EF > 0 at Finite Temperatures.

The charge carrier (electrons and holes) concentration for different position of the Fermi level at room temperature is shown in Figure 4.28. Chemical potential values less than or equal to 0.2 eV was discussed by previous papers(G. W. Hanson, 2008; Jablan, Buljan, & Soljačić, 2009; Stauber, Peres, & Geim, 2008). These small values of the chemical potential are consistent with low-to-moderate levels of chemical doping in graphene. Highly doped graphene is considered with μ = 0.6 eV. A high doping level of graphene by immersing graphene in solutions of 14 M concentration of $H_2SO_4$ was also reported by previous research (Zhao et al.) They achieved carrier concentrations of 0.2~0.4 × $10^{13}$ $cm^{-2}$ in bilayer graphene.

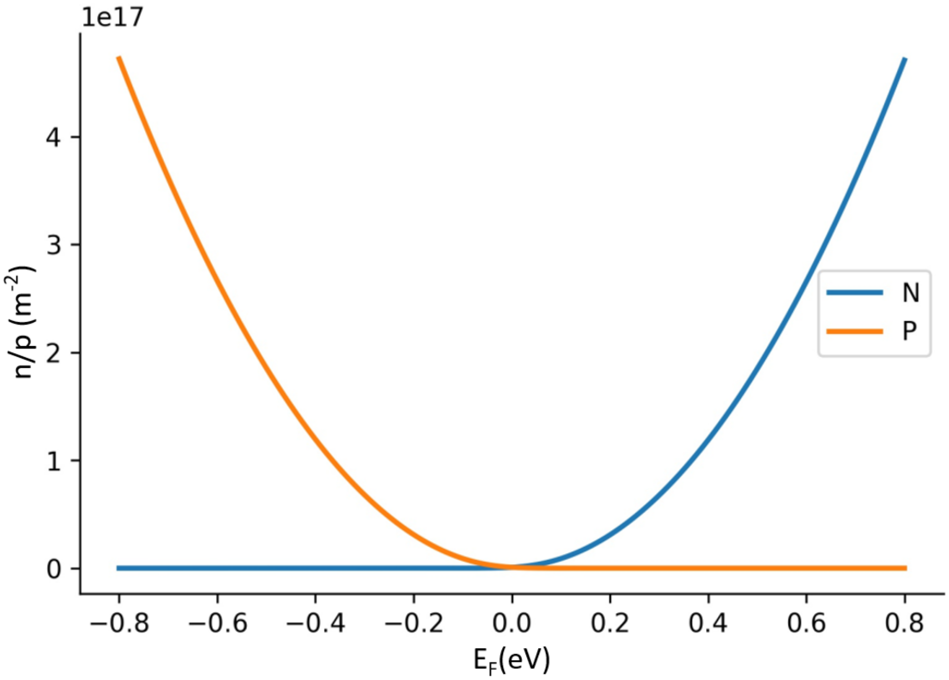

Figure 4.28 Charge Carrier (Electrons and Holes) Concentration for Different Position of the Fermi level at Room Temperature

### 4.4.2 Graphene Mobility

The mobility of graphene can be explored by experimental methods through the electric field effect. Figure 4.29 shows the graphene mobility mapping for a large area of chemical vapor deposition (CVD)graphene film (Buron et al., 2015) . Figure 4.29 a) shows the conductivity $\sigma_s$ as a function of gate voltage Vg for three distinct areas in the map with highly conducting graphene(circle, 0 V < Vg < 18 V), less conducting graphene(triangle, 26 V < Vg < 40 V), and no graphene coverage(square). The graphene film was p type. Figure 4.29 b) is the map showing the spatial distribution of hole field effect mobility.

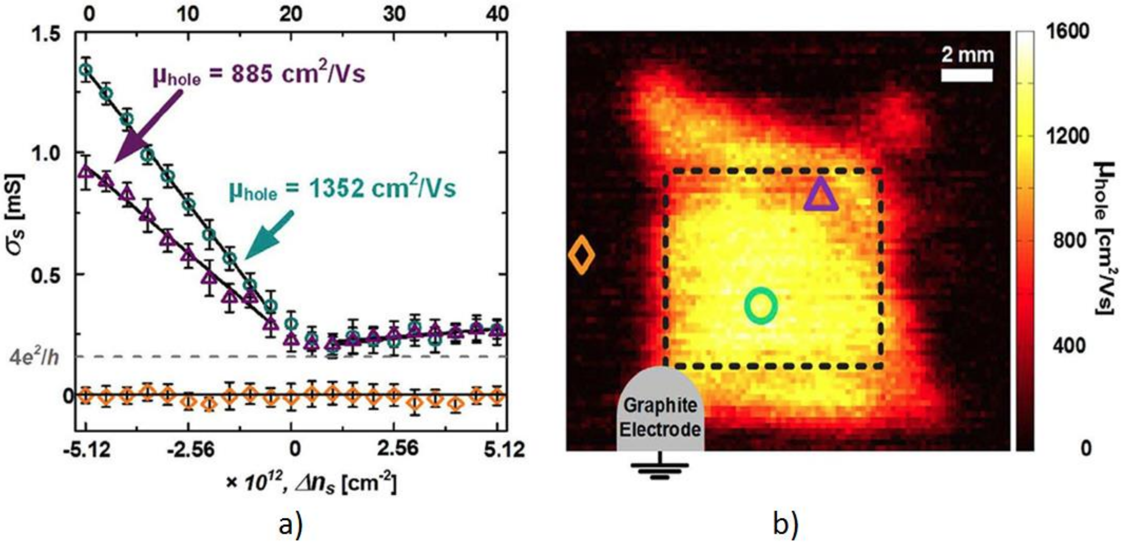

Figure 4.29 Field-Effect Mobility Mapping of Graphene. a)Conductivity $\sigma_s$ as a Function of Gate Voltage Vg. b) Spatial Distribution of Hole Field Effect Mobility(Buron et al., 2015)

Similarly, the electron field effect mobility of graphene has been explored by previous researches(Ang et al., 2008; F. Chen, Xia, & Tao, 2009; J.-H. Chen et al., 2008; Schedin et al., 2007). These results indicate both electron and hole field-effect mobility of graphene depends on the fact of doping. Therefore, variations in mobility rather than doping can be the cause of conductance in-homogeneities of graphene, which it is very difficult to assessing graphene transport properties.

Despite the zero carrier density at the Dirac point, graphene exhibits a finite minimum conductivity. Theoretical analysis proved that the finite minimum conductivity is a characteristic property of Dirac fermions in two dimensional systems. In zero temperature, at zero charge carrier density without any scattering the conductivity is predicted to be of the order of $e^2/h$ (Katsnelson, 2006).The experimental values are around $\sigma_{min} = 4e^2/h$.

## 4.5 Design and Fabrication of Graphene pH sensors

Four inch wafer size CVD (Chemical Vapor Deposition) single layer graphene on SiO2 can be purchased from ACS material company (Figure 4.30). The wafer structure is shown in Figure 4.31. The silicon substrate is heavily doped.

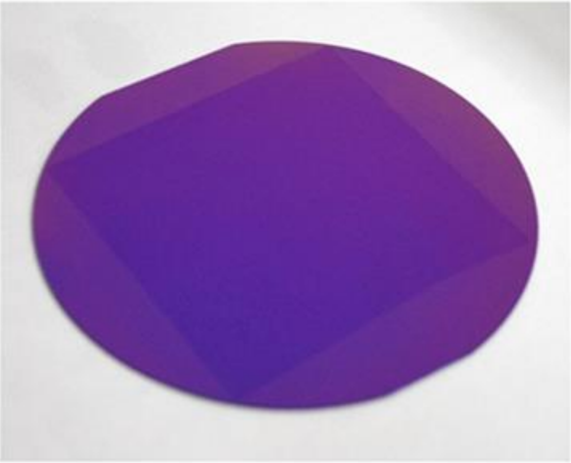

Figure 4.30 Four Inch Wafer Size CVD Single Layer Graphene Sold by ACS Material Company("Graphene on SiO2 Substrate," n.d.)

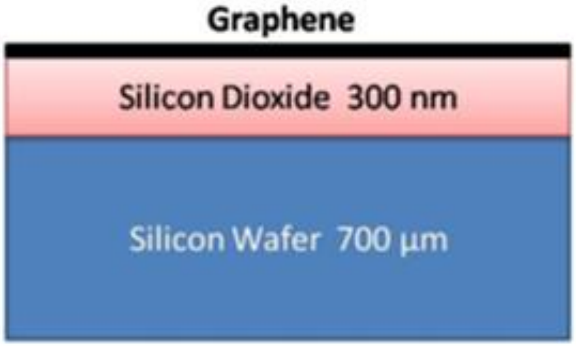

Figure 4.31 Wafer Structure for the Four Inch Wafer Size CVD Single Layer Graphene Sold by ACS Material Company(“Graphene on SiO2 Substrate,” n.d.)

Figure 4.32 shows the graphene layer under microscope. Au/Ti (100nm/10nm) was deposited to form the top metal contacts as the source and drain (Figure 4.33). The back gate was formed at the back side of the chip. Wire bonding has been done on two metal contacts and on the backside, followed by epoxy sealing.

Figure 4.32 Graphene Layer under Microscope

Figure 4.33 Graphene pH Sensor

## 4.6 Experiment Results and Discussion

Test setup is shown as Figure 4.34. DC power supply and multi-meter were used as device analyzer.

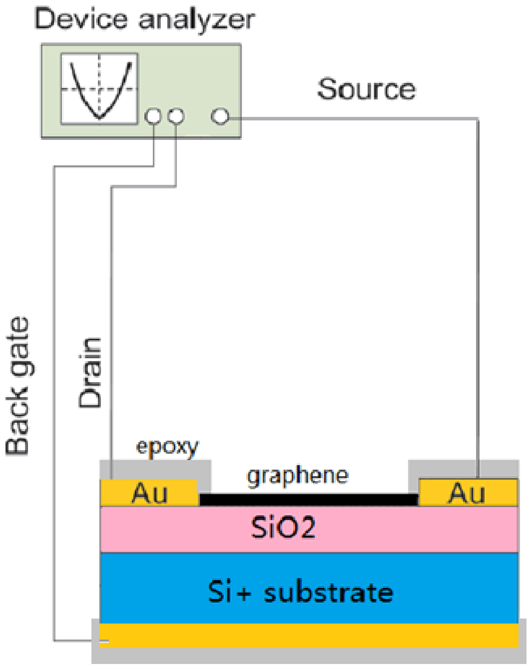

Figure 4.34 Experimental Setup for Electrical Characteristic Analysis of the GFET

The gate voltages were applied from -18V to 30V with a step of 2V and the resistance of the graphene with the gate voltage in the air at room temperature is shown in

Figure 4.35. Clearly, the Dirac Point is where the gate voltage is positive (around 8 V) which shows that the graphene single was p doped in the air. The test result is quite consistent with the theoretical ambipolar electric field effect in single-layer graphene.

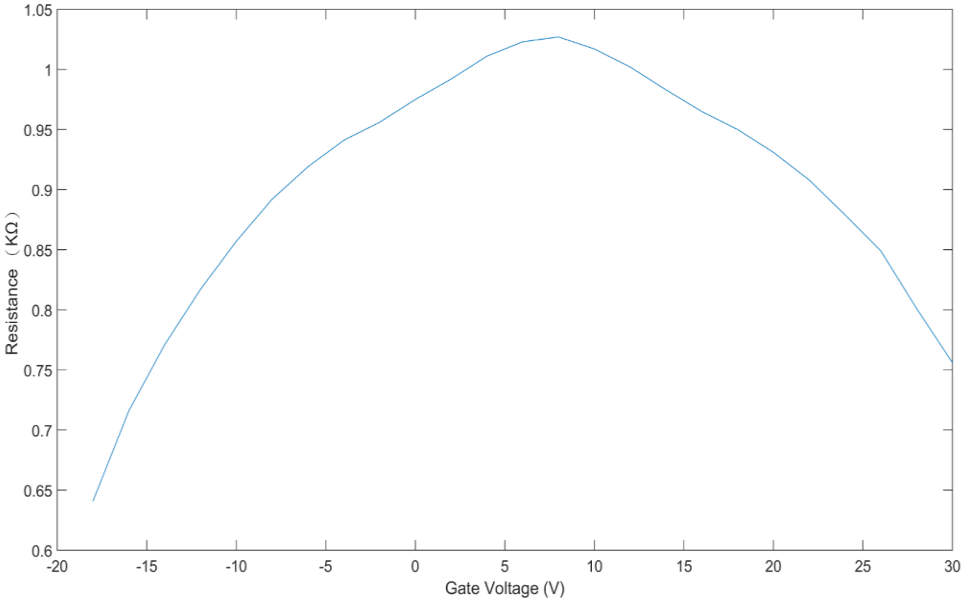

Figure 4.35 Test Result for the Ambipolar Electric Field Effect in Single-layer Graphene

The resistance of Sample 1 was measured the in buffered solutions of different pH values (3-11) without back gate voltage applied. The pH buffered solutions were purchased from Atlas Scientific. The results (Table 4.2) shows in the alkaline solutions the resistance of the sensor decreases with the pH values from 7 to 11. However, in the acid solutions the resistance does not change monotonically with the pH values from 3 to 7. Therefore, Sample 1 cannot be used as a pH sensor. The reason why the resistance of graphene did not change monotonically with all the pH values from 3 to 11 is that, graphene single layer was p doped and hydroxide ions in the alkaline solutions enhance p doping of the graphene and therefore the resistance decreases with pH values in alkaline solutions. However, the graphene layer was not p doped to a very high level so when it is immersed in the acid solution, the hydrogen ions weaken the p doping of graphene and make the graphene under the state of n-p plateau region near the Diract point, where the resistance does not change monotonically with the pH values. Therefore, the graphene needs to be heavily p doped so that it does not work under the n-p plateau area either in acid solution or in alkaline solution.

Table 4.2 Resistance Measurement of Sample 1 in pH Buffers from pH 3 to 11

| pH | 3 | 4 | 5 | 6 | 7 | 8 | 9 | 10 | 11 |
|---|---|---|---|---|---|---|---|---|---|
| Resistance(Ω) | 1038 | 1034 | 1023 | 1028 | 1036 | 1034 | 1033 | 1029 | 1025 |

Sample 1 was soaked in DI water overnight and therefore was more heavily p doped. Then the resistance of Sample 1 was measured again in the buffered solutions of different pH values (pH3-11) without back gate voltage applied. The results (average of multiple measurements) are shown in Table 4.3. Measurement results with error bars are plotted in Figure 4.36. The results show that the resistance of the graphene sensor decreases with the increase of pH values.

Table 4.3 Average Resistance of Sample 1 (DI Water Soaked) in pH Buffers from pH 3 to 11

| pH | 3 | 4 | 5 | 6 | 7 | 8 | 9 | 10 | 11 |
|---|---|---|---|---|---|---|---|---|---|
| Resistance(Ω) | 358.8 | 354.6 | 352.4 | 351 | 349.3 | 347 | 345 | 342 | 338 |

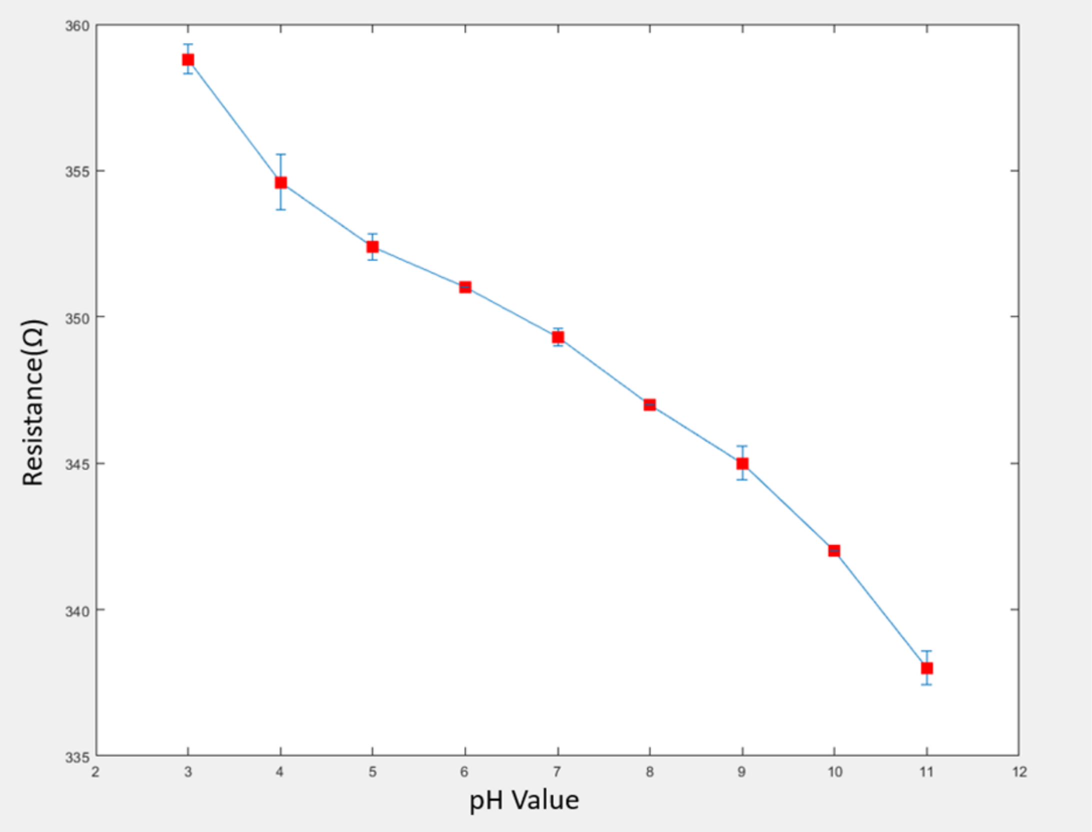

Figure 4.36 Plot for Resistance of Sample 1 (DI Water Soaked) in pH Buffers from pH 3 to 11

Then Sample 1 was baked to make it less heavily p doped and measured the in buffered solutions of different pH values (pH3-11) again, the test result is shown in Table 4.4. It confirmed the conclusion that the resistance of graphene does not change monotonically with all the pH values from 3 to 11 if the graphene is not p doped to high level.

Table 4.4 Resistance Measurement of Sample 1 (Baked) in pH Buffers from pH 3 to 11

| pH | 3 | 4 | 5 | 6 | 7 | 8 | 9 | 10 | 11 |
|---|---|---|---|---|---|---|---|---|---|
| Resistance(Ω) | 1037 | 1040 | 1034 | 1038 | 1041 | 1040 | 1039 | 1037 | 1035 |

The graphene sensor is also tested in conductivity solutions with the conductivities of 220 uS/cm,3000 uS/cm,10500 uS/cm,40000 uS/cm,62000 uS/cm,90000 uS/cm to explore if the sensor is sensitive to solution salinity. The conductivity solutions (potassium chloride solutions) were purchased from Atlas Scientific. The results (average of multiple measurements) are shown in Table 4.5. Sample1 was soaked in the DI water for 3 hours and was renamed as Sample 1'. Measurement results with error bars are plotted in Figure 4.37. The result shows that graphene is not sensitive to solution salinity.

Table 4.5 Resistance Measurement of Sample 1 and Sample 1' in Conductivity Solutions

| Conductivity (uS/cm) | | 220 | 3,000 | 10,500 | 40,000 | 62,000 | 90,000 |
|---|---|---|---|---|---|---|---|
| Resistance(Ω) | Sample1 | 1048 | 1048 | 1048 | 1048 | 1048 | 1048 |
| | Sample1' | 959.1 | 959.3 | 959.3 | 959.1 | 959.1 | 959.2 |

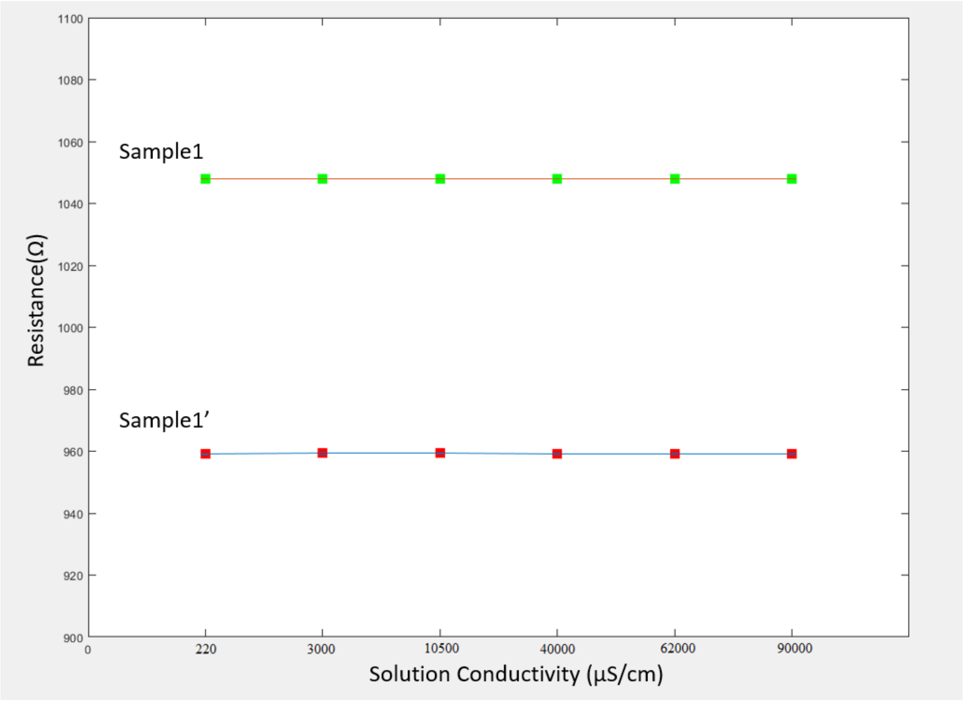

Figure 4.37 Plot for Resistance of Sample 1 and Sample 1' in Conductivity Solutions

The experiment results of the graphene pH sensors show its great potential for calibration free pH sensors. In order to further improve the performance of the sensor, first, the doping level of the graphene can be stabilized by depositing an ALD (atomic layer deposition) $Al_2O_3$ passivation layer. Second, technology for n doping of graphene shall be explored. Thirdly, circuits shall be included in the design for signal output and post signal amplifying. These will be discussed in Chapter 5.

# CHAPTER 5

# FUTURE WORK

## 5.1 Decrease the Contact Resistance of Thermoelectric Generator

The contact resistivity of the fabricated thermoelectric generator was calculated. Sample #2, Sample#5, Sample#6 described in Table 3.2 are used for the calculation. The derivation process is as following.

Based on the specification of the bismuth telluride shown in Table 3.1. ${}^{1}/_{100000}\, s/m$ is used as the electrical conductivity for both N type and P type bismuth telluride. The height of the bismuth telluride pellet is $h = 1.1 * 10^{-3}m$ and the area of the pellet is $A = 1.4 * 10^{-3} * 1.4 * 10^{-3}m^2$. Therefore, the resistance of one pellet is

$$\begin{aligned} R_{\text{pellet}} &= \rho * \frac{h}{A} = (1/100000) * (1.1 * 10^{-3}) / \,(1.4 * 10^{-3} * 1.4 * 10^{-3}) \\ &= 0.56 * 10^{-2}\text{Ohm} \end{aligned} \tag{5.1}$$

Therefore, For Sample #2, which has 25 pairs of bismuth telluride pellets, The total resistance contributed by the bismuth telluride pellets $R_{\text{tp}} = 50 * R_{\text{pellet}} = 0.28\ \text{Ohm}$

The total resistance of Sample 2, $R_{\text{total}}$, is 21.1 $\text{Ohm}$ as shown in Table 3.2. Therefore, if the metal connection resistance is ignored, the contact resistance between the metal and bismuth telluride is $(R_{\text{total}} - R_{\text{tp}})/(4 * 25) = 0.2082 Ohm$ , considering 4 contact areas for each pair.

The contact resistivity $\rho_c = R_{contact} * A = \ 0.2082 * 1.4 * 10^{-3} * 1.4 * 10^{-3} = 4 * 10^{-3}\ \text{ohm} * cm^2$

Similarly, for Sample #5, which has 35 pairs of Bismuth Telluride pellets, the calculated contact resistivity between the metal and the bismuth telluride is $3.6 * 10^{-3}$ ohm $* cm^2$.

For Sample #6, the calculated contact resistivity between the metal and the bismuth telluride is also $3.6 * 10^{-3}$ ohm $* cm^2$.

Compared with the previous research work (S. J. Kim et al., 2014), although Ni layer was also inserted in this work, but the contact resistivity didn't decrease ideally. The contact resistivity without Ni layer is around $10^{-1} \sim 10^{-2}$ ohm $* cm^2$.and that with Ni layer reaches $6 * 10^{-6}$ ohm $* cm^2$ in their work. This is because the dimension of the Bismuth Telluride pellets is much smaller than theirs and the Ni did not cover the whole contact area when deposited using a shadow mask.

In order to further effectively decrease the contact resistivity between the metal connection and the bismuth telluride material, soldering can be considered. However, the temperature for soldering is pretty high, where parylene C cannot stand. There other type of film that can tolerate high temperature, such as parylene N, should be used accordingly.

## 5.2 Optimized Design and Fabrication of Graphene pH Sensors

### 5.2.1 Doping of Graphene

As discussed in Chapter 4, if a positive back gate voltage or a negative back gate voltage is applied, graphene can be used to detect pH by measuring its corresponding conductance value. Applying gate voltages for graphene is called "electrical doping of graphene". Chemical doping of graphene includes substitutional doping and surface transfer doping of graphene(Liu, Liu, & Zhu, 2011). Surface transfer doping of graphene is achieved by the transfer of electrons between the dopant molecules and graphene. Graphene can be easily surface transfer p doped by water in the air or from wet chemicals. N doping of graphene proved to challenging. It has been found that wet chemical processing using ammonium fluoride solution ($NH_4F$ ) is an facile method of N doping for CVD graphene (Bong, Sul, Yoon, Choi, & Cho, 2014).

### 5.2.2 Wheastone Bridge

In order to improve the sensitivity of the device and make the output of the signal easy for post- processing and amplifying, Wheatstone Bridge is applied for the new design. The circuit diagram of Wheatstone bridge is shown in Figure 5.1. For this circuit, there are four resistors and if each of them has a change in resistance ΔR, the relation between the output voltage and input voltage is expressed Equation. (5.1). The sign of ΔR1 and ΔR3 should be different from ΔR2 and Δ R4. For instance, if ΔR1 and ΔR3 are minus then ΔR2 and Δ R4 should be plus.

$$V_{out} = \frac{(R_2 + \Delta R_2)(R_4 + \Delta R_4) - (R_1 + \Delta R_1)(R_3 + \Delta R_3)}{(R_1 + \Delta R_1 + R_2 + \Delta R_2) * (R_3 + \Delta R_3 + R_4 + \Delta R_4)} V_B \tag{5.1}$$

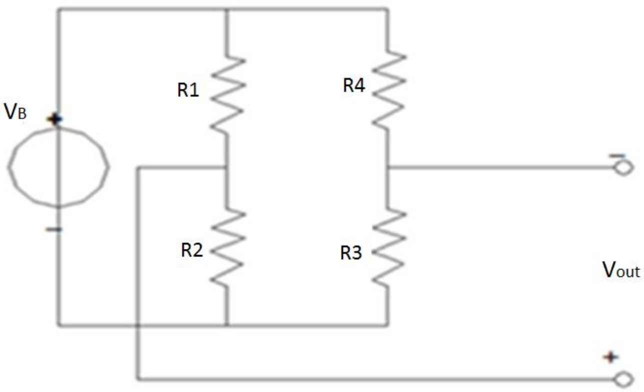

Figure 5.1 Circuit Diagram of Wheatstone Bridge

Therefore, four graphene pH resistors can construct a Wheatstone Bridge by making two of the resistors increase in resistance while the remaining two decrease in resistance when all of them are in a same acid or base solution. This can be realized by doing different types of doping for the graphene resistors (Figure 5.2). For instance, making R1 and R3 n-doping and making R2 and R4 p-doping. The most challenging technology for the new design is the n doping of graphene as we disscussed.

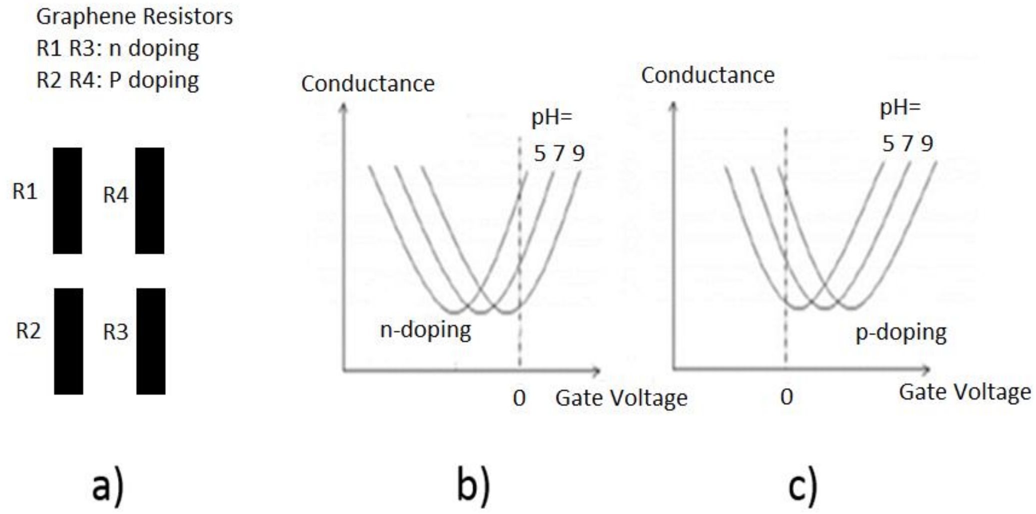

Figure 5.2 Wheatstone Bridge Constructed by Graphene Resistors

### 5.2.3 Fabrication of the Optimized pH Sensors with Wheatstone Bridge Circuit Structure

Both p doped and n doped graphene resistors will be formed on the same substrate to construct the Wheatstone Bridge. The fabrication process is shown in Figure 5.3. First, the substrate is pre-cleaned and then the electrodes can be formed using lift of process. In Step 3, the graphene is etched using RIE to get individual devices. Then photoresist is deposited and patterned so that there are openings for the N doping of the graphene and other part of the graphene is covered to maintain P doped. In Step 6, the device is soaked in the $NH_4F$ solution (40%) to N dope the graphene. Then the photoresist is removed and immediately the ALD (Atomic Layer Deposition) $Al_2O_3$ layer is deposited. Final step is the wire bonding and epoxy sealing.

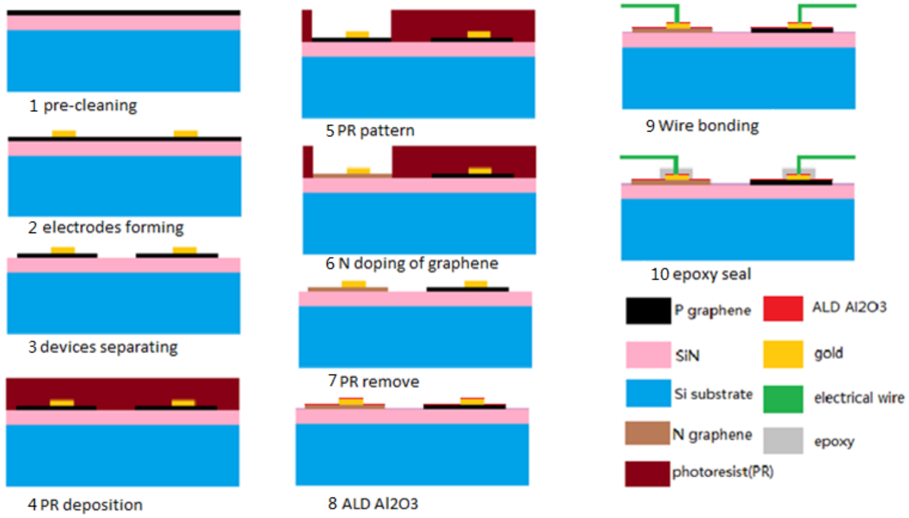

Figure 5.3 Fabrication Flow of Graphene pH Sensor with both P Doping and N Doping Graphene Resistors on the Same Substrate to Form the Wheatstone Bridge

# REFERENCES

Ang, P. K., Chen, W., Wee, A. T. S., & Loh, K. P. (2008). Solution-gated epitaxial graphene as pH sensor. *Journal of the American Chemical Society*, *130*(44), 14392–14393.

Arms, S. W., Townsend, C. P., Churchill, D. L., Galbreath, J. H., & Mundell, S. W. (2005). Power management for energy harvesting wireless sensors. In *Smart Structures and Materials* (pp. 267–275). International Society for Optics and Photonics. Retrieved from http://proceedings.spiedigitallibrary.org/proceeding.aspx?articleid=862268

Asada, H. H., Jiang, H.-H., & Gibbs, P. (2004). Active noise cancellation using MEMS accelerometers for motion-tolerant wearable bio-sensors. In *Engineering in Medicine and Biology Society, 2004. IEMBS'04. 26th Annual International Conference of the IEEE* (Vol. 1, pp. 2157–2160). IEEE. Retrieved from http://ieeexplore.ieee.org/abstract/document/1403631/

Barns, S. M., Fundyga, R. E., Jeffries, M. W., & Pace, N. R. (1994). Remarkable archaeal diversity detected in a Yellowstone National Park hot spring environment. *Proceedings of the National Academy of Sciences*, *91*(5), 1609–1613.

Bergveld, P. (2003). ISFET, theory and practice. In *IEEE Sensor Conference, Toronto* (Vol. 328).

Bhuyan, M. S. A., Uddin, M. N., Islam, M. M., Bipasha, F. A., & Hossain, S. S. (2016). Synthesis of graphene. *International Nano Letters*, *6*(2), 65–83.

Birch, M. C., Quinn, R. D., Hahm, G., Phillips, S. M., Drennan, B., Beer, R. D., … others. (2001). A miniature hybrid robot propelled by legs. In *Intelligent Robots and Systems, 2001. Proceedings. 2001 IEEE/RSJ International Conference on* (Vol. 2, pp. 845–851). IEEE. Retrieved from http://ieeexplore.ieee.org/abstract/document/976274/

Bong, J. H., Sul, O., Yoon, A., Choi, S.-Y., & Cho, B. J. (2014). Facile graphene n-doping by wet chemical treatment for electronic applications. *Nanoscale*, *6*(15), 8503–8508.

Buron, J. D., Pizzocchero, F., Jepsen, P. U., Petersen, D. H., Caridad, J. M., Jessen, B. S., … Bøggild, P. (2015). Graphene mobility mapping. *Scientific Reports*, *5*.

Busscher, H. J., & Weerkamp, A. H. (1987). Specific and non-specific interactions in bacterial adhesion to solid substrata. *FEMS Microbiology Letters*, *46*(2), 165–173.

Chen, F., Xia, J., & Tao, N. (2009). Ionic screening of charged-impurity scattering in graphene. *Nano Letters*, *9*(4), 1621–1625.

Chen, J.-H., Jang, C., Adam, S., Fuhrer, M. S., Williams, E. D., & Ishigami, M. (2008). Charged-impurity scattering in graphene. *Nature Physics*, *4*(5), 377–381.

Chen, P., Chen, T.-K., Wang, Y.-S., & Chen, C.-C. (2009). A time-domain sub-micro watt temperature sensor with digital set-point programming. *IEEE Sensors Journal*, *9*(12), 1639–1646.

Cole, D. J., Ang, P. K., & Loh, K. P. (2011). Ion adsorption at the graphene/electrolyte interface. *The Journal of Physical Chemistry Letters*, *2*(14), 1799–1803.

Cox, A., Shock, E. L., & Havig, J. R. (2011). The transition to microbial photosynthesis in hot spring ecosystems. *Chemical Geology*, *280*(3), 344–351.

Dargaville, T. R., Farrugia, B. L., Broadbent, J. A., Pace, S., Upton, Z., & Voelcker, N. H. (2013). Sensors and imaging for wound healing: a review. *Biosensors and Bioelectronics*, *41*, 30–42.

Deposition Processes. (n.d.). Retrieved December 30, 2016, from https://www.mems-exchange.org/MEMS/processes/deposition.html

Eftekhari, A., Kazemzad, M., & Keyanpour-Rad, M. (2006). Significant effect of dopant size on nanoscale fractal structure of polypyrrole film. *Polymer Journal*, *38*(8), 781–785.

Fahrner, W. R., & Schwertheim, S. (2009). *Semiconductor thermoelectric generators*. Trans Tech Publ.

Frosio, I., Pedersini, F., & Borghese, N. A. (2009). Autocalibration of MEMS accelerometers. *IEEE Transactions on Instrumentation and Measurement*, *58*(6), 2034–2041.

Gaucher, E. A., Kratzer, J. T., & Randall, R. N. (2010). Deep phylogeny—how a tree can help characterize early life on Earth. *Cold Spring Harbor Perspectives in Biology*, *2*(1), a002238.

Geim, A. K., & Novoselov, K. S. (2007). The rise of graphene. *Nature Materials*, *6*(3), 183–191.

Gottenbos, B., Busscher, H. J., Van Der Mei, H. C., & Nieuwenhuis, P. (2002). Pathogenesis and prevention of biomaterial centered infections. *Journal of Materials Science: Materials in Medicine*, *13*(8), 717–722.

Graphene on SiO2 Substrate. (n.d.). Retrieved February 17, 2017, from http://www.acsmaterial.com/graphene-on-sio2-substrate-1548.html

Guo, B., Liu, Q., Chen, E., Zhu, H., Fang, L., & Gong, J. R. (2010). Controllable N-doping of graphene. *Nano Letters*, *10*(12), 4975–4980.

Haldane, F. D. M. (1988). Model for a quantum Hall effect without Landau levels: Condensed-matter realization of the" parity anomaly". *Physical Review Letters, 61*(18), 2015.

Han, R., Zhang, Z., Ren, T., & Lin, H. (2011). Research for piezoresistive pressure sensors: Methods to reduce the influence of processing deviation on sensitivity and improve product consistency. In *Sensors, 2011 IEEE* (pp. 573–576). IEEE. Retrieved from http://ieeexplore.ieee.org/xpls/abs_all.jsp?arnumber=6127413

Han, R., Zhang, Z., Ren, T., Lin, H., & Liu, L.-T. (2012). Simulation Method for the Sensitivity and Linearity of Piezoresistive Pressure Sensors. *Weina Dianzi Jishu(Micronanoelectronic Technology), 49*(2).

Han, R., Zhang, Z., Ren, T., Lin, H., & Pang, B. (2011). Methods of superior design for the full scale output of piezoresistive pressure sensors. In *Electrical Power Systems and Computers* (pp. 55–61). Springer. Retrieved from http://link.springer.com/chapter/10.1007/978-3-642-21747-0_8

Hanein, Y., BÎhringer, K. F., Wyeth, R. C., & Willows, A. O. D. (2002). 1.3 Towards MEMS Probes for Intracellular Recording. Retrieved from http://people.stfx.ca/rwyeth/reprints/HANEIN2002.pdf

Hanson, G. W. (2008). Dyadic Green’s functions and guided surface waves for a surface conductivity model of graphene. *Journal of Applied Physics, 103*(6), 064302. https://doi.org/10.1063/1.2891452

Hanson, S., Foo, Z., Blaauw, D., & Sylvester, D. (2010). A 0.5 V sub-microwatt CMOS image sensor with pulse-width modulation read-out. *IEEE Journal of Solid-State Circuits, 45*(4), 759–767.

Huang, X., & Chuan, T. K. (2002). MEMS-micropumps: a review. In *Journal of Fluids Engineering-Transactions of the ASME*. Retrieved from http://offshoremechanics.asmedigitalcollection.asme.org/pdfaccess.ashx?url=/data/journals/jfega4/27173/384_1.pdf

Hugenholtz, P., Pitulle, C., Hershberger, K. L., & Pace, N. R. (1998). Novel division level bacterial diversity in a Yellowstone hot spring. *Journal of Bacteriology, 180*(2), 366–376.

Iyore, O. D., Lee, T. H., Gupta, R. P., White, J. B., Alshareef, H. N., Kim, M. J., & Gnade, B. E. (2009). Interface characterization of nickel contacts to bulk bismuth tellurium selenide. *Surface and Interface Analysis, 41*(5), 440–444.

Jablan, M., Buljan, H., & Soljačić, M. (2009). Plasmonics in graphene at infrared frequencies. *Physical Review B, 80*(24), 245435.

Jones, C. D. W., Bolle, C. A., Ryf, R., Simon, M. E., Pardo, F., Aksyuk, V. A., … others. (2009). MEMS thermal imager with optical readout. *Sensors and Actuators A: Physical*, *155*(1), 47–57.

Jun, L., Lian-meng, Z., Li, H., & Xin-feng, T. (2003). Synthesis and thermoelectric properties of polyaniline. *Journal of Wuhan University of Technology–Materials Science Edition*, *18*(3), 53–55.

Kaiper, G. V. (2004). *US Energy Flow Trends-2002*. United States. Department of Energy. Retrieved from https://e-reports-ext.llnl.gov/pdf/308904.pdf

Katsnelson, M. I. (2006). Zitterbewegung, chirality, and minimal conductivity in graphene. *The European Physical Journal B-Condensed Matter and Complex Systems*, *51*(2), 157–160.

Kemp, N. T., Kaiser, A. B., Liu, C.-J., Chapman, B., Mercier, O., Carr, A. M., … Lee, J. Y. (1999). Thermoelectric power and conductivity of different types of polypyrrole. *Journal of Polymer Science Part B: Polymer Physics*, *37*(9), 953–960.

Kim, D.-H., Ahn, J.-H., Choi, W. M., Kim, H.-S., Kim, T.-H., Song, J., … Rogers, J. A. (2008). Stretchable and foldable silicon integrated circuits. *Science*, *320*(5875), 507–511.

Kim, S. J., We, J. H., & Cho, B. J. (2014). A wearable thermoelectric generator fabricated on a glass fabric. *Energy & Environmental Science*, *7*(6), 1959–1965.

Knauth, L. P., & Lowe, D. R. (2003). High Archean climatic temperature inferred from oxygen isotope geochemistry of cherts in the 3.5 Ga Swaziland Supergroup, South Africa. *Geological Society of America Bulletin*, *115*(5), 566–580.

Konhauser, K. O., Jones, B., Reysenbach, A.-L., & Renaut, R. W. (2003). Hot spring sinters: keys to understanding Earth's earliest life forms. *Canadian Journal of Earth Sciences*, *40*(11), 1713–1724.

Kuai, X., & Zhao, Q. (2017). Examining healthy food accessibility and disparity in Baton Rouge, Louisiana. *Annals of GIS*, *23*(2), 103–116. https://doi.org/10.1080/19475683.2017.1304448

Lee, K. B. (2011). *Principles of microelectromechanical systems*. John Wiley & Sons. Retrieved from https://books.google.com/books?hl=en&lr=&id=-fyb36q4q-QC&oi=fnd&pg=PT9&dq=Principles+of+Microelectromechanical+Systems&ots=xDsCZ-95dp&sig=L46buGMbxqbMHzVjJT2gJ0MaIrA

Lee, K., Cho, S., Park, S. H., Heeger, A. J., Lee, C.-W., & Lee, S.-H. (2006). Metallic transport in polyaniline. *Nature*, *441*(7089), 65–68.

Lei, N., Li, P., Xue, W., & Xu, J. (2011). Simple graphene chemiresistors as pH sensors: fabrication and characterization. *Measurement Science and Technology*, *22*(10), 107002.

Leonov, V., Fiorini, P., Sedky, S., Torfs, T., & Van Hoof, C. (2005). Thermoelectric MEMS generators as a power supply for a body area network. In *Solid-State Sensors, Actuators and Microsystems, 2005. Digest of Technical Papers. TRANSDUCERS'05. The 13th International Conference on* (Vol. 1, pp. 291–294). IEEE. Retrieved from http://ieeexplore.ieee.org/abstract/document/1496414/

Liang, M., Huang, H., Agafonov, V., Tang, R., Han, R., & Yu, H. (2016). Molecular electronic transducer based planetary seismometer with new fabrication process (pp. 986–989). Presented at the IEEE 29th International Conference on Micro Electro Mechanical Systems (MEMS), Shanghai: IEEE.

Liu, H., Liu, Y., & Zhu, D. (2011). Chemical doping of graphene. *Journal of Materials Chemistry*, *21*(10), 3335–3345.

Luczak, S., Oleksiuk, W., & Bodnicki, M. (2006). Sensing tilt with MEMS accelerometers. *IEEE Sensors Journal*, *6*(6), 1669–1675.

Martel, S., Sherwood, M., Helm, C., De Quevedo, W. G., Fofonoff, T., Dyer, R., … Hunter, I. (2001). Three-legged wireless miniature robots for mass-scale operations at the sub-atomic scale. In *Robotics and Automation, 2001. Proceedings 2001 ICRA. IEEE International Conference on* (Vol. 4, pp. 3423–3428). IEEE. Retrieved from http://ieeexplore.ieee.org/abstract/document/933147/

Mattevi, C., Kim, H., & Chhowalla, M. (2011). A review of chemical vapour deposition of graphene on copper. *Journal of Materials Chemistry*, *21*(10), 3324–3334.

McClure, J. W. (1956). Diamagnetism of graphite. *Physical Review*, *104*(3), 666.

Miyajima, H., Murakami, K., & Katashiro, M. (2004). MEMS optical scanners for microscopes. *IEEE Journal of Selected Topics in Quantum Electronics*, *10*(3), 514–527.

Nathanson, H. C., & Wickstrom, R. A. (1965). A RESONANT-GATE SILICON SURFACE TRANSISTOR WITH HIGH-Q BAND-PASS PROPERTIES. *Applied Physics Letters*, *7*(4), 84–86.

Novoselov, K. S., Morozov, S. V., Mohinddin, T. M. G., Ponomarenko, L. A., Elias, D. C., Yang, R., … Jiang, D. (2007). Electronic properties of graphene. *Physica Status Solidi (B)*, *244*(11), 4106–4111.

Oiler, J. (2013). *MEMS Harsh Environment Sensors for Earth and Space Exploration*. Arizona State University. Retrieved from http://gradworks.umi.com/35/58/3558003.html

Otto, T., Saupe, R., Weiss, A., Stock, V., Throl, O., Grählert, W., … Gessner, T. (2009). MEMS analyzer for fast determination of mixed gases. In *SPIE MOEMS-MEMS: Micro-and Nanofabrication* (p. 72080E–72080E). International Society for Optics and Photonics. Retrieved from http://proceedings.spiedigitallibrary.org/proceeding.aspx?articleid=809104

Park, K.-T., Shin, S.-M., Tazebay, A. S., Um, H.-D., Jung, J.-Y., Jee, S.-W., … others. (2013). Lossless hybridization between photovoltaic and thermoelectric devices. *Scientific Reports*, *3*. Retrieved from http://www.nature.com/srep/2013/130703/srep02123/full/srep02123.html?WT.ec_id=SREP-639-20130801

Parra, C., Ramírez, C., Jimenez, E., Dorta, F., Villalobos, P., Henríquez, R., & Rojas, R. (2015). A nanomolecular approach to decrease adhesion of biofouling-producing bacteria to graphene-coated material. *Journal of Nanobiotechnology*, *13*(1), 82.

Parylene Coating & Vapor Deposition Process | VSI Parylene. (n.d.). Retrieved December 7, 2017, from https://vsiparylene.com/parylene-advantages/process/

Rone, W. S., & Ben-Tzvi, P. (2011). MEMS-based microdroplet generation with integrated sensing. In *Excerpt from the Proceedings of the 2011 COMSOL Conference in Boston, Exhibit* (Vol. 2018). Retrieved from https://www.comsol.ru/paper/download/100745/bentzvi_paper.pdf

Runyan, W. R., & Bean, K. E. (1990). *Semiconductor integrated circuit processing technology*. Addison Wesley Publishing Company.

Schedin, F., Geim, A. K., Morozov, S. V., Hill, E. W., Blake, P., Katsnelson, M. I., & Novoselov, K. S. (2007). Detection of individual gas molecules adsorbed on graphene. *Nature Materials*, *6*(9), 652–655.

Shock, E. L., Holland, M., Meyer-Dombard, D. R., & Amend, J. P. (2005). Geochemical sources of energy for microbial metabolism in hydrothermal ecosystems: Obsidian Pool, Yellowstone National Park. *Geothermal Biology and Geochemistry in Yellowstone National Park*, *1*, 95–112.

Singh, S. P., Li, Y., Be'er, A., Oren, Y., Tour, J. M., & Arnusch, C. J. (2017). Laser-Induced Graphene Layers and Electrodes Prevents Microbial Fouling and Exerts Antimicrobial Action. *ACS Applied Materials & Interfaces*.

Singh-Gasson, S., Green, R. D., Yue, Y., Nelson, C., Blattner, F., Sussman, M. R., & Cerrina, F. (1999). Maskless fabrication of light-directed oligonucleotide microarrays using a digital micromirror array. *Nature Biotechnology*, *17*(10), 974–978.

Slonczewski, J. C., & Weiss, P. R. (1958). Band structure of graphite. *Physical Review*, *109*(2), 272.

Snyder, G. J. (2008). Small thermoelectric generators. *The Electrochemical Society Interface*, *17*(3), 54.

Stauber, T., Peres, N. M. R., & Geim, A. K. (2008). Optical conductivity of graphene in the visible region of the spectrum. *Physical Review B*, *78*(8), 085432.

Suemori, K., Hoshino, S., & Kamata, T. (2013). Flexible and lightweight thermoelectric generators composed of carbon nanotube–polystyrene composites printed on film substrate. *Applied Physics Letters*, *103*(15), 153902.

Suntharalingam, V., Berger, R., Burns, J. A., Chen, C. K., Keast, C. L., Knecht, J. M., … others. (2005). Megapixel CMOS image sensor fabricated in three-dimensional integrated circuit technology. In *Solid-State Circuits Conference, 2005. Digest of Technical Papers. ISSCC. 2005 IEEE International* (pp. 356–357). IEEE. Retrieved from http://ieeexplore.ieee.org/abstract/document/1494016/

There's more to come from Moore. (2015). *Nature News*, *520*(7548), 408. https://doi.org/10.1038/520408a

Thermoelectric Energy Harvesting | DigiKey. (n.d.). Retrieved January 2, 2017, from http://www.digikey.com/en/articles/techzone/2011/oct/thermoelectric-energy-harvesting

Tritt, T. M., & Subramanian, M. A. (2006). Thermoelectric materials, phenomena, and applications: a bird's eye view. *MRS Bulletin*, *31*(03), 188–198.

Warner, J. H., Schaffel, F., Rummeli, M., & Bachmatiuk, A. (2012). *Graphene: Fundamentals and emergent applications*. Newnes. Retrieved from https://books.google.com/books?hl=en&lr=&id=RqOUsIWTZAIC&oi=fnd&pg=PP1&dq=Fundamentals+and+emergent+applications&ots=WYvxFRu0Tb&sig=cRzbwa9obCi3CFYfypYRa95-k7k

Wentz, E. A., & Zhao, Q. (2015). Assessing validation methods for building identification and extraction. In *Urban Remote Sensing Event (JURSE), 2015 Joint* (pp. 1–4). IEEE. Retrieved from http://ieeexplore.ieee.org/xpls/abs_all.jsp?arnumber=7120453

Werner-Allen, G., Lorincz, K., Ruiz, M., Marcillo, O., Johnson, J., Lees, J., & Welsh, M. (2006). Deploying a wireless sensor network on an active volcano. *IEEE Internet Computing*, *10*(2), 18–25.

Wu, J., Fedder, G. K., & Carley, L. R. (2002). A low-noise low-offset chopper-stabilized capacitive-readout amplifier for CMOS MEMS accelerometers. In *Solid-State Circuits Conference, 2002. Digest of Technical Papers. ISSCC. 2002 IEEE International* (Vol. 1, pp. 428–478). IEEE. Retrieved from http://ieeexplore.ieee.org/abstract/document/993115/

Yabiku, S., Glick, J., Wentz, E., Ghimire, D., & Zhao, Q. (2017). Comparing Paper and Tablet Modes of Retrospective Activity Space Data Collection. *Survey Research Methods*, *11*(3), 329–344. https://doi.org/10.18148/srm/2017.v11i3.6741

Yang, P., & Liao, N. (2007). Surface sliding simulation in micro-gear train for adhesion problem and tribology design by using molecular dynamics model. *Computational Materials Science*, *38*(4), 678–684.

Zhang, J., Zhang, Z. H., Chen, T., Kong, X. M., Ren, T. L., & Liu, L. T. (2011). A Tire Pressure Monitoring System Based on MEMS Sensor. In *Key Engineering Materials* (Vol. 483, pp. 370–373). Trans Tech Publ. Retrieved from http://www.scientific.net/KEM.483.370

Zhang, Z., Ren, T., Han, R., Yuan, L., & Pang, B. (2013). SIMULATION METHODS OF PIEZORESISTIVE PRESSURE SENSORS IN ORDER TO IMPROVE CONSISTENCY. *Modern Physics Letters B*, *27*(02), 1350011. https://doi.org/10.1142/S0217984913500115

Zhang, Z.-H., Ren, T.-L., Zhang, Y.-H., Han, R., & Liu, L.-T. (2012). Low Power and High Sensitivity MOSFET-Based Pressure Sensor. *Chinese Physics Letters*, *29*(8), 088501. https://doi.org/10.1088/0256-307X/29/8/088501

Zhao, Q. (2017). *Evaluating the Effectiveness of Tree Locations and Arrangements for Improving Urban Thermal Environment* (PhD Thesis). ARIZONA STATE UNIVERSITY. Retrieved from https://repository.asu.edu/attachments/192532/content/Zhao_asu_0010E_17356.pdf

Zhao, Q., Myint, S. W., Wentz, E. A., & Fan, C. (2015). Rooftop Surface Temperature Analysis in an Urban Residential Environment. *Remote Sensing*, *7*(9), 12135–12159. https://doi.org/10.3390/rs70912135

Zhao, Q., & Wentz, E. A. (2016). A MODIS/ASTER Airborne Simulator (MASTER) Imagery for Urban Heat Island Research. *Data*, *1*(1). https://doi.org/10.3390/data1010007

Zhao, Q., Wentz, E. A., Fotheringham, S., Yabiku, S. T., Hall, S. J., Glick, J. E., … Heavenrich, H. (2016). Semi-parametric Geographically Weighted Regression (S-GWR): a Case Study on Invasive Plant Species Distribution in Subtropical Nepal. In *Short peer-reviewed papers proceedings of the GIScience 2016*. Montreal, Canada.

Zhao, Q., Wentz, E. A., & Murray, A. T. (2014). Shade Optimization in a Desert Environment. In *Extended Abstract Proceedings of the GIScience 2014* (pp. 118–121). Retrieved from https://www.researchgate.net/profile/Qunshan_Zhao/publication/271215424_Sha de_Optimization_in_a_Desert_Environment/links/54c2c98c0cf256ed5a8f950c.pdf

Zhao, Q., Wentz, E. A., & Murray, A. T. (2017). Tree shade coverage optimization in an urban residential environment. *Building and Environment*, *115*, 269–280. https://doi.org/10.1016/j.buildenv.2017.01.036

Zhao, Q., Yang, J., Wang, Z.-H., & Wentz, E. (2018). Assessing the Cooling Benefits of Tree Shade by an Outdoor Urban Physical Scale Model at Tempe, AZ. *Urban Science*, *2*(1), 4. https://doi.org/10.3390/urbansci2010004

Zhao, W., Tan, P., Zhang, J., & Liu, J. (2010). Charge transfer and optical phonon mixing in few-layer graphene chemically doped with sulfuric acid. *Physical Review B*, *82*(24), 245423.